6-6-2016

Advancements in Fiber, Interface, and Matrix Materials for Ceramic Matrix Composites

Rebecca E. Gottlieb
rebecca.gottlieb@uconn.edu

Advancements in Fiber, Interface, and Matrix Materials for Ceramic Matrix Composites
Rebecca Eve Gottlieb, PhD
University of Connecticut, 2016

Abstract

Chemical Vapor Deposition (CVD) was used to deposit a variety of carbide, boride, and nitride interfacial coatings on substrates including silicon carbide based ceramic fibers for use in fabrication of components in Ceramic Matrix Composites (CMCs). Experiments were designed to correlate coating thickness and time required for these coating depositions and the materials fabricated in these experiments were used in various other experimental designs in this work. Coatings were characterized for their thickness and morphology, as well as to identify the phases present in the materials.

A polycarbosilane pre-ceramic polymer was developed using a modified in-situ Grignard reaction with chlorinated silane precursors. This polymer was designed for use as both a precursor to silicon carbide ceramic fibers and for the ceramic matrix material in CMCs fabricated using Polymer Impregnation Pyrolysis (PIP). The polymer was characterized using Fourier Transform Infrared (FT-IR) spectroscopy and ^{1}H Nuclear Magnetic Resonance (NMR) to identify functional groups and to propose polymer structure, and Thermogravimetric Analysis coupled with Mass Spectrometry (TG-MS)was used to propose a mechanism for ceramic formation. The pyrolyzed ceramic was characterized using X-Ray Diffraction (XRD) to determine crystalline phases present, Scanning Electron Microscopy (SEM) and Energy Dispersive X-Ray Spectroscopy (EDS) to examine grain morphology and elemental distribution.

A second pre-ceramic polymer was designed to incorporate titanium and boron into a commercially available polymer (Starfire® SMP-10) for the intention of improving select properties for use in CMCs as both a fiber precursor and as a matrix material. The polymer was designed to form silicon carbide and titanium diboride upon pyrolysis in a two-step

process. Titanium was first incorporated into the polymer, followed by a heat-treatment in boron trichloride to boronize the titanium. Both the as-received polymer and the modified polymer were characterized using TG-MS to determine the ceramic yield and mechanism of ceramic formation. Heat treatment studies were performed using XRD to determine the optimum temperature range for boron incorporation during the heat treatment. The ceramic was characterized using SEM and EDS to examine the grain growth inhibition provided by the titanium diboride, as well as to determine elemental distribution in the ceramics. CMCs were fabricated from both the commercially available polymer and the modified polymer and the composites were analyzed for the ultimate Flexural Stress measured before mechanical failure occurred.

Cobalt metal was deposited on a variety of substrates including ceramic fiber and then coated with CVD silicon dioxide and Chemical Vapor Infiltration (CVI) silicon carbide protective coatings for use in a magnetic ceramic matrix composite. The protective coatings were designed to help increase oxidation resistance so the composite would retain magnetic properties at elevated temperatures under oxidizing conditions. The material was characterized using XRD to determine crystalline phases present, and SEM and EDS were used to examine the coating morphology, adhesion, and elemental distribution in the composite. Superconducting Quantum Interference Device (SQUID) was used to determine the magnetic properties of the material during coating application and oxidation resistance studies. Tensile testing was used to to determine the ultimate tensile strength and the effect on coating application and oxidation on the strength of the composite both with and without the oxidation resistive coatings.

Advancements in Fiber, Interface, and Matrix Materials for Ceramic Matrix Composites

Rebecca Eve Gottlieb, PhD
B.S., University of Hartford, 2011

A Dissertation
Submitted in Partial Fulfillment of the
Requirement for the Degree of
Doctor of Philosophy at the
University of Connecticut

2016

2016

Approval Page

Doctor of Philosophy Dissertation
Advancements in Fiber, Interface, and Matrix Materials for Ceramic Matrix Composites

Presented by
Rebecca Eve Gottlieb

Major Advisor 
Steven L. Suib

Associate Advisor 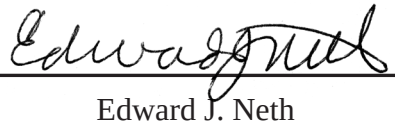
Edward J. Neth

Associate Advisor 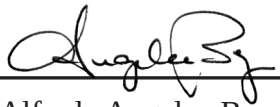
Alfredo Angeles-Boza

Associate Advisor 
Douglas H. Adamson

Associate Advisor 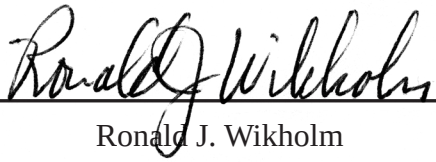
Ronald J. Wikholm

University of Connecticut

2016

Dedicated to my husband, Rich.

Acknowledgements

I would like to thank my major advisor, Dr. Steven Suib, for his direction and support over the last five years. His guidance has helped me grow as a student and as a researcher, and for this I am eternally grateful. I also would like to extend my gratitude to Dr. Michael A. Kmetz, whose unique approaches to research and life will stand with me as lifelong lessons. I would also like thank Dr. Francis Galasso for his knowledge, support, and assistance in completing my degree and in finding a job, and my committee members, Dr. Edward J. Neth, Dr. Alfredo Angeles-Boza, Dr. Douglas H. Adamson, and Dr. Ronald J. Wikholm for their support.

I would like extend a special acknowledgment to Shannon Poges, my coworker, lab-mate, and partner in crime for the encouragement and clarity in our research over the last three years. I would also like to thank my fellow graduate students, both past and present, Chris Monteleone, Ken Petroski, Dr. Gavin Richards, Dr. Timothy Coons, Dr. Justin Reutenauer, and Sam Frueh. I would also like to extend gratitude to Dan Daleb at the UConn machine shop, for being a teacher, mentor, and friend throughout my time here.

Finally I would like to thank my family, especially my husband Rich, for continued support and perspective throughout my career as a chemist, my parents, Jackie and Mark, as I would not have been able to accomplish this without them, and my grandmother and great uncle, Marilyn and Herb, for their encouragement and support over the years.

Table of Contents

List of Figures

Chapter Page

List of Tables

Chapter Page

Chapter 1 Introduction

1.1 High Temperature Materials

The demand for materials capable of withstanding high temperatures has developed significantly within the last century with the advancement of powerful vehicles and engine components[1]. Ceramic matrix composites (CMCs) are multi-component systems capable of withstanding these high temperatures, combining both the excellent strength and thermal capabilities of ceramics with the durability of advanced composite systems. These CMCs use a three-part system of ceramics to provide the hardness, heat resistance, oxidation resistance, and chemical resistance, low density, low thermal expansion coefficients, and refractory properties of ceramics while combating the inherent brittle nature of these materials through a multi-component composite system[2].

High-temperature materials are necessary for the manufacture and operation of components in power generation, aerospace, and military technologies. Materials capable of withstanding the elevated temperatures present in these components are essential for advancement in these fields and the engine systems require even more durable and heat-resistant materials as power and efficiency of these machines continue to advance. Development of new high-temperature materials and systems is imperative to keep up with the advancements in this power generating industry[3].

Historically, high-temperature materials have been used in advanced engineering applications since the initial invention of the steam turbine in the 1880's. The production of petroleum based chemicals lead to the development of materials like alloyed steels, tungsten filament lamps, and nickel-chromium alloys, advancing the fields of metallurgy, coatings, and composites. Within the last 50 years, materials capable of withstanding 1000°C operational

temperatures have been discovered, developed, and tested. These materials, including carbon fibers, titanium alloys, thermal barrier coatings, alumina, nickel super-alloys, and ceramic matrix composites have provided significant advancement in high temperature materials[4].

Since the 1900's, use of nickel alloys in high temperature applications like aircraft panels and aerospace engines has been conventional. These alloys, initially designed to include nickel, chromium, and other metal additives, were developed with the intention of providing both oxidation and corrosion resistance. Mechanical testing of these alloys showed the materials to also have excellent strength, providing a combination of properties for use in engine turbines[5]. Further development of these alloys lead to the incorporation of nickel, chromium, iron, silicon and aluminum in varying concentrations, producing alloys like like the Brightray™ series and Inconel™ metals. These alloys were the industry standard for exhaust manifolds in aircraft engines. Nickel super-alloys like Nimonic® expanded temperature and strength capabilities through the addition of elements like boron, carbon, zirconium and hafnium for grain boundary inhibition and strengthening. Aluminum, tantalum, and titanium were added for precipitation strengthening, molybdenum, tantalum, tungsten and rhenium for solid solution strengthening, and aluminum and chromium for surface oxidation and corrosion protection[6]. Research and development of high-temperature materials continued through the 1990's, providing materials like CMSX-4® which was capable of withstanding temperatures as high as 1050°C in engine turbine blades[7]. These alloys provided excellent strength and durability in these applications and are still the industry standard in a variety of applications, however these materials are still limited by their operational temperature.

Titanium alloys also exhibited excellent high temperature properties while maintaining strength at above 1100°C. Titanium and aluminum metal matrix composites (MMCs) were initially fabricated using titanium aluminides, providing excellent heat resistance and high melting points at 1460°C[8]. These composites used reinforcing materials composed of silicon carbide, boron, or aluminum metal, provided strength, toughening, and structure in these MMCs. These composites were fabricated using chemical vapor deposition of silicon carbide

onto tungsten or carbon core wires to produce the reinforcement, followed by application of the metal matrix through hot-pressing methods. These strong composites proved to be durable, but were limited by the strong interfacial bond of fiber to matrix and the mismatch of thermal expansion coefficients. Damage including cracking, chipping, and structural failures where the fiber met the matrix and occurred at elevated temperatures, as well as during the heat up and cool-down processes resulting in poor composite performance in heat cycling tests[9]. These metal composites also had a higher density than ceramic matrix composites, another downfall in the system and a deterrent against using these MMCs in typical aerospace and aircraft applications where weight was a major concern.

Ceramic matrix composites were designed with the shortcomings of other high-temperature materials in mind. Ceramics provided higher melting points than in metal alloys or MMCs, allowing for even higher operating conditions, while low and well-matched thermal expansion coefficients performed well in temperature cycling tests for engine applications[10]. Ceramic matrix composites provided solutions for the failures of other high-temperature systems, and continued development has lead to the incorporation of these systems into modern aircraft. The potential for future use in both commercial and military aircraft, as well as aerospace and power generation applications remains high as research and development is continued with these systems.

1.2 Ceramic Matrix Composites (CMCs)

Ceramic Matrix Composites consist of three separate parts, designed to function as a complete system with excellent durability and strength provided by these components. These systems are typically made from either oxide ceramics or non-oxide ceramics exclusively. Both oxide and non-oxide CMCs are designed specifically for use in high temperature applications, capable of withstanding both significant heat and extreme oxidizing conditions. Oxide CMCs are typically used under lower operating conditions, fabricated either with or without an interphase

material, and more with a more porous design. Non-oxide CMCs, often composed of silicon carbide, are designed to operate at extremely high temperatures, typically above 1400°C. These systems are fabricated with ceramic materials with naturally high melting points and inherent oxidation resistance[11]. These composites are assembled with a non-oxide ceramic interphase as one of the components which functions as a solid state lubricant, providing strength and durability to the CMC. Recent developments, as discussed in this thesis, include the novel incorporation of refractory ceramics like borides, as well as additional dopants used in multiple parts of the system to tailor the properties of the resulting composites. These new materials are designed, fabricated, and tested, providing significant advancement in the path to develop an incredibly high-temperature, durable composite system.

Figure 1-1 shows a cross-sectional micrograph of a CMC comprised of silicon carbide fibers and a silicon carbide matrix, abbreviated as a SiC/ SiC composite. The interface in the CMC shown has an interphase composed of boron nitride and silicon nitride with a (BN / Si_3N_4). The individual parts of a CMC are detailed in the following sections.

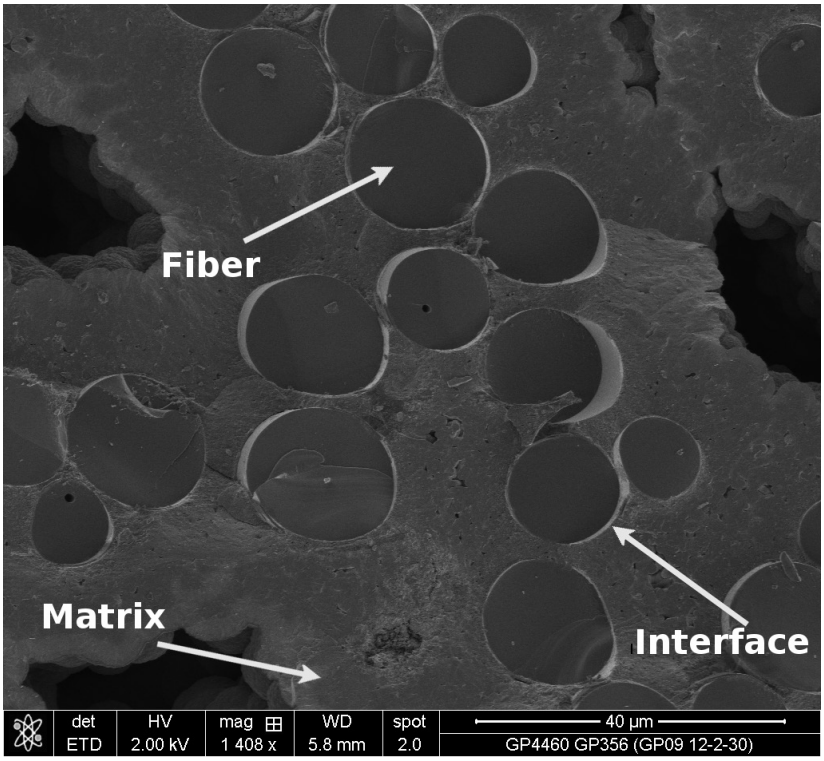

Figure 1-1. Cross Sectional Micrograph of Ceramic Matrix Composite

In a Continuous Fiber Reinforced Ceramic Matrix Composite (CFR- CMC), fibers provide reinforcement, strength and structure in the composite system. These fibers can be present in a CMC as uni-directional fiber tow, as well as both two-dimensional and three-dimensional woven fabrics. Other types of CMCs can use short, chopped, multi-directional fiber whiskers, as well as other types of ceramic reinforcement or filler to provide structure. When fibers are used, the individual filaments are designed to have very small diameters, typically in the range of 10 to 20 micron, resulting in a ceramic fiber with reduced brittleness and increased flexibility[12]. The Young's moduli of these fibers are relatively low when the fibers are designed with these small diameters, providing more flexibility than a bulk ceramic of the same material[13].

The fiber reinforcement in a CFR-CMC provides excellent strength and durability for high temperature applications and are produced from both oxide and non-oxide ceramics. Oxide fibers include ceramics like alumina, silicon dioxide, borea, and zirconia in varying

combinations[14], while non-oxides are typically composed of silicon carbide, silicon nitride, and carbon, as well as additives like boron, titanium, and zirconium. These ceramics all have low densities and relatively high melting points, making them excellent materials for use in high-temperature applications. Fibers are typically manufactured using methods unique to fiber production including spinning and CVD on resistively heated metal cores. Hot-pressing and sintering processing methods used for bulk ceramics do not allow for the production of the fine diameters required for these advanced fibers, and fabrication is generally limited to spinning the fiber from a liquid, organic precursor or through chemical vapor deposition of these ceramics on an existing fiber substrate. Spun fibers, like those produced from pre-ceramic polymers including polycarbosilane, are cured through irradiation or through sintering, producing small diameter, uniform continuous fiber filaments. These filaments are combined to produce uni-directional fiber tow, which can be used in CMCs or can be woven into complex shapes and patterns for fabrics in composite systems[15]. The ceramics used in these fibers are typically designed to be amorphous to micro-crystalline which allows for more flexibility and less rigidity in the reinforcement system overall[16]. Advanced ceramic materials, as well as the use of grain growth inhibitors and the newly developed pre-ceramic polymers detailed in this thesis, continue the important research on these fiber systems, increasing the strength and durability in future materials.

The interface material (also called the interphase) in a ceramic matrix composite is applied directly to the fibers and provides the composite with strength mechanisms exhibited in CMCs. Application of a weakly bound interface provides the system with a means of energy dispersion for the mechanical stresses experienced during operation[17]. Bulk ceramics have a very low fracture toughness and experience significant cracking readily due to their inherent brittleness[18]. Monolithic and bulk ceramics are susceptible to catastrophic failure resulting from even a small crack in the material, while a CMC with an interface allows for easy slipping between the fiber and the matrix. The weakly bound interface provides a means for energy dispersion throughout the ceramic material, resulting in strengthening mechanisms like crack

deflection, fiber-to-matrix debonding, fiber bridging, and fiber pullout, whereas a crack in a bulk ceramic propagates through the entire monolith, resulting in mechanical failure of the material[19]. In the CMC with an interface, the crack travels a more complicated path, as observed in *Figure 1-2*, allowing for energy dispersion and absorption in the composite system. These mechanisms are what contribute to the strength and durability of three-part ceramic matrix composite system[20].

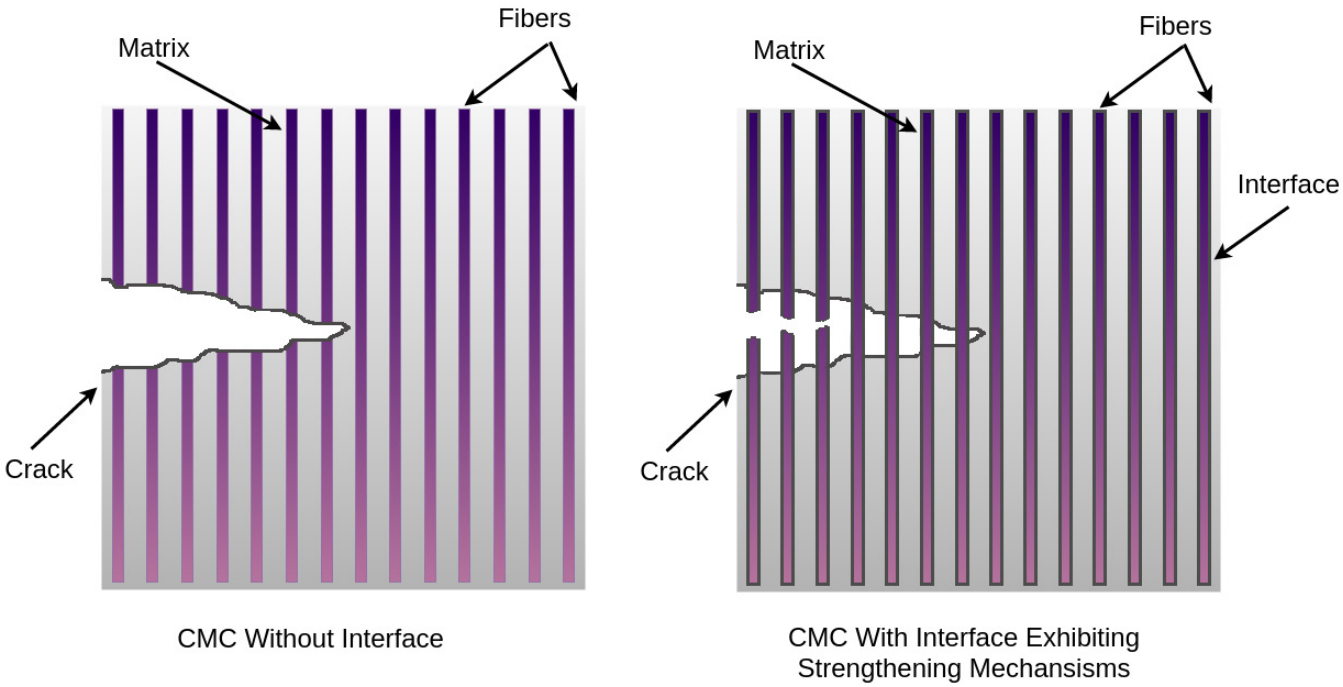

Figure 1-2. Strengthening Mechanisms in a Continuous Fiber Reinforced Ceramic Matrix Composite

Interfaces in CMCs are typically composed of materials that have fine layered structures like hexagonal boron nitride and graphitic carbon. These two compounds have hexagonal layered structures containing strong covalent bonds between the in-plane atoms and weak van der Waals forced holding together the layers[21]. The structure is quite conducive of slippage between the weakly-interactive layers, providing a solid state lubricant in the interface material. Boron nitride has relatively good thermal stability, decomposing at 1000°C in air and 2800°C

under inert atmosphere, however it is very susceptible to moisture damage. To overcome this issue, a protective layer of non-oxide ceramic, either silicon carbide or silicon nitride, is applied over the boron nitride interface during the fabrication process to prevent moisture damage in the coating[22]. Carbon interfaces have much lower thermal stability, decomposing in air near 500°C[23], however these can also be coated with a non-oxide ceramic as a means of oxidation protection. Non-oxide interfaces are currently in development and candidate materials include calcium oxides and phosphates[24]. Interfaces in this thesis are applied using chemical vapor deposition, in which the reaction or decomposition of gaseous precursors produce a uniform, thin coating on a fiber or fabric.

The matrix in a CMC makes up the bulk material and is designed to be extremely stable and have a compatible thermal expansion coefficient with the fiber. The matrix, made from a low density ceramic, provides both structure and protection for the fiber and the interface material, and serves as a means through which energy from mechanical stresses can disperse throughout the composite[25]. In the matrix, the coefficient of thermal expansion (CTE) plays a very important role in the stability and durability of the composite. Large differences in CTE between the fiber and the matrix can result in stresses, cracking, and composite damage during heating and cooling cycles. Low thermal expansion in materials like the SiC-SiC composites fabricated in this research exhibit low rates of expansion and contraction during both heat up and cool down cycles[26].

When the CTE of the matrix is higher than that of the fiber, the matrix expands when heated and contracts upon cooling, gripping and pulling the fiber in a strong bond between the fiber and matrix. Mechanisms allowing for strengthening like fiber pullout or matrix debonding cannot occur, resulting in a brittle material and ultimately failure of the composite. In the inverse scenario, in which the CTE of the fiber was greater than the matrix, the fiber contracts upon cooling, resulting in fiber debonding and gaps between the fiber and matrix, which eliminates the reinforcement properties in the CMC and results in composite failure.

Fiber and matrix CTE match allows for expansion and contraction at similar rates in both components, preventing damage and composite failure[27].

The matrix in non-oxide systems is also specifically designed to protect and provide oxidation resistance to both the interface and fiber. Materials like silicon carbide and silicon nitride have incredibly high melting points and good mechanical properties, even at high temperatures, exhibiting refractory properties excellent for use in CMCs[28]. Silicon carbide has oxidation resistance at temperatures up to 1480°C[29]. At temperatures at or around this point under oxidizing conditions, the outer layer of silicon carbide forms an oxide scale of silica, protecting the bulk material from further oxidation. At even higher temperatures above 1700°C, this silica layer melts and flows via capillary action to fill microcracks formed in the matrix[30]. This unique property makes silicon carbide an excellent material for non-oxide matrices, providing the necessary properties for a strong and durable composite.

Matrices, both oxide and non-oxide, can be applied using a variety of techniques. Hot-pressing methods to apply a matrix are limited by the very high melting point of the ceramics, as well as being limited to simple shapes. This method does produce a matrix with low porosity, good uniformity, and requires only one cycle for densification[31]. Matrices can also be applied using chemical vapor infiltration (CVI), similar to CVD, in which the interface-coated fiber is exposed to gaseous precursors, producing a uniform, relatively dense infiltrated matrix coating. Deposition rate and thickness are controlled to modify the coating porosity and thickness, and complex 3-D shapes can easily be infiltrated with this method[32]. Finally, non-oxide matrices are commonly produced using the Polymer Impregnation Pyrolysis (PIP) method, in which a liquid pre-ceramic polymer is applied to the coated fiber and fully infiltrated into the form using either vacuum infiltration or a series of injections of the viscous polymer to coat the substrate. These polymers are then cured and pyrolyzed, producing ceramics like silicon carbide and silicon nitride[33]. The first heat treatment step in this method cures the polymer at relatively low temperatures below 300°C, producing a “green-body” form. This form is then pyrolyzed at

much higher temperatures (~1600°C), producing a ceramic matrix. The PIP method requires multiple cycles of impregnation to achieve fully densified composites[34].

Applications for CMCs typically exist where high temperature resistance and strength are a necessity. These systems have excellent properties for use in ground vehicles[35], aircraft and aerospace technologies including engine turbines, brake components and both tiles and exterior panels[36]. These lightweight, durable, and refractory systems provide the hardness, toughness, and lightweight nature needed for these types of vehicles. CMCs have shown promise in engine turbine blades, surpassing the operational temperatures of conventional nickel-alloys and allowing for engines to be designed to have more power and run at these extreme temperatures over 1400°C[37]. Ceramic composite systems also have applications for multiple uses in military applications like personal armors[38] and panels in tanks and armored warfare vehicles[39], providing excellent strength and properties against ballistics. CMCs have also been designed for the automotive industry, including passenger vehicles in both brake pads[40], rotors, and clutch components[41]. These composites have excellent wear resistance and provide toughness and durability while maintaining low density. Added weight in any type of vehicle is a disadvantage and the inherent low densities of ceramics makes these systems ideal candidates where weight of the operating system is a factor. Ceramic matrix composites have excellent versatility in a variety of applications and continued development of these materials and systems will lead to further advancements in these fields.

1.3 Chemical Vapor Deposition (CVD)

CVD is used in this research as the method for the deposition of various interface materials, coatings, and thin films. This non-line-of-sight coating process uses gaseous precursors to deposit materials onto substrates which contain regions not directly visible from the deposition source[42]. These precursors were flowed into a heated chamber, decomposing to form a solid on the surface of the substrate. Byproducts were produced and removed from the reactor

through gas flows or low pressure systems. Hot-walled reactors use heating elements to heat the entire deposition chamber and substrate, while cold-wall reactors heat only the substrate through resistive heating processes[43]. CVD can be performed at both atmospheric pressure and at low pressures (LP-CVD) using a variety of precursors and gaseous environments. Coating thicknesses, porosity, and crystalline state can be controlled using precursor flow rates and proportions, reactor temperature, and gas dilutions. Control of the coatings is relativity precise and allows for many variations and options for these films[44]. A significant portion of the CVD performed at the UConn Center of Excellence involves the deposition of a specialized duplex interface material for ceramic matrix composite fabrication. These duplex interfaces, composed of either BN/Si_3N_4 or BN/SiC are typically deposited on ceramic fiber tow or woven fabric and play an essential role in the fabrication of advanced CMCs.

1.4 Chemical Vapor Infiltration (CVI)

Chemical vapor infiltration, while similar in method to CVD, is used for infiltration of a porous substrate. CVI is used in matrix application in CMCs, creating a fully densified, relatively thick matrix on fiber, fabric, or other substrates and providing a strong and durable bulk material for the composite[45]. CVI matrices in this lab are typically composted of silicon carbide, applied to the substrate using methyltrichlorosilane using the same process as in CVD. CVI can be used on complex 3-D shapes, providing a consistent and uniform method for matrix application, and is not limited to silicon carbide or even non-oxide ceramics. CVI can be used for matrix application for a variety of materials including non-oxide ceramics, oxides ceramics, and a variety of other materials[46].

1.5 Polymer Impregnation Pyrolysis (PIP)

Another method used for matrix application is through PIP processing. For this method, a substrate with an applied interface is dipped into and wetted with a liquid pre-ceramic

polymer, using a ceramic filler to improve the density of the resulting composite. This substrate, typically fiber, fabric, or a complex 3-D form is cured to temperatures below 350˚C, forming a green-body composite. From here, the green-body is pyrolyzed at higher temperatures (1100-1600˚C) producing a ceramic char[47]. The fabrication process is described in *Figure 1-3* shows the multiple cycle process for CMC fabrication through this process.

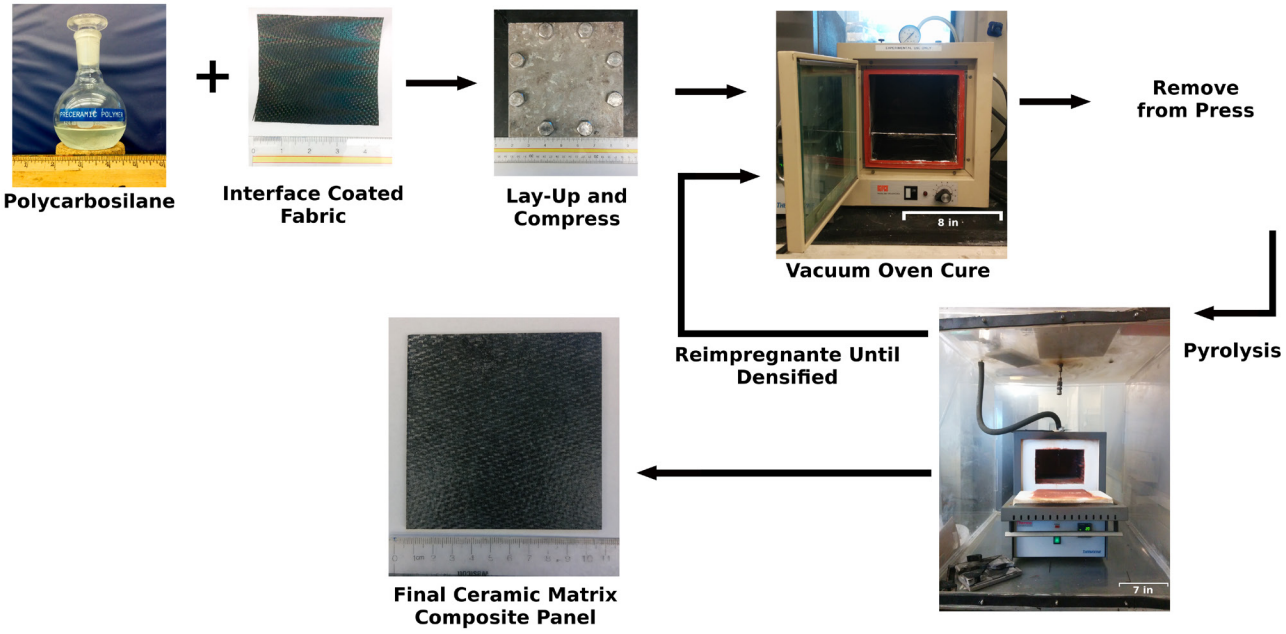

Figure 1-3. Process for Fabrication of a CMC Using the Polymer Impregnation Pyrolysis Process

Polymers used in the PIP method have historically been based off of silicon. These polymers have a wide range of atoms incorporated into the polymer backbone, including metals, carbon and nitrogen, and vary greatly in molecular weight, viscosity, physical and chemical properties, as well as the ceramic resulting from pyrolysis of these polymers. *Figure 1-4*, adapted from Bansal et al, summarizes various silicon based polymers formed with these atoms where M is a metal, demonstrating the versatility of silicon based polymers[48].

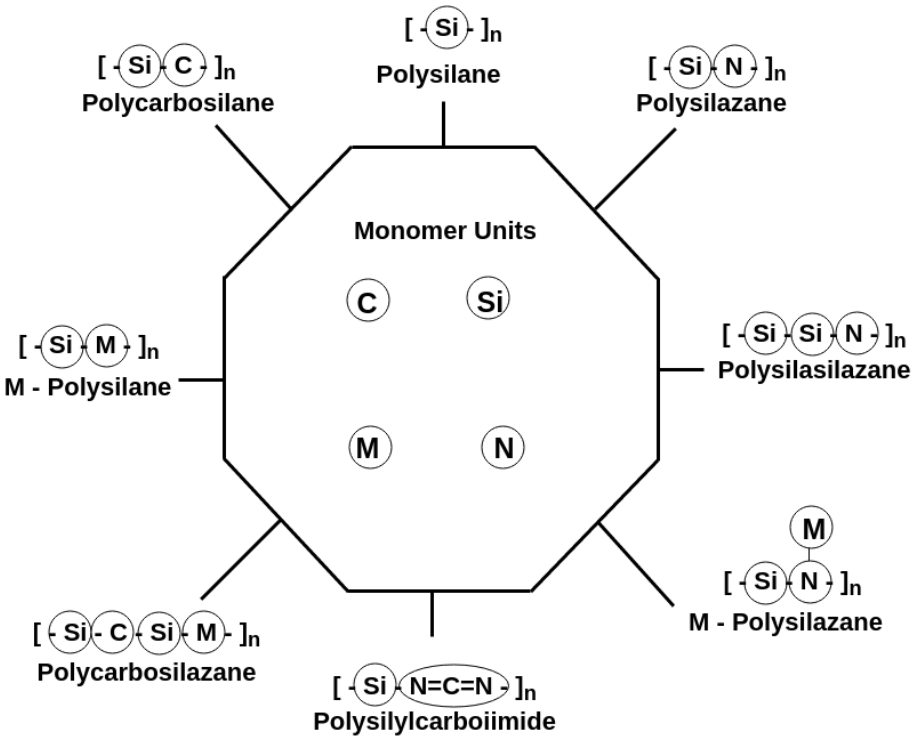

Figure 1-4 Synthetic Pathways to Silicon-Based Pre-Ceramic Polymers[48]

Silicon and carbon based pre-ceramic polymers were the main focus of the research in this thesis, providing stable, near stoichiometric silicon carbide when heated in inert atmospheres. **Chapter 4** also examines the introduction of both titanium and boron into the ceramic system, producing a unique polymer which provided a two-phase crystalline ceramic after heat treatments.

Advantages to using pre-ceramic polymers and the PIP process include ease of processing and the ability to infiltrate complex 3-D shapes in significantly less time than alternatives like CVI[49]. PIP processing required multiple infiltration cycles, however much less time and specialty reactors or equipment is required to achieve a fully densified composite. A composite is considered fully densified when the density no longer increases after impregnation cycles.

Several factors must be considered for effective pre-ceramic polymers, specifically silicon-carbide based polymers. These materials typically produce stoichiometric or near-stoichiometric silicon carbide, reducing the oxidation susceptibility of these materials. Ceramics with free carbon or free silicon are much more prone to oxidation than ceramics comprised entirely of

silicon carbide[50]. Another consideration is Ceramic Yield, or the residual mass of ceramic left over after the polymer has been pyrolyzed[51]. Polymers with high ceramic yields retain more of their mass, reducing porosity and shrinkage in composites. These pores, as well as material contraction which occur during the cure process negatively effect the strength of the composite, reducing the durability and increasing crack formation and ultimate composite failure[52].

1.6 Heteroatom Dopants in Pre-ceramic Polymers

Advancements in pre-ceramic polymers are not only dependent on synthesis method but also on modifications to the ceramics produced upon pyrolysis of the polymer. Specific properties like strength, grain size, and high-temperature refractories can be modified through the incorporation of heteroatoms including titanium and boron[53]. The ceramics produced are optimized for specific properties, providing a superior precursor for both fiber production and matrix material in PIP CMCs. Titanium diboride ceramic is valued for its incredibly high melting point of 2970°C, oxidation resistance, and grain growth inhibition properties[54,55].

High-end commercially available fiber Sylramic® is composed of silicon carbide and a small amount of titanium diborde, resulting in small grain size, increased fiber strength, flexibility, and temperature resistance, but is expensive and difficult to obtain in large quantities[56,57]. Production of a polymer which forms a similar combination of silicon carbide and titanium diboride was valued for use in both fiber production, as well as for a matrix material for use in CMCs.

The polymer was designed to incorporate both titanium and boron into the resulting ceramic, producing a strong, durable material with similar properties to the unmodified ceramic. Stability and ease of CMC fabrication were considerations for this process, ensuring the material produced would be simple and effective for use in multiple components in these composites.

1.7 Advanced CMC Applications and Magnetism

Incorporation of magnetic materials in a composite with high-temperature properties was of interest for use in advanced military and aerospace applications[58]. These materials provide a variety of unique characteristics by taking advantage of the inherent properties of magnetic materials. These advanced applications include magnetic sensors, information storage devices, and a variety of synthetic intermediates for other material production[59,60,61]. With the advancement of the multi-layer system fabricated in this research these applications were not limited to room temperature operation, providing expansion of the capabilities of these systems for use in high-temperature environments like those in aircraft and aerospace technologies. Production of a material capable of withstanding hot, oxidizing environments while maintaining magnetic properties and strength would allow for use of these composites under the harsh conditions present during operation.

Current technologies of magnetic composites do exist, but these systems are not capable of withstanding heat or oxidation and are typically designed in a way that incorporates metal filler into the matrix, adding significant weight to an otherwise low-density material[62]. In aircraft applications, mass is significant and must be kept low to ensure the aircraft can still fly efficiently and the addition of extra weight from metal filler puts the composite at a disadvantage.

The system designed was composed of a magnetic cobalt coating, applied as a thin film on low-weight ceramic substrates. This metal was then coated with a two part system of silicon dioxide and silicon carbide, serving as protection from heat and oxidation and allowing the assembled composite to retain both its strength and magnetic properties during oxidation at 800°C. This development showed significant potential for use in advanced composite applications in which magnetism would be beneficial.

1.8 Research Reported in this Thesis

All chemical vapor deposition and infiltration coatings were deposited in our lab at the University of Connecticut. The large and small scale reactors used to deposit these coatings, both interphase, matrix, and others, were designed and developed at the University of Connecticut in this lab. Polymer synthesis and characterization was performed in this lab, and all fabrication, assembly, and mechanical testing of both composites and mini-composites were performed in this lab.

Chapter 2 Chemical Vapor Deposition of Nitride, Carbide, and Boride Based Coatings for CMCS

2.1 Introduction

The purpose of the research described in this chapter was to modify the experimental design of an existing reactor used to depositing nitride and carbide coatings for interphase materials, as well as to design a reactor setup for depositing boride coatings under similar conditions. As discussed in **Section 1.3**, CVD coatings are essential in the development of thin films for use in CMC technology. The CVD described in this section was used for both duplex interface materials, as well as for the design of a protective coating for a metal for use as a fiber material. CVD was used to deposit thin films with excellent uniformity and control of deposition rates. Materials were characterized using XRD to identify phases present in the coatings produced, as well as with SEM to measure coating thicknesses and to observe coating bulk and surface morphologies, as well as visible adhesion properties.

Duplex interfaces have commonly been used at UConn[63,64] as well as in commercially designed CFR-CMCs[65] to provide an interphase material with excellent strengthening properties for the composite materials. Boron nitride is an ideal material for interfaces[66] due to the hexagonal plane structure allowing for solid state lubricant properties. A coating of boron nitride allows for plane slipping, resulting in strengthening mechanisms in the composite like fiber pullout and crack deflection. Despite these beneficial properties of BN as an interphase, a critical limitation of the material is the susceptibility to moisture damage. Boron nitride begins to corrode in the presence of water at temperatures between 800˚C and 1200˚C and

without protection would result in the catastrophic failure of the composite during operation[67]. The reaction equation of boron nitride with water is shown in *Equation 2-1*, below.

$$2BN_{(s)} + 3H_2O_{(g)} \longleftrightarrow B_2O_{3(s)} + 2NH_{3(g)} \quad \text{(Eq. 2-1)}$$

Boron nitride was deposited in a low-pressure CVD reactor using boron trichloride and ammonia in a multi-step process. Coatings produced were between 100 and 1000 nm thick and were deposited on a variety of substrates including silicon carbide fiber.

This moisture sensitivity is overcome through the application of a thin coating of oxidation-resistance ceramic, either silicon carbide or silicon nitride. This thin coating protects the boron nitride during operation at elevated temperatures in oxidizing atmospheres. Both silicon carbide and silicon nitride are inherently oxidation resistant, providing oxidation protection for the BN under high temperature conditions. Silicon nitride was used in the duplex interface system due to the ease of deposition process, low permeability to both oxygen and water, excellent hardness, and excellent chemical resistance[68,69]. Amorphous silicon nitride was deposited using silicon tetrachloride and ammonia, following the reaction in *Equation 2-2*.

$$3SiCl_{4(g)} + 4NH_{3(g)} \rightarrow Si_3N_{4(s)} + 12H_{2(g)} \quad \text{(Eq. 2-2)}$$

An alternate oxidation resistive ceramic coating for the duplex interface was silicon carbide. This material had similar properties to silicon nitride, was relatively simple to deposit using CVD, and was able to protect the boron nitride from moisture damage. Silicon carbide also has excellent mechanical properties, chemical inertness, and thermal resistance. Silicon carbide was deposited using methyltrichlorosilane as the precursor. Methyltrichlorosilane was thermally decomposed in hydrogen following the reaction in *Equation 2-3* [70]. Coatings of CVD non-

oxide ceramics were deposited on top of films of CVD turbostratic boron nitride to create the duplex matrix fabricated and utilized in other sections of this research.

$$2CH_3SiCl_{3(g)} + H_{2(g)} \rightarrow 2SiC_{(s)} + 6HCl_{(g)} + H_{2(g)} \quad \text{(Eq. 2-3)}$$

Chemical vapor deposition was also used to deposit titanium diboride coatings for the protection of molybdenum metal for future use as a fiber material. Titanium diboride has intrinsic physical properties that make it a desirable candidate for high temperature applications. Titanium diboride is an extremely hard, conductive ceramic with high thermal and electrical conductivities[71]. Titanium diboride also has a high strength to density ratio and excellent wear resistance. These properties[72] make titanium diboride an excellent material for CMC applications as both a matrix and fiber material and the focus of this section was to develop an initial coating process for fiber fabrication of TiB_2 coated molybdenum metal. Titanium diboride was deposited using titanium tetrachloride and boron trichloride, according to *Equation 2-4*.

$$TiCl_{4(g)} + 2BCl_{3(g)} + 5H_{2(g)} \rightarrow TiB_{2(s)} + 10HCl_{(g)} \quad \text{(Eq. 2-4)}$$

In the past, similar fibers containing tungsten, silicon carbide, and boron have been investigated for their desirable high temperature properties. BP Fiber (Sigma SiC Fiber, TISICS UK) used a tungsten filament coated with CVD SiC to create a fiber with excellent oxidation resistance. The conventional way of making these silicon carbide filaments typically involved the resistive heating of tungsten wire in an atmosphere containing methyltrichlorosilane (MTS) and hydrogen, producing a silicon carbide coating on a tungsten core[73]. Commercially available BORSIC fibers (United Aircraft) were produced using this process on a boron-coated tungsten core filament[74].

Typical boron fibers were produced through the CVD of boron onto a tungsten filament substrate heated by resistive heating. The filament, typically 0.012 mm in diameter, was heated and continuously pulled through a reaction chamber at 1000-1300°C in the presence

of boron trichloride and hydrogen. The boron trichloride was reduced to boron according to *Equation 2-5*:

$$2BCl_{3(g)} + 3H_{2(g)} \rightarrow 2B_{(s)} + 6HCl_{(g)} \quad \text{(Eq. 2-5)}$$

The resulting fibers were approximately 1% tungsten by volume and the thickness of the boron coating can be controlled by the speed of pulling, flow rate of boron trichloride, and temperature of deposition. During this deposition, the tungsten was boronized, forming tungsten borides by diffusion and reaction of boron with the tungsten core. The core diameter was increased during this process[75]. SICABO, another commercially available boronized tungsten fiber, had a thinner SiC coating than that of BORSIC (BORSIC has about 1 micron[76]). BORSIC also contained more surface carbon than SICABO, but was stoichiometric or silicon rich within 80-90 nm depth. The SICABO fiber was slightly carbon rich in the 150 nm range. These differences in fiber composition were attributed to different coating processes[77,78].

The materials coated in this work provided an introductory study on the behavior of the deposition of titanium diboride at atmospheric conditions on molybdenum foil coupons. Given the success of these coatings, this research can be applied to systems using thin molybdenum[79,80], tungsten, or other material wires to produce coated fibers.

Overall, the deposition processes and material characterization for these nitrides, carbides, and borides was so similar that combining the extensive research performed for these coatings into one section was an appropriate way to encompass all of the results of these studies. Non-oxide ceramic coatings produced using CVD are essential to the fabrication of Ceramic Matrix Composites.

2.2 Experimental

2.2.1 Boron Nitride and Silicon Nitride on SiC Fibers

Nitride based duplex interfaces were applied using a hot-walled Low Pressure Chemical Vapor Deposition Reactor, depicted in *Figures 2-1 and 2-2*.

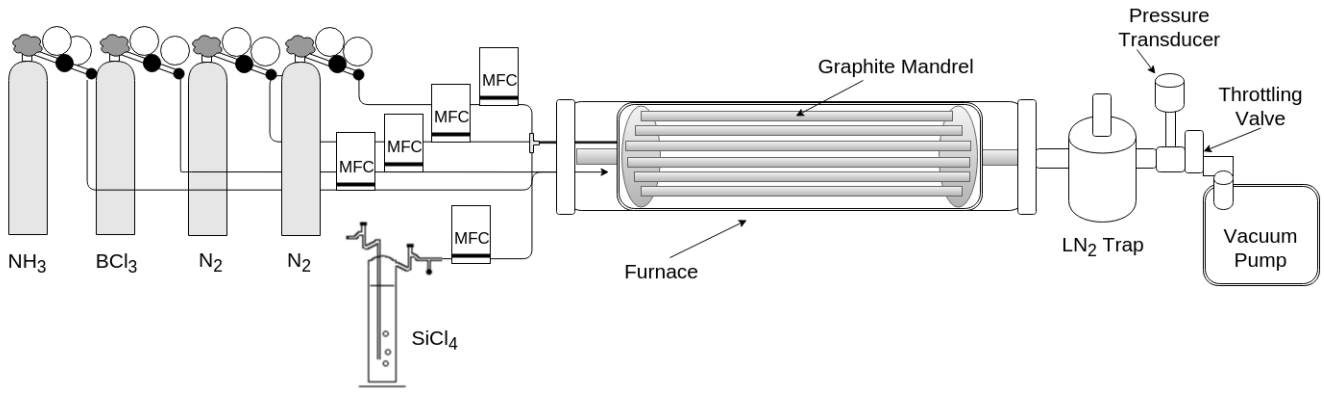

Figure 2-1. Schematic of LP-CVD Reactor Used for Coatings

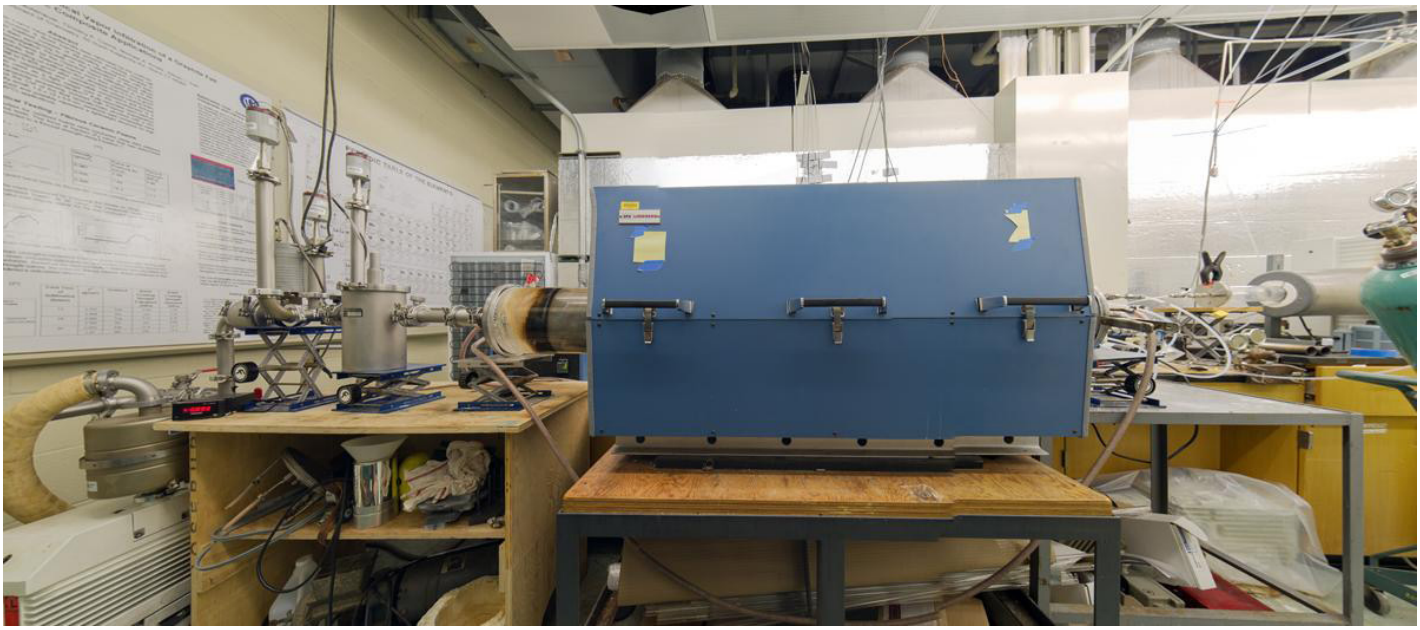

Figure 2-2. Panoramic Photograph of LP-CVD Reactor used for Coatings

The reactor was composed of a Lindberg Blue furnace with a 45" hot zone controlled by resistive heating and three Type K thermocouples arranged in the three zones of the furnace.

25 cm

The temperature limit of the reactor was 1100°C. Gas flows were controlled using MKS mass flow controllers with a MKS 647C Mass Flow Readout and low pressure was maintained at 0.1 kPa using an MKS throttling valve coupled with a MKS 622 Capacitance Monometer when required, controlled using a MKS electronic butterfly valve. Pressure was monitored using MKS pressure heads and ultimate low pressure was maintained at $1x10^{-3}$ Torr. Vacuum was provided by a Emerson Motor Company pump (Model #G78597, 60 Hz, 3.00 HP, 1750 RPM, 460 V) equipped with alumina particulate filtration elements and a Midi-Mist™ oil trap. The reactor was affixed with a liquid nitrogen trap before the pressure transducers to trap gaseous byproducts before they reached the pump.

The fused quartz reaction tube was 72" in length and 11" in outer diameter, affixed with fused flanges attached at either end. The tube was fitted with a removable graphite sleeve to protect the quartz from deposited products. Fiber and fabric substrates were wrapped onto graphite mandrel, shown in *Figure 2-1*. Fabric was secured with Toray® Carbon Fibers T300 carbon fiber tow to prevent the substrate from moving from the mandrel. The mandrel was attached to a peg on the front metal flange which was in turn connected to a spinning motor. The mandrel was turned at approximately 5-10 rpm during the coating process.

The front flanges of the reactor were fitted with a notch holding a Kal-Rez O-ring to ensure a good vacuum in the reactor. Kal-Rez was also used to ensure inertness of the O-rings when subjected to corrosive gases. The flanges were also designed with a cooling water coil to prevent overheating of the O-rings during elevated temperature runs.

Substrates for a typical deposition were continuous fiber tow or 2-D fabric like 8HS CG-Nicalon™, wrapped on the graphite mandrel and secured with Toray® T300 fiber tow. The fabric and fiber is received with a coating of polyvinyl acetate or polyvinyl alcohol sizing for

protection during shipping, which much be removed during the heat-up process. This is known as desizing. A typical run for the deposition of a BN/Si_3N_4 interface was performed as follows:

CG-Nicalon™ Fabric (22" x 35") was wrapped around the graphite mandrel and secured with carbon T300 tow. The fabric was loaded into the reactor, and pumped down to an ultimate low pressure of 12 millitorr. The leak uprate of the reactor was determined by closing the ball valve to the pump and monitoring the increase in pressure over one hour. A leak uprate of under 100 millitorr per hour was considered sufficient. The cooling water lines were turned on and the reactor was heated to 800˚C under the conditions shown in *Table 2-1*.

Table 2-1. Warm-Up Gas Flow Conditions for CVD BN Deposition

Gas	Flow Rate (sccm)
NH_3	100
N_2	200
N_2 Through BCl_3 Line	200

Once the reactor reached temperature, the liquid nitrogen trap was filled to trap gaseous byproducts and the AC motor was turned on to rotate the mandrel inside of the tube. A 100 nm BN coating was deposited using the flow rates shown in *Table 2-2*.

Table 2-2. CVD BN Deposition Conditions

Gas	Flow Rate (sccm)
NH_3	500
N_2	400
BCl_3	125

Temperature, flow rate, pressure, and rotation notes were monitored and recorded every fifteen minutes. Liquid nitrogen was added to the cold trap with each reading. After the desired time, the boron trichloride tank was closed and excess ammonia was flowed for 30 minutes to react excess precursors.

The silicon nitride coating was then applied using liquid silicon tetrachloride (Gelest) in a proprietary bubbler. The design of the bubbler is shown in *Figure 2-3*.

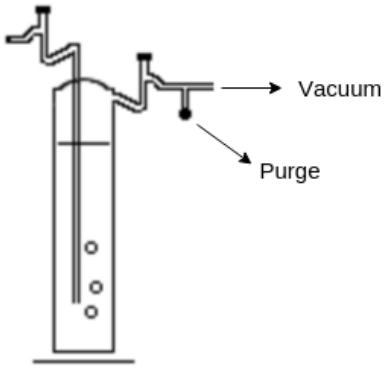

Figure 2-3. Diagram of Bubbler Apparatus for Silicon Tetrachloride Delivery

The right side valve of the bubbler was opened to vacuum and vapors were pulled from the liquid at a rate of 100 sccm Heating tape wrapped around the bubbler was used to help control the flow rate. All gas flow parameters used are summarized in *Table 2-3*.

Table 2-3. CVD Silicon Nitride Deposition Parameters

Gas	Flow Rate (sccm)
$SiCl_4$	100
N_2	400
NH_3	400

After 30 minutes, the valve to the bubbler was closed and excess ammonia flowed to react all excess precursors. The ammonia flow was turned off and the reactor cooled to room temperature under flowing nitrogen. The reactor was backfilled with nitrogen to return to atmospheric pressure and the fabric was removed. A small section of fiber was removed from each the front and back ends of the fabric for analysis.

2.2.2 Boron Nitride and Silicon Carbide on SiC Fibers

The same reactor described in **Section 2.2.1** was used to deposit a BN-SiC duplex interface. Boron nitride was deposited according to the same procedure, using the same warm up conditions for desizing of the fiber. After the BN was deposited, the reactor was cooled and cleaned. The

fabric was flipped, rewrapped with T300 on the graphite mandrel, and loaded into the reactor. Carbon mesh pads were placed inside the reactor against the flanges to protect the O-rings from heat. The reactor was heated to 1050˚C using the flow conditions in *Table 2-1*.

Once the reactor had reached temperature, the liquid nitrogen trap was filled to trap gaseous byproducts and the AC motor was turned on for rotation. The vacuum pump was throttled to 50.00 torr to control the deposition. The silicon carbide coating was then applied using liquid methyl trichlorosilane (Gelest) in a proprietary bubbler by opening the valve to the bubbler and allowing the vacuum to pull vapors off of the liquid. A flow rate of 100 sccm was controlled with heating tape. All gas flow parameters used are summarized in *Table 2-4* and the deposition was performed for 60 minutes.

Table 2-4. CVD SiC Deposition Parameters

Gas	Flow Rate (sccm)
MTS	100
H_2	400

After the desired time of reaction, the valve to the bubbler was closed and excess hydrogen was flowed to ensure all reactive species were used. The reactor was cooled to 800 under flowing hydrogen and nitrogen before the pressure was unthrotted and the reactor was cooled to room temperature under flowing nitrogen. The reactor was backfilled with nitrogen to return to atmospheric pressure, the fabric was removed, and a small section of fiber was removed from each of the front and back ends of the fabric for analysis.

2.2.3 Titanium Diboride CVD

Titanium diboride was deposited onto Grafoil® (GrafTech, 0.005 inch thickness) and molybdenum foil (Alfa Aesar, 0.005 inch thickness-) at 1050˚C and atmospheric pressure using boron trichloride (Aldrich) and titanium tetrachloride (Alfa Aesar). *Figure 2-4* shows the reactor setup for the deposition of the titanium diboride films.

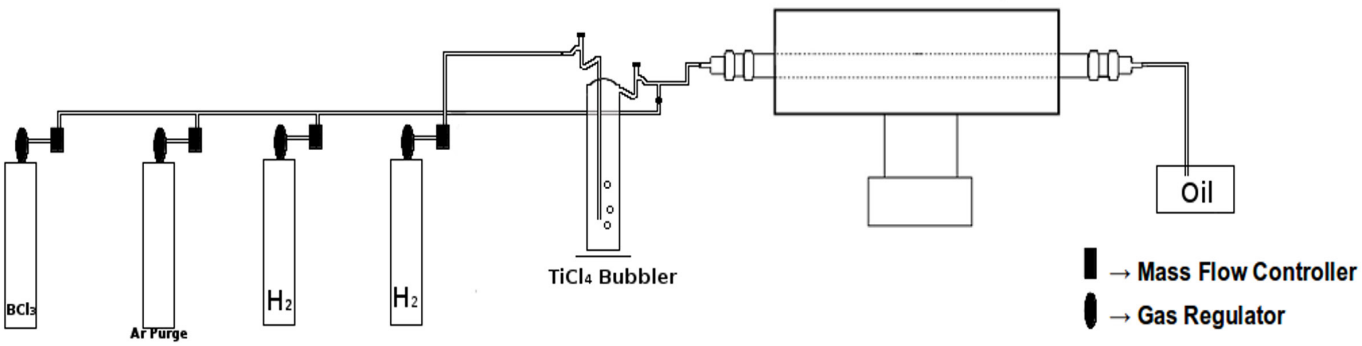

Figure 2-4. Reactor Setup for CVD of TiB_2 at Atmospheric Pressure

The gas flows were controlled by using MKS Mass Flo Controllers (MFC, Model 1179A with Kalrez Seals). The gas was delivered in ¼ inch (conversion) stainless steel tubing and the connections between the quartz tube and the gas lines were made using Cajon™ fittings with Viton elastomer seals. The hot-walled CVD reactor consisted of a Thermolyne™ 21100 Tube Furnace, a 1" quartz (fused silica) reaction tube with a Grafoil® liner to protect the tube from reacting with the precursors. The byproduct gases were vented into an oil trap that was treated with potassium hydroxide to neutralize the gaseous hydrogen chloride byproduct.

In a typical deposition run, the reactor was first heated to 1050°C under flowing argon (100 sccm, UHP, Airgas) to purge the entire system of air and moisture. After the furnace reached deposition temperature, the argon was replaced with the flowing reactant hydrogen gas (UHP, Airgas) at a rate of 50 sccm. After equilibrium was achieved (30 minutes), the reactive gases were introduced. Titanium tetrachloride was added to the system by bubbling hydrogen through reagent grade titanium tetrachloride held in a glass bubbler at a rate of 100 sccm. The two sources of hydrogen served as both a diluent and as a carrier for the liquid $TiCl_4$. At the same time, boron trichloride was also introduced into the reactive chamber at a rate of 30 sccm. Coating thicknesses were controlled by varying deposition time. After determining the proper ratios of titanium tetrachloride and boron trichloride required to produce crystalline titanium diboride, these parameters were used for the remainder of experiments. The resulting

coatings showed a 7 cm deposition zone near the front end of the reactor. Reaction parameters are summarized in *Table 2-5*.

Table 2-5. Experimental Conditions and Deposition Parameters of CVD TiB_2

Run ID	BEG001	BEG002	BEG003	BEG004	BEG005
Furnace Temperature (°C)	1050	1050	1050	900	800
Argon Purge (sccm)	100	100	100	100	100
Hydrogen (sccm)	50	50	50	50	50
Boron Trichloride (sccm)	30	30	30	30	30
Hydrogen through $TiCl_4$ (sccm)	100	100	100	100	100
Deposition Time (min)	15	30	60	30	30
Resulting Coating Thickness Average (μm)	1.696	2.553	4.598	2.221	No Significant Coating Observed

2.3 Characterization

All materials and coatings were examined for crystalline phases using X-Ray Diffraction patterns obtained using a Rigaku Ultima IV X-Ray Diffractometer with a Cu Kα X-Ray source with a beam voltage of 44 kV and 40 mA beam current. Scans were performed from 10 to 80° with a scan rate of 2.0°/min. X-Ray diffraction patterns and phases were verified by JCPDS and Rigaku RINT2200 XG Software.

All materials and coatings were characterized using either a FEI Nova NanoSEM 450 Scanning Electron Microscope with a Everhart-Thornley Detector and with X-Max 80 Silicon Drift Detectory or a Zeiss DSM 982 Gemini FE-SEM with a Schotty Emitter with a voltage range of between 2.00 to 4.00 kV and a beam current of 1 -2 mA. Coating thicknesses and coating adhesion were investigated using SEM .

Energy-Dispersive X-Ray Spectroscopy was performed using an Oxford Instruments EDS with Aztec Instruments Nanotechnology Microanalysis System. Map scans were performed at a working distance of 5.3 mm with a Process Time of 4 and High Voltage at 0.2 kV.

2.4 Results

2.4.1 Optical Observations

Optical photographs of the BN-Si_3N_4 and BN-SiC coatings showed color variation and banding typical with thin films produced via CVD. Photographs of the two duplex coatings are shown in *Figures 2-5 and 2-6*.

Figure 2-5. Photograph of BN-Si_3N_4 Duplex Interface Coating on SiC Fabric showing Color Banding

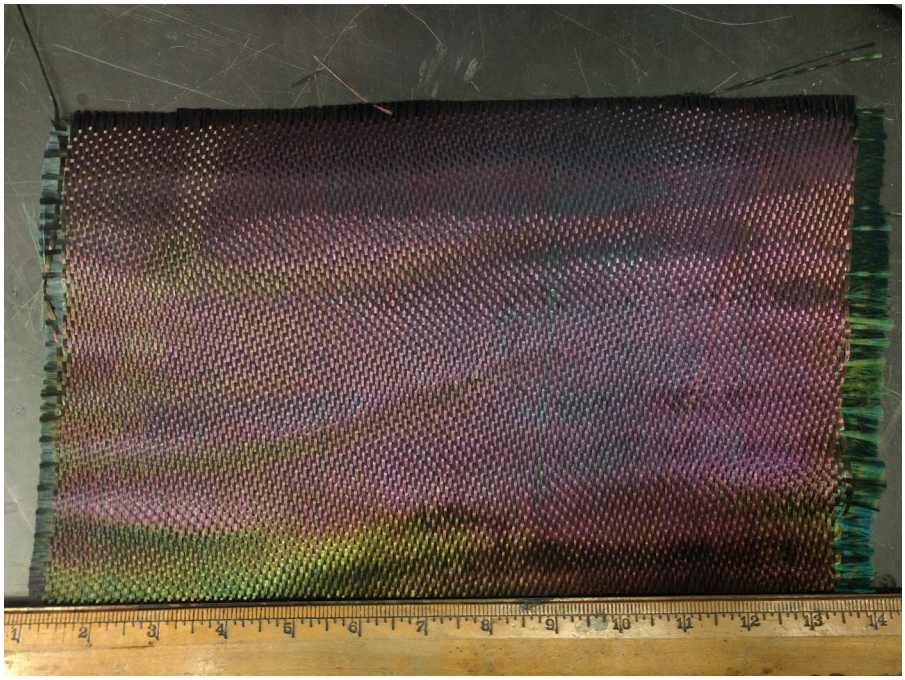

Figure 2-6. Photograph of BN-SiC Duplex Interface Coating on SiC Fabric showing Color Banding

The CVD TiB_2 coatings exhibited slight birefringence as well, though the area of interest for the protective coating was where the coating was dark grey on Grafoil™.

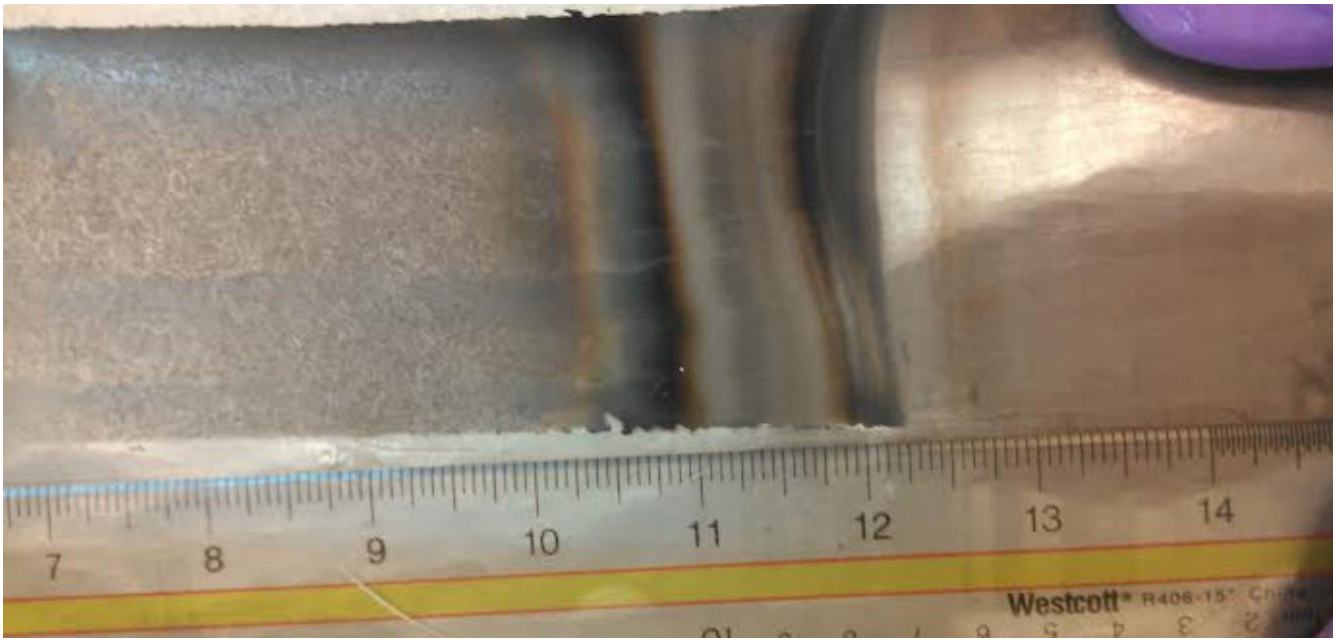

Figure 2-7. CVD TiB_2 on Grafoil Showing Slight Color Banding and Ceramic Coating on Left Side

2.4.2 X-Ray Diffraction

2.4.2.1 Boron Nitride and Silicon Nitride

The diffraction pattern for CG Nicalon™ fabric coated with boron nitride and silicon nitride showed only broad, amorphous signals. These signals could not be indexed to either boron nitride or silicon nitride and the spectra were not included because it did not provide relevant data.

2.4.2.2 Boron Nitride and Silicon Carbide

The diffraction pattern for CG Nicalon™ fabric coated with boron nitride and silicon carbide showed only broad, amorphous signals that could not be indexed to either boron nitride or silicon carbide. The spectra did not contain any conclusive data and were not included.

2.4.2.3 Titanium Diboride

Diffraction patterns were obtained for titanium diboride deposited on both Grafoil and molybdenum foil. The pattern for TiB_2 on molybdenum foil is shown in *Figure 2-8* and the diffraction peaks for are summarized in *Table 2-6*.

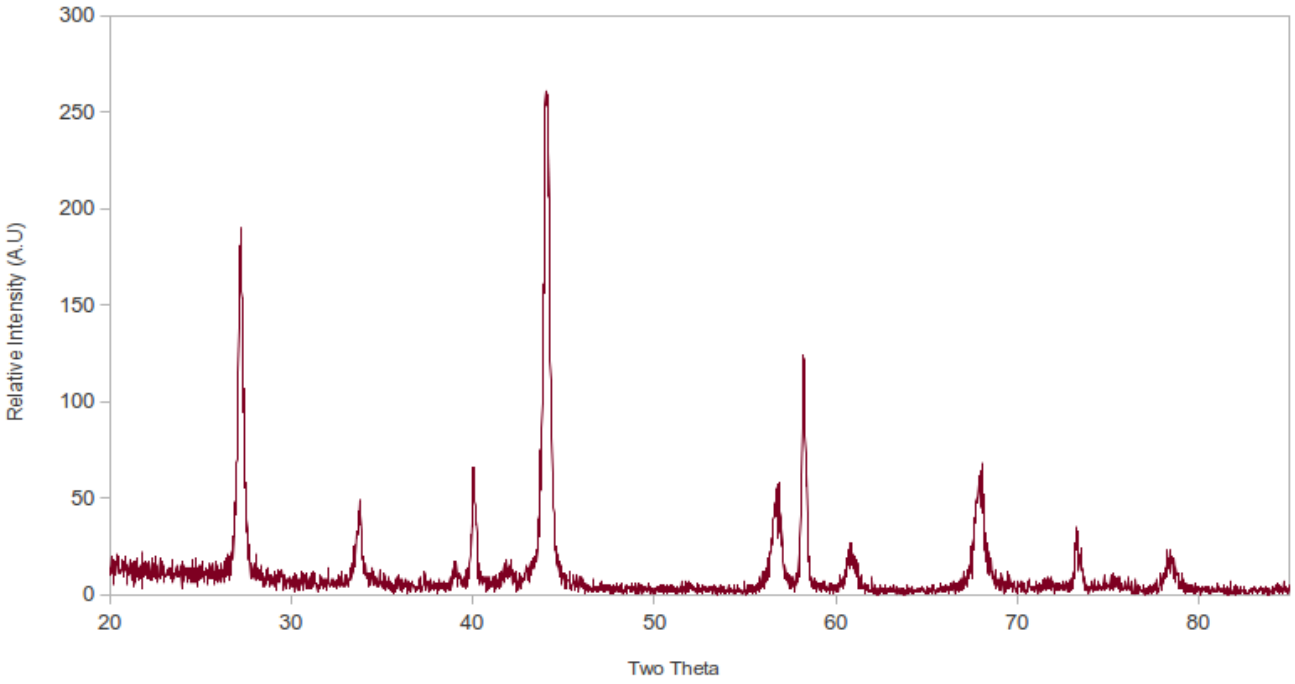

Figure 2-8. Diffraction Pattern of CVD TiB_2 on Molybdenum Foil

Table 2-6. Summarized 2θ Values for XRD CVD TiB_2

CVD TiB_2 on Mo Foil
27.22
33.76
40.10
44.08
56.88
58.22
60.80
68.08
73.26
78.40

2.4.3 Scanning Electron Microscopy

SEM was used to determine the bulk properties of the produced coatings including texture, quality, and morphology. The micrographs were also used to quantify the thickness of the coatings that were produced.

2.4.3.1 Boron Nitride and Silicon Nitride

Micrographs of duplex boron nitride and silicon nitride coatings are shown in *Figure 2-9* below.

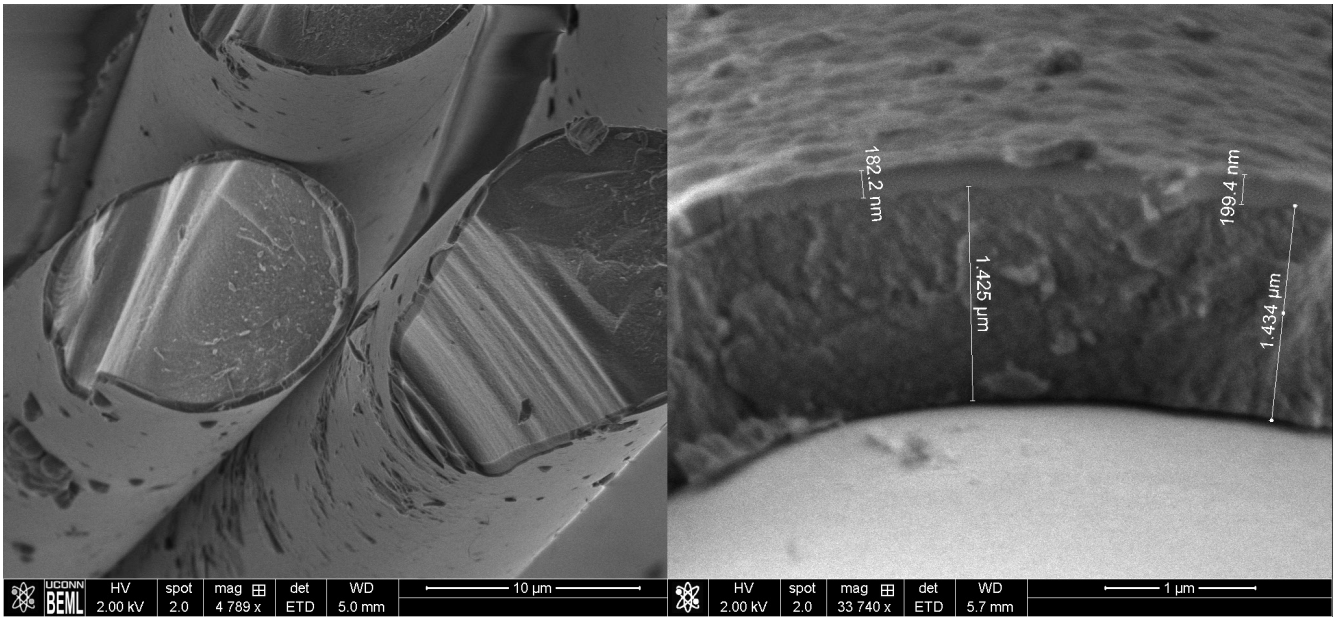

Figure 2-9. Micrographs showing CVD BN and Si_3N_4 Coatings on Ceramic Fibers

These coatings showed good adhesion to the fiber, as well as uniformity in thickness across the material. The coatings were not peeling or flaking in areas and the surfaces of the materials were relatively smooth and free of large clumps of excess material. Coating thickness was adjusted by increasing or decreasing the time, and these values were used to assemble the plot shown in *Figure 2-10 and 2-11*. These data are discussed in detail in **Section 2.5.3.1**.

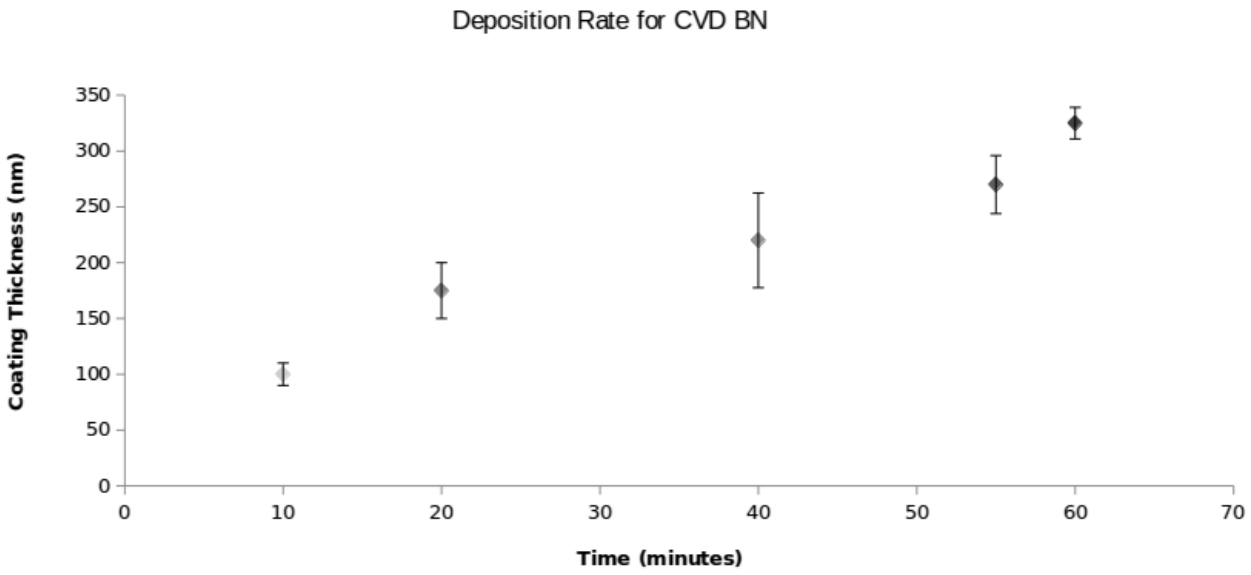

Figure 2-10. Plot Showing Coating Thickness vs. Time of Deposition for CVD BN

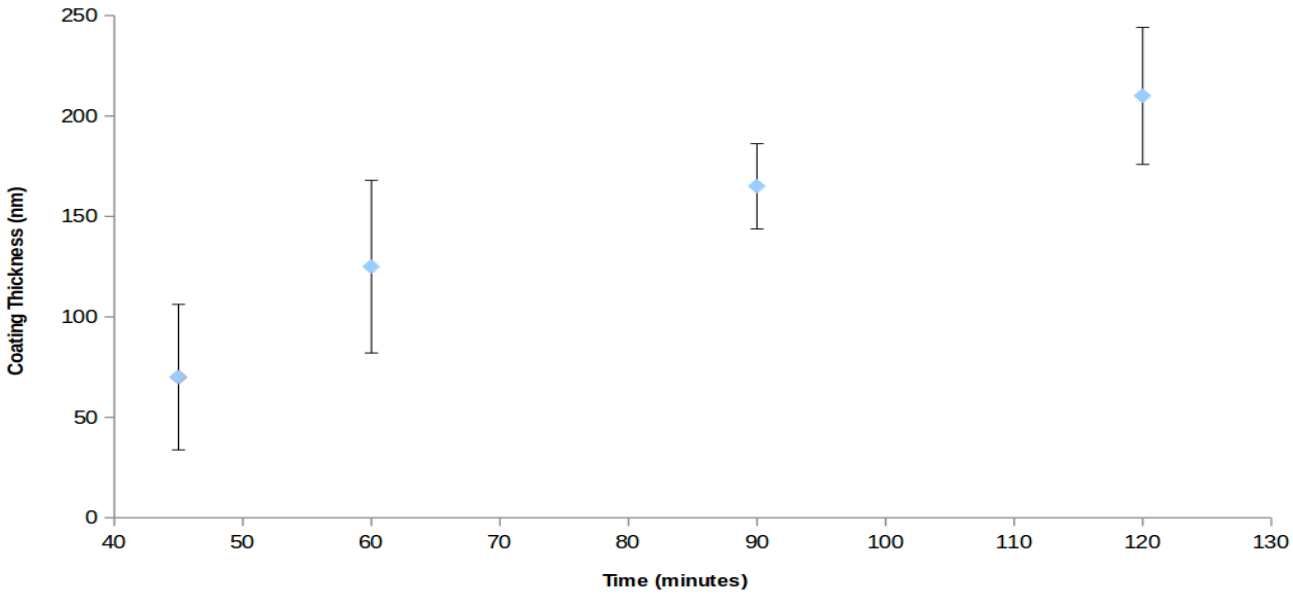

Figure 2-11. Plot Showing Coating Thickness vs. Time of Deposition for CVD Si_3N_4

2.4.3.2 Boron Nitride and Silicon Carbide

Micrographs of the boron nitride and silicon carbide coatings were obtained and are shown in *Figure 2-12* below. The coating deposited showed the fiber, surrounded by a ring of boron nitride and a ring of silicon carbide. Both coatings were well-adhered to the fiber and showed no gaps or areas of flaking. The coatings were smooth and relatively uniform, showing consistency across the sample.

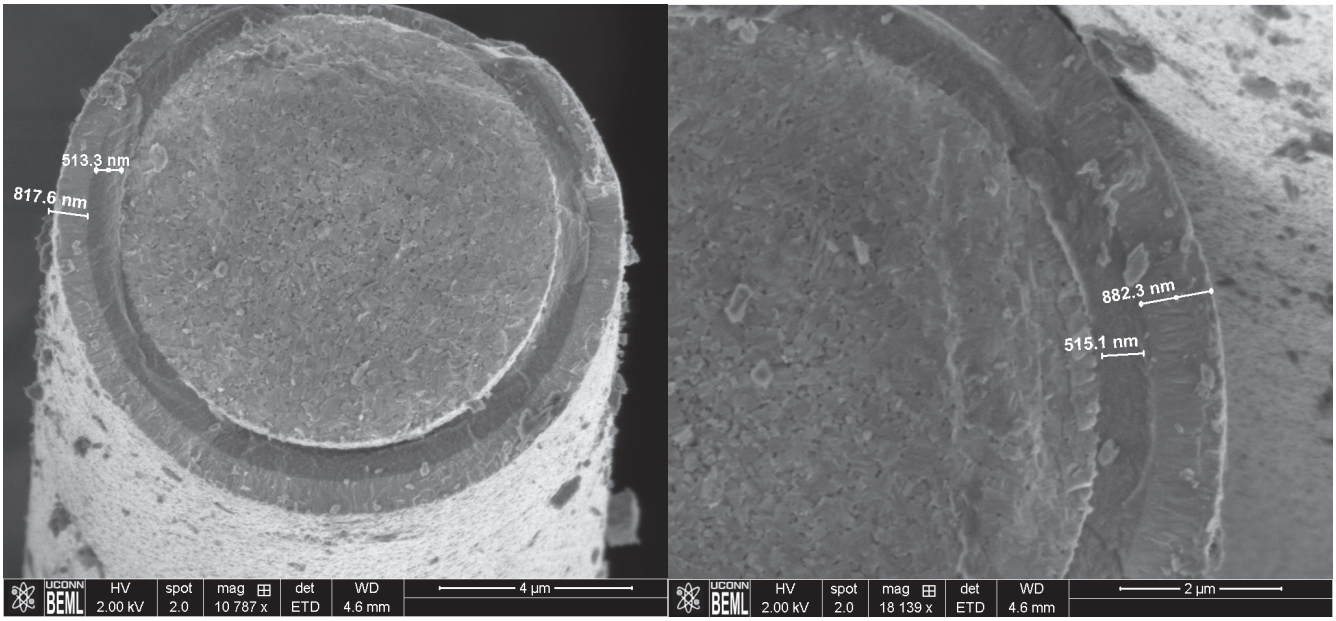

Figure 2-12. Micrographs showing BN SiC Coatings Applied Using CVD

Micrographs of multiple samples were used to generate a thickness plot, seen in *Figure 2-13*, below. The plot for the deposition rate of BN was shown above in **Section 2.4.3.1**.

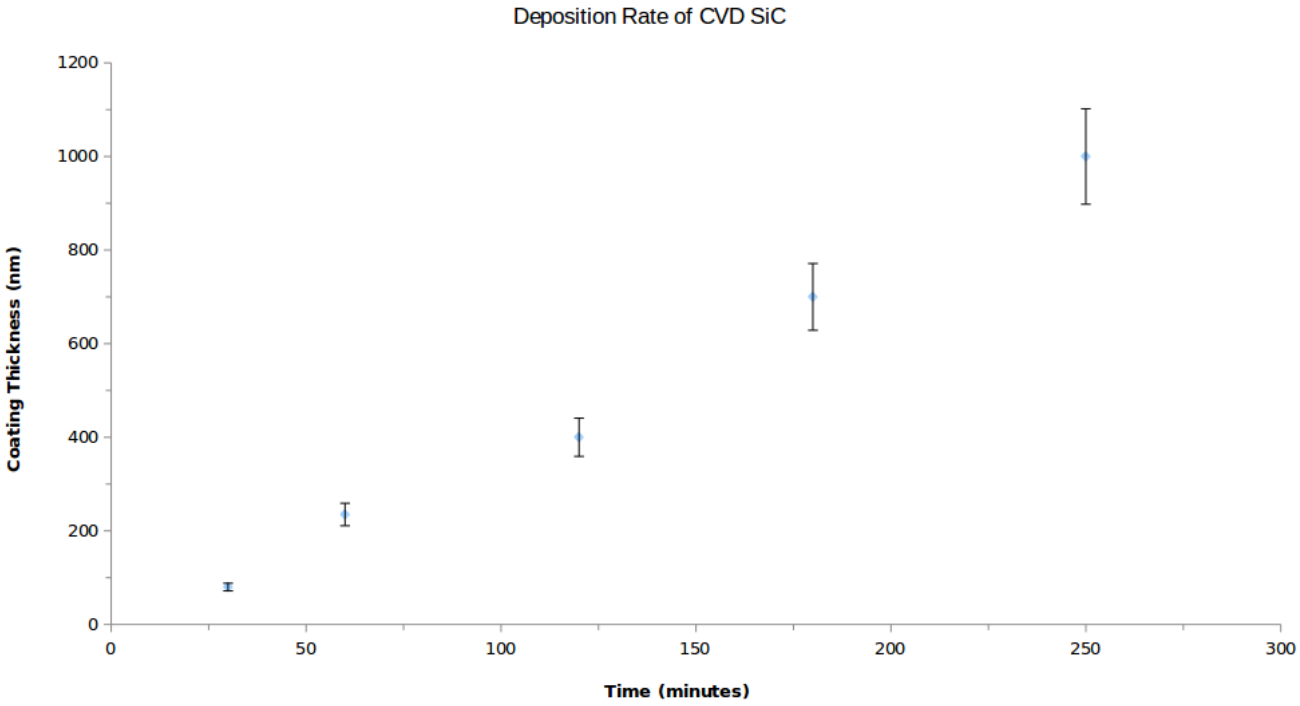

Figure 2-13. Plot Showing Coating Thickness vs. Time of Deposition for CVD SiC

2.4.3.3 Titanium Diboride

TiB_2 films of molybdenum metal were characterized using SEM to determine the surface morphology of the coating, as well as to determine the coating thickness across a cross section. These micrographs are shown in *Figures 2-14 and 2-15* below. Surface morphology of the CVD TiB_2 coating showed flake-like clusters across the entire micrograph with good uniformity and no uncoated regions. The cross sectional micrograph showed excellent adhesion with no areas of coating separation. Measurements were marked using the Oxford Software and a plot of coating thickness versus time of deposition is shown in *Figure 2-16*.

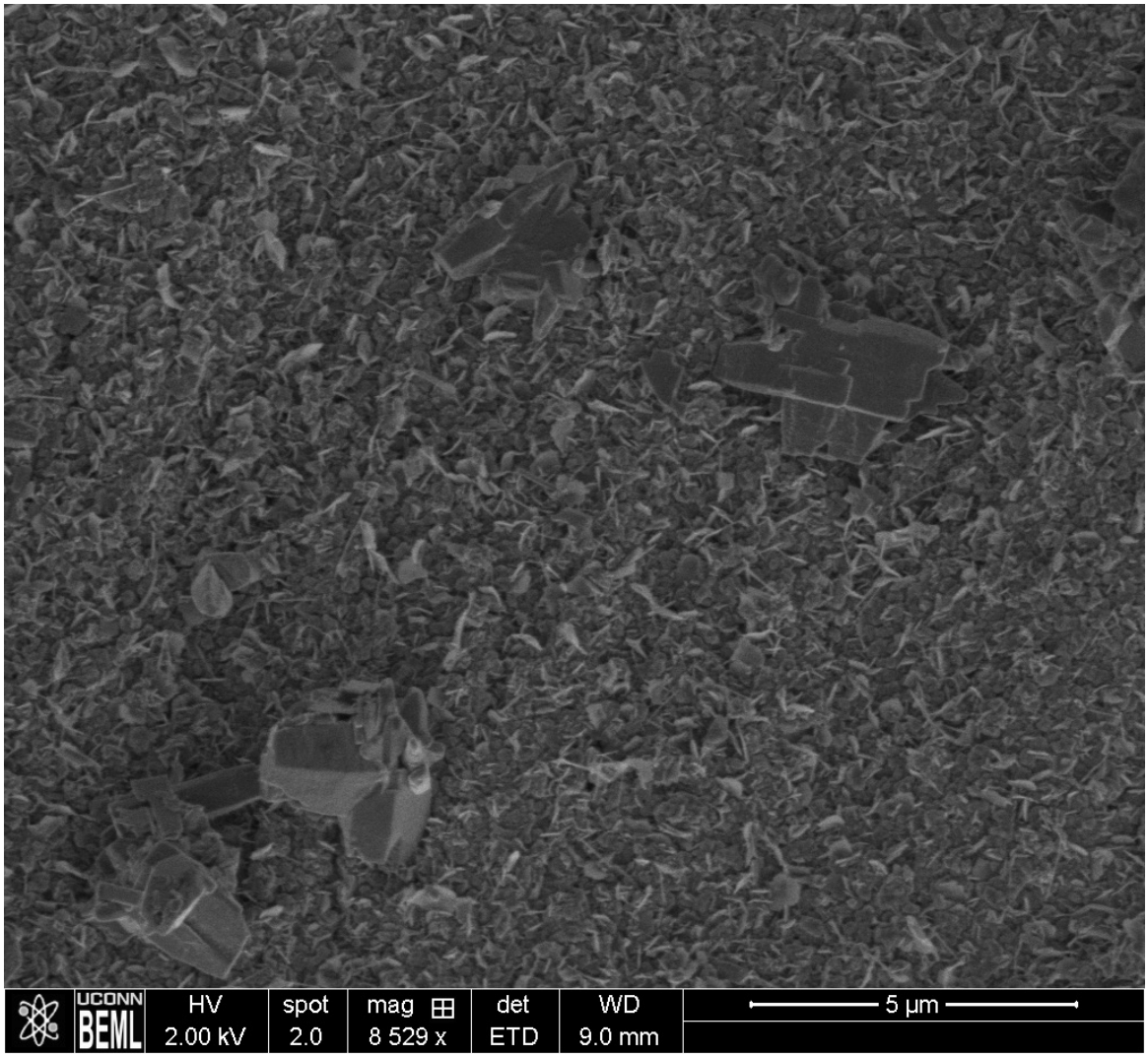

Figure 2-14. SEM of CVD TiB_2 Showing Uniform Coating Across Mo Foil

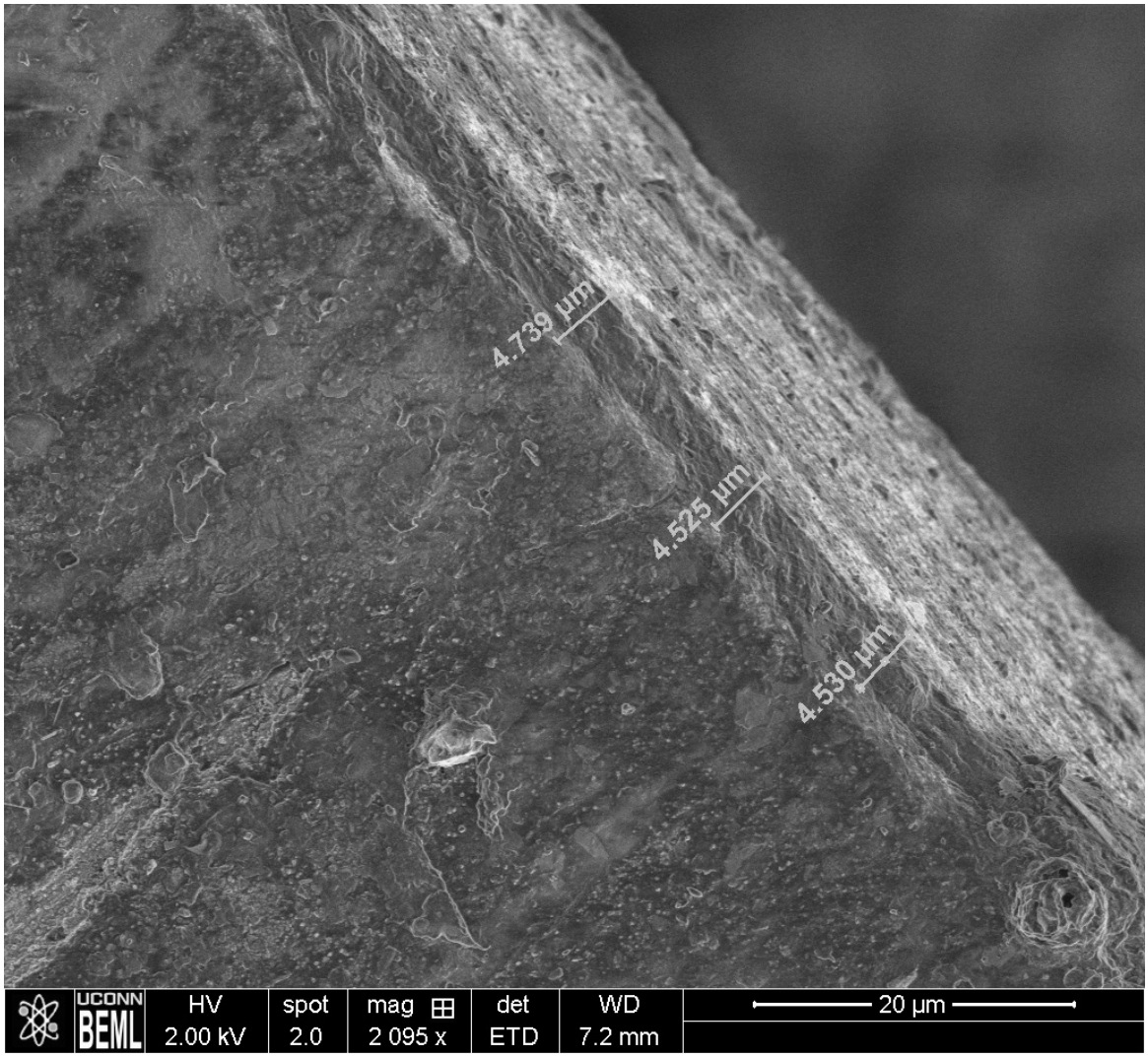

Figure 2-15. Cross Sectional Micrograph of CVD TiB_2 Film on Mo Foil

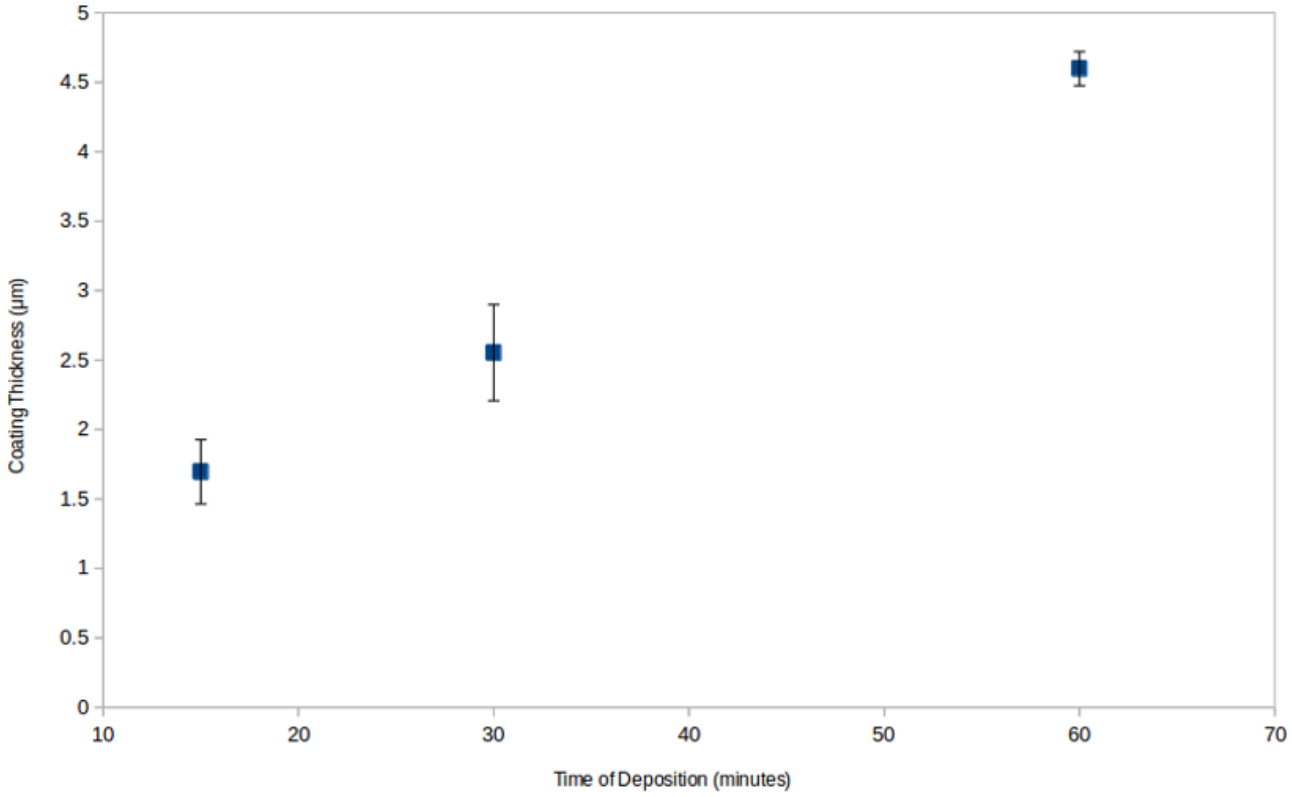

Figure 2-16. Plot Showing Coating Thickness vs. Time of Deposition of CVD TiB_2

2.5 Discussion

2.5.2 X-Ray Diffraction

2.5.2.1 Boron Nitride and Silicon Nitride and Boron Nitride and Silicon Carbide

The diffraction patterns for CG Nicalon™ fabric coated with boron nitride and silicon nitride, as well as boron nitride and silicon carbide showed only broad, amorphous signals that could not be indexed to either boron nitride or silicon nitride. The very broad signals correlated the most to the silicon carbide reflections for the (1 1 1), (2 2 0), and (3 1 1) planes due to the

microcrystalline silicon carbide in the CG Nicalon™ fiber. This result was consistent with the expected amorphous turbostratic boron deposited at 800°C described in previous studies performed with the system used, as well as silicon nitride deposited at the same temperature 34, 46, 63, 64 .

2.5.2.2 Titanium Diboride

Diffraction patterns for the titanium diboride coatings deposited on molybdeum foil were indexed to titanium diboride and molybdenum foil with no evidence of other phases indicating boronization of the metal. The signals were sharp and narrow, indicating a high degree of crystallinity. The signals for molybdenum were clearly distinguished under the TiB_2 coating due to the relatively thin film deposited on the metal. The diffraction pattern with labeled reflections is shown in *Figure 2-17*, and the reflections were indexed to JCPDS cards in *Tables 2-7 and 2-8*.

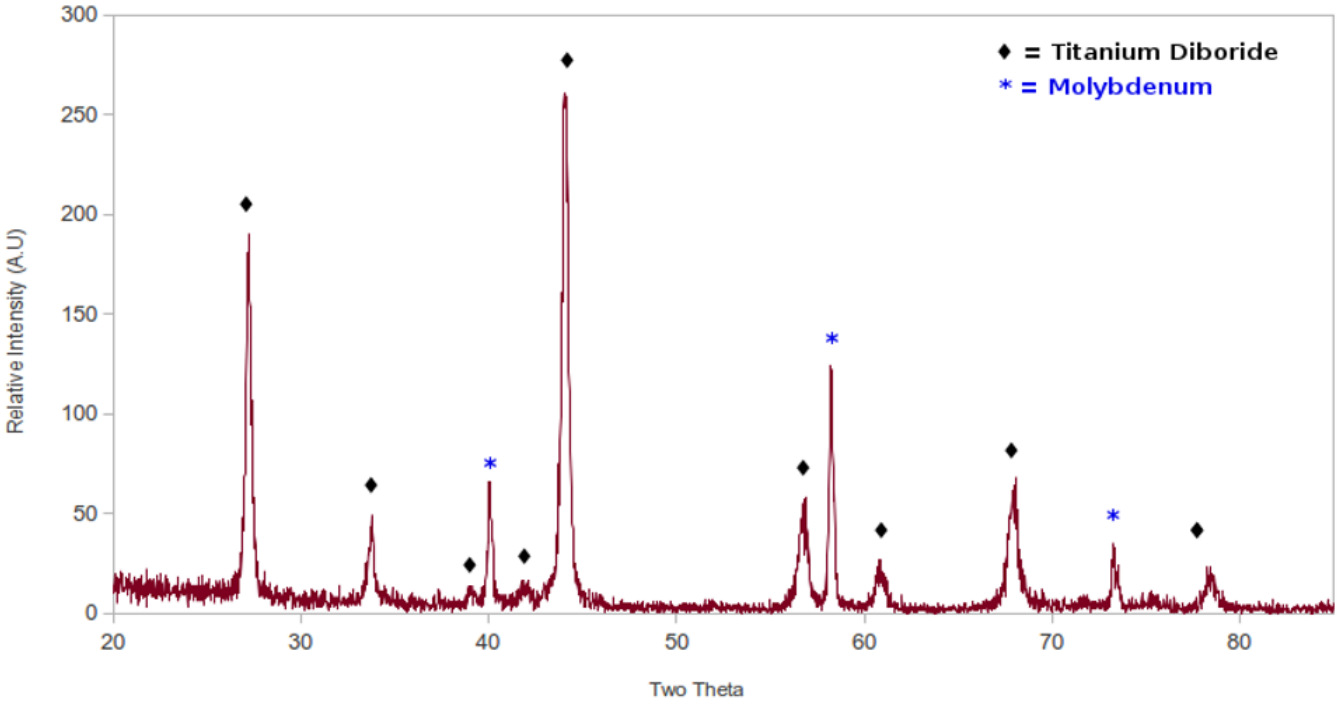

Figure 2-17. Labeled Diffraction Pattern of CVD TiB_2 on Mo Foil

Table 2-7 JCPDS vs. Experimental Reflections for Molybdenum in CVD TiB_2 Coated Mo Foil

	Molybdenum		Experimental	
(h, k, l)	2θ	I/I_0	2θ	I/I_0
(1, 1, 0)	40.19	100	40.10	53.20
(2, 0, 0)	58.15	21.30	58.22	100
(2, 1, 1)	73.05	39.0	73.26	26.60

DB Card No. 01-075-0254

Table 2-8 JCPDS vs. Experimental Reflections for TiB_2 in CVD TiB_2 Coated Molybdenum Foil

	TiB_2		Experimental	
(h, k, l)	2θ	I/I_0	2θ	I/I_0
(0, 0, 1)	27.68	20.0	27.22	73.0
(1, 0, 0)	34.20	60.0	33.76	18.8
(1, 0, 1)	44.53	100.0	44.08	100
(0, 0, 2)	57.05	14.0	56.88	47.7
(1, 1, 0)	61.16	20.0	60.80	10.4
(1, 0, 2)	68.20	16.0	68.08	26.2
(2, 0, 1)	78.69	14.0	78.40	8.80

DB Card No. 00-008-0121

2.5.3 Scanning Electron Microscopy

2.5.3.1 Boron Nitride and Silicon Nitride

Micrographs of CG Nicalon™ fabric tows coated with BN and Si_3N_4 showed both coatings with clear definition from the fiber. The coatings were slightly different in tone due to the differences in chemical composition. Coatings were dense, with no porosity between the fiber and at the interfaces of the films. Both the BN and Si_3N_4 were relatively uniform across the entirety of the fiber and showed good adhesion to both the fiber and at the coating interfaces. Coatings showed no signs of spallation or peeling, indicating an excellent coating with no moisture damage. Surface morphology was relatively smooth with some impurities across the

surface potentially arising from sample preparation, but no large clumps along the surface of the fibers were seen, indicating complete desizing and no moisture damage.

Micrographs of coatings produced with different times of deposition were used to create plots of Coating Thickness vs. Time of Deposition for both boron nitride and silicon carbide to determine the rate of deposition. The plot for BN, shown in *Figure 2-18*, indicated a relatively linear trend in which longer time resulted in longer coating times. The error in each point varied between the coating times and ultimately was reasonable for this type of coating system. The R^2 value of 0.95 indicated a less than perfect fit of the linear curve, however with the error in these types of measurements and coatings, the proposed equation was still beneficial to future experiments in which a specific coating thickness was required.

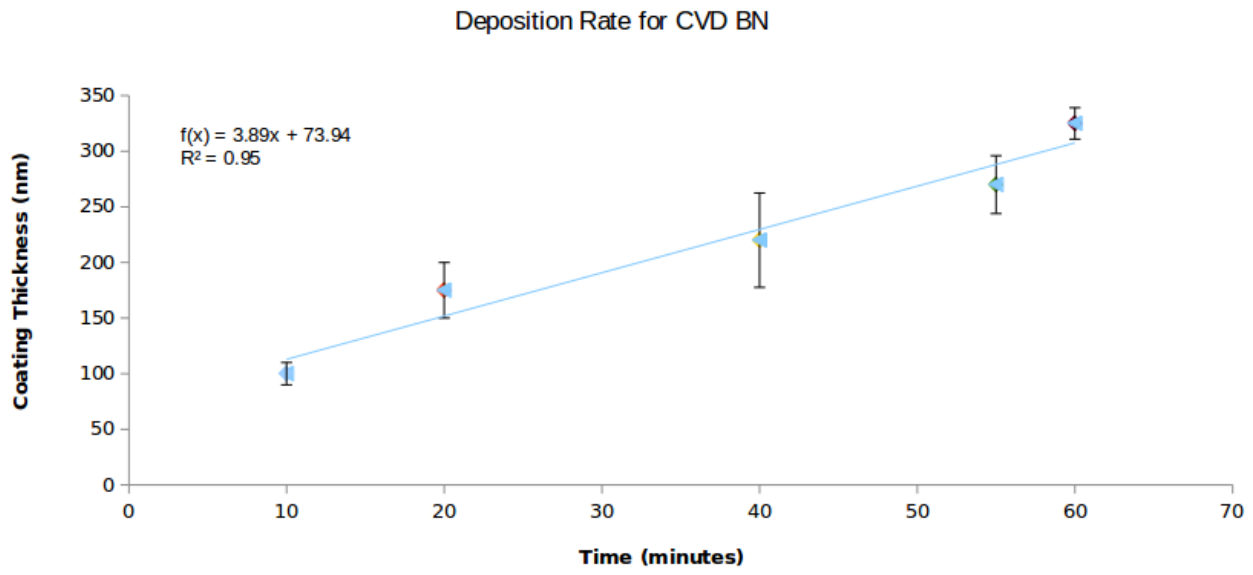

Figure 2-18. Plot Showing Coating Thickness vs. Time of Deposition for CVD BN with Equation

A similar plot was constructed for the silicon nitride component of the duplex interface. This plot, showing coating thickness versus time, is shown in *Figure 2-19* below.

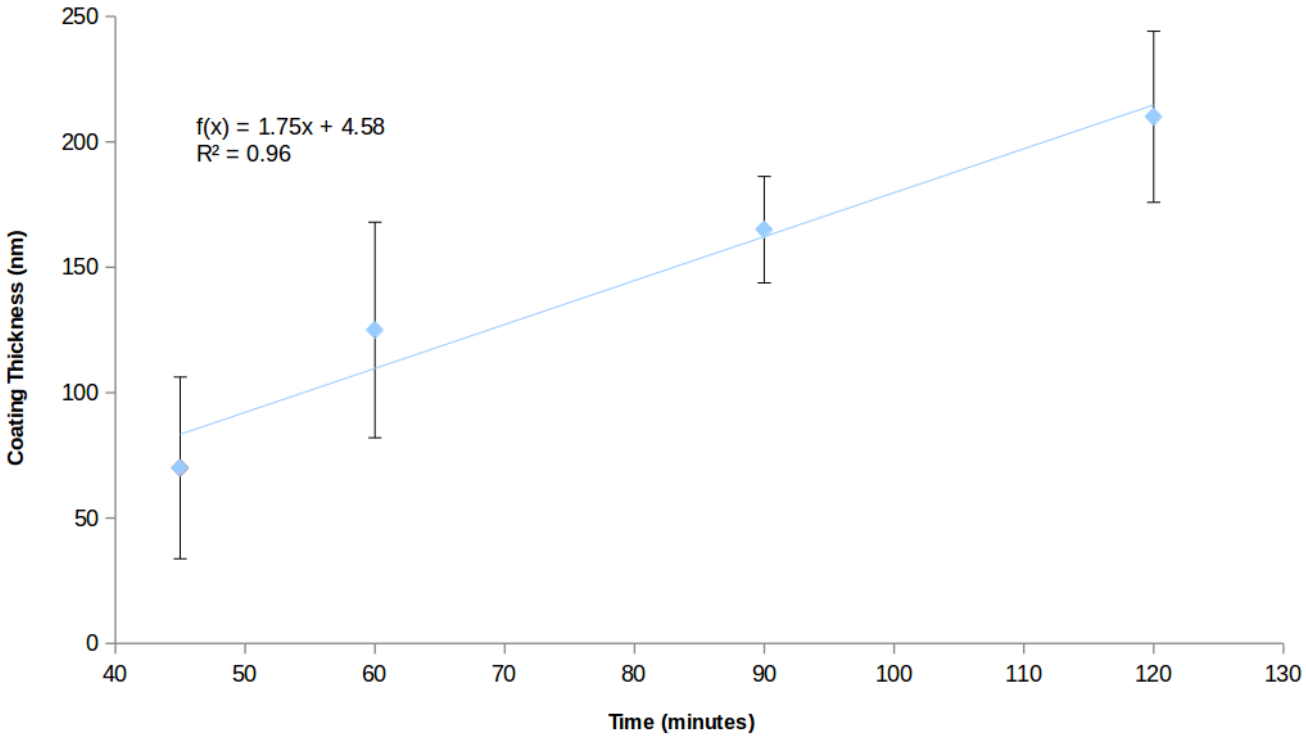

Figure 2-19. Plot Showing Coating Thickness vs. Time of Deposition for CVD Si_3N_4 with Equation

The plot again shows a near-linear correlation of coating time and coating thickness, as expected with CVD reactions. The error bars in the plot were larger and the curve fit was signified by and R^2 value of 0.96, which was likely due to less sample data being used for plot construction. These values had some inevitable variation due to the nature of coatings produced with CVD, but overall the proposed equation had a relatively good fit and will benefit future experiments in which coating thickness is set and time of reaction must be determined.

2.5.3.2 Boron Nitride / Silicon Carbide

CG Nicalon™ Fabric tows coated with BN and SiC were examined using SEM. The micrographs showed evidence of both coatings, clearly visible by a difference in grey tone. The coatings appeared solid and dense, with no evidence of holes or porosity in the coatings. Interfaces between fiber and BN, as well as between the BN and SiC were clean and showed no

evidence of separation. There were no gaps in the coating interfaces, indicating good adhesion. Both coatings were relatively uniform in thickness across the entire perimeter of the fiber and surfaces of the coatings were smooth with minimal imperfections.

Micrographs of coatings produced with varied time of deposition were again used to create plots of Coating Thickness vs. Time of Deposition for silicon carbide to determine the rate of deposition. The plot for SiC, shown in *Figure 2-20*, showed a linear correlation of deposition time and coating thickness consistent with the other coating rates of the duplex interface materials. The error in each point increased with the thickness of the coating, suggesting that the longer the coating, the more variation in the coating produced. The R^2 value of 0.99 indicated relatively good fit with the linear equation. As in the case with the other plots, this equation will provide beneficial information to experiments in the future in which the time of coating required to produce a specified thickness must be determined.

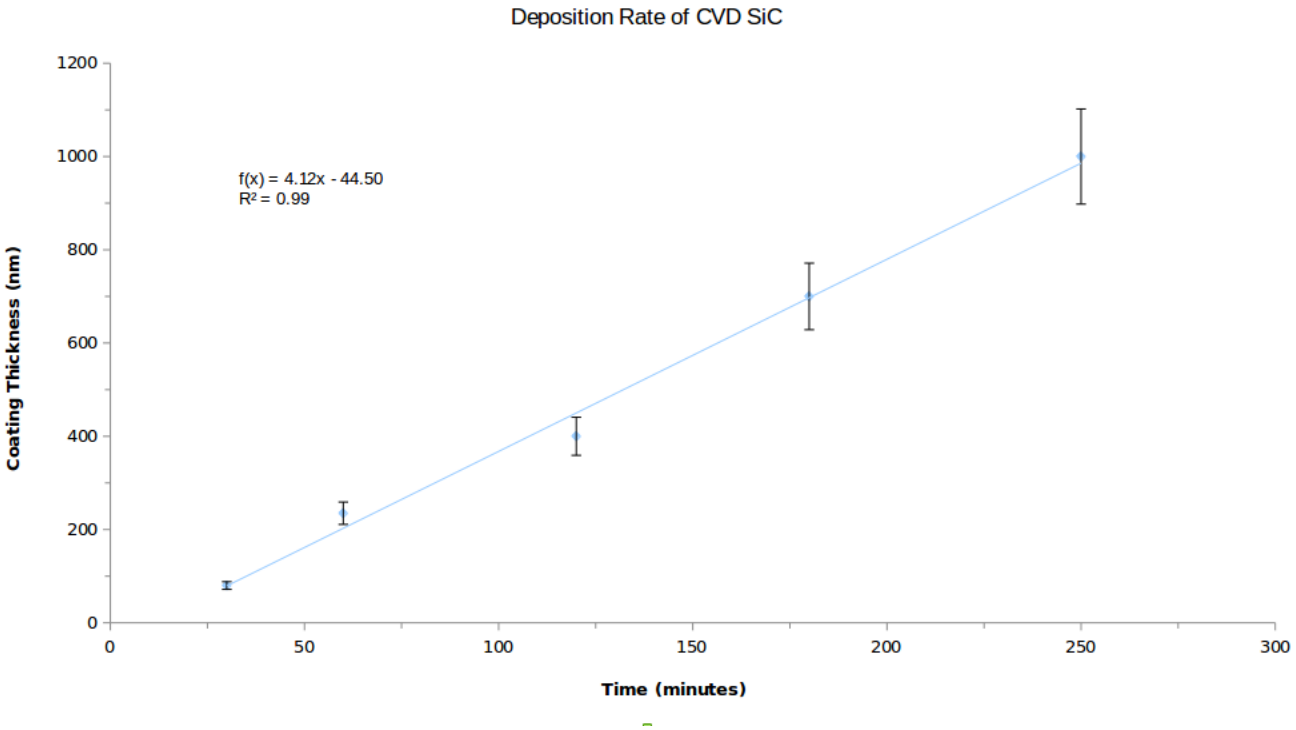

Figure 2-20. Plot Showing Coating Thickness vs. Time of Deposition for CVD SiC with Equation

Finally, the observation was made that the slopes for all three duplex interface materials were relatively similar. The values, shown in *Table 2-8*, indicated a similar rate of deposition between the three ceramics. This similarity was likely due to the initial experimental design of the reaction parameters and must be considered for future experiments. Rate of deposition ultimately affects coating porosity and in turn strength of the material produced through these methods.

Table 2-9. Slopes of Linear Equations for Deposition Rates of Duplex Interface Materials

Deposition	Slope of Linear Fit Equation (nm/min)
BN	3.89
Si_3N_4	4.58
SiC	4.12

2.5.3.3 Titanium Diboride

Micrographs of the CVD coating show an even, flake-like coating across the molybdenum foil with no large clumps or bare spots evident. The coating showed excellent uniformity across the substrate.

The cross sectional micrograph showed good adhesion. Adhesion is important for the future of this system for use as a fiber which will be subjected to mechanical stresses. Samples were prepared by cutting the molybdenum foil with shears and the TiB_2 coating was still found to bond to the foil despite bending and tearing of the foil during sample preparation. Coatings appear uniform in both texture and thickness in both the Grafoil and as expected with a CVD coating. The morphology of the coating appears to be flake-like clusters, in contrast with the smooth surface of the molybdenum foil.

The coating thickness plot showed a linear correlation between coating thickness and time of deposition. The plot with a fitted curve is shown in *Figure 2-21*. The R^2 value of 1.00 shows excellent linear fit of the equation $f(x) = 0.07x+0.67$. Linear correlation was expected for this type of reaction because coating thickness was directly related to time of deposition and in turn amount of precursor reacting for deposition.

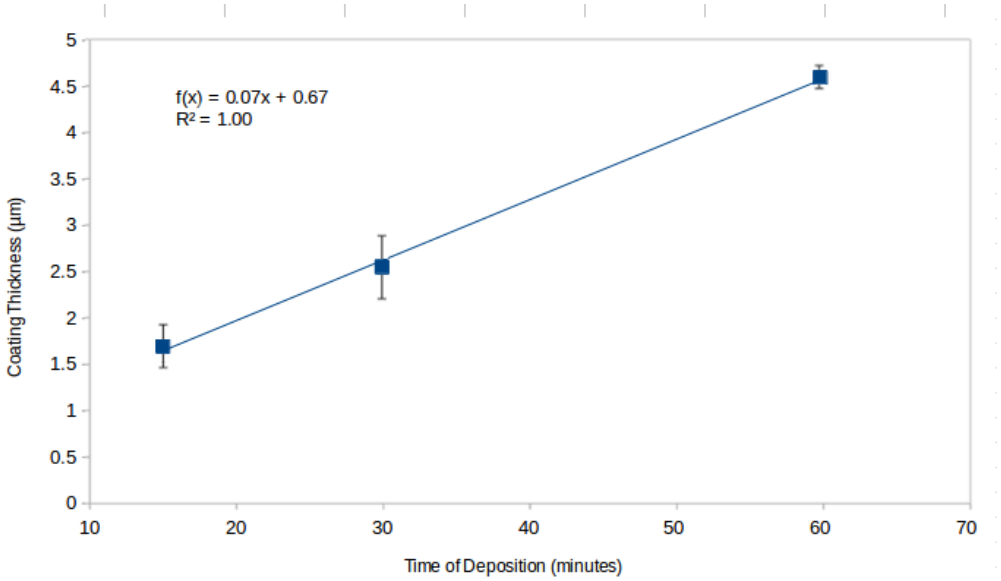

Figure 2-21. Plot Showing Coating Thickness vs. Time of Deposition for CVD TiB_2 with Equation

2.6 Conclusions

Non-oxide ceramics, specifically, nitrides, carbides, and borides, were deposited using CVD on a variety of substrates for multiple uses in Ceramic Matrix Composites. These materials were selected for their inherent high temperature and strength properties, providing structure and strengthening mechanisms in the composite systems. These materials were deposited using CVD, producing thin films with uniformity and excellent visible adhesion properties. Coatings were characterized using XRD to determine crystalline phases present, as well as SEM to examine the coating morphology and adhesion to the substrate. Coating thickness was also examined using SEM and plots of coating thickness versus coating time were designed to determine the relationship between film thickness and time of deposition, as well as to provide a tool for future coating parameters.

Chapter 3 Development of a Polycarbosilane Pre-Ceramic Polymer

3.1 Introduction

Pre-ceramic polymers have shown to be excellent sources for matrix material in ceramic matrix composites and provide a convenient means for this popular technology. Ceramics like silicon carbide are ideal for high temperature applications due to their high strength, thermal properties, and low densities[81]. Application for these polycarbosilanes is for usage in ceramic matrix composites as both a fiber and as a matrix. The polymer can be spun into fibers and pyrolyzed for a reinforcing material, providing amorphous or nanocrystalline silicon carbide and yield increased flexibility, excellent thermal properties and oxidation resistance[82]. The polymer can also be used as a bulk matrix material in the composite, serving as the strength component and allowing for toughening mechanisms when the matrix cracks during use. This matrix is applied using the PIP method and allows for ease of use in composite manufacture[83]. Polycarbosilanes are not limited to CMCs and the material can also be used as a silicon carbide precursor in electronics, semiconductors, films, chemical sensors, or biological applications[84,85,86]. Polycarbosilanes can also be used as a synthetic intermediate to make a variety of composite-like materials. Initial development of these polymers began in the 1970's with the Yajima process and Wurtz Reaction, shown in in *Figure 3-1* [87].

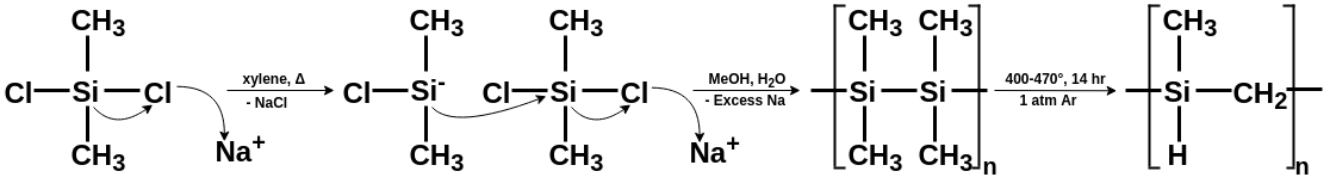

Figure 3-1. Yajima Process for Simple Polycarbosilane Synthesis

This reaction, using dichlorodimethylsilane and sodium metal produced a simple polydimethylsilane product that was insoluble in most organic solvents and proved to decompose entirely at a temperature below the melting point of the solid polymer, limited the polymer essentially useless as a silicon carbide precursor. These problems were overcome through an autoclaving treatment to 450°C under inert atmosphere, resulting in a carbon and silicon atom rearrangement in the backbone through the Kumada rearrangement process[88]. The resulting solid polymer was relatively insoluble in organic solvents and was sensitive to moisture, but paved the way for future development of polycarbosilane and silicon-based pre-ceramic polymers.

These polycarbosilanes function as silicon carbide precursors for multiple uses in a CMC, including spun fibers and bulk matrix resin material in ceramic matrix composites, yielding materials with excellent oxidation resistance at high temperatures, low porosity, and inherent low density[89,90]. The versatility of a liquid polycarbosilane serves as a benefit to multiple components in a CMC, and the use of the polymer is not limited to only composite applications. Typical modern polycarbosilane synthesis involves the Grignard coupling reaction of chlorinated silane precursors, followed by the reduction of excess chlorine[91]. The polymer forms a backbone of alternating silicon and carbon atoms and the degree of branching is dependent on the groups attached to the initial silane precursor[92]. This polymer is then heated in inert atmosphere, burning off volatile side groups and low weight oligamers, leaving only the silicon and carbon as silicon carbide. Polycarbosilanes should yield near-stoichiometric silicon carbide at relatively low pyrolysis temperatures, result in high (> 60%) ceramic yields,

and have limited contaminants[93].

Commercially available polycarbosilanes like Starfire® SMP-10 are widely popular for creating PIP composites[32] and complex 3-D shapes from silicon carbide[94]. Starfire® SMP-10 forms amorphous silicon carbide between 850-1200°C and nano-crystalline β-SiC between 1250-1700°C[95]. This commercially available polymer forms silicon carbide with a 1:1 silicon to carbon atomic ratio. Despite this ease of use, this polymer is expensive, limited quantities are produced yearly, and air stability can be an issue, resulting in lower ceramic yields over time.

The new polymer produced in this research differs from typical polycarbosilanes through the unique usage of specific concentrations of two chlorinated silane precursors and allyl chloride. These two silanes, chloromethyltrichlorosilane and chloromethylmethyldichlorosilane, shown in *Figure 3-2*, were chosen due to the presence of the reactive chloromethyl group and the relatively low cost as compared to other specialty chlorosilanes.

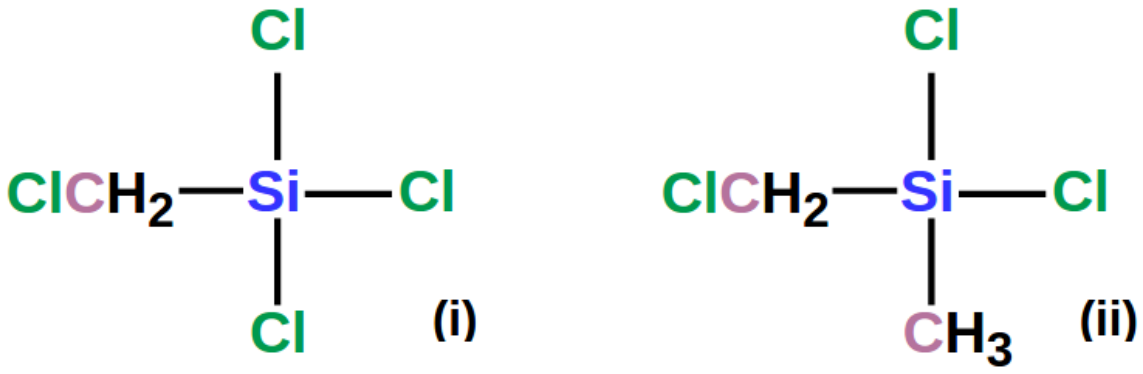

Figure 3-2 Monomers Selected for Polycarbosilane Synthesis: Chloromethyltrichlorosilane (i) and Chloromethylmethyldichlorosilane (ii)

A new branched polymer containing silicon and carbon in the backbone was synthesized from chlorinated silane precursors and allyl chloride. This polymer, which formed near-stoichiometric silicon carbide upon pyrolysis, was designed to be relatively air-stable, have a long shelf life, and have moderate viscosity for ease of use in CMC applications. Pyrolysis of

the polymer yielded microcrystalline β-silicon carbide at 1100°C with ceramic yield of 75%.

3.2 Experimental

3.2.1 Polymer Synthesis

A typical synthesis of the polymer was carried out as follows:

Tetrahydrofuran (THF, Sigma-Aldrich) and diethyl ether (Sigma-Aldrich) were added to a flask under constant nitrogen purge. Magnesium powder was added to the flask and stirred constantly. In a glove box, an addition funnel was filled with chloromethyltrichlorosilane (Cl_3SiCH_2Cl, Gelest Inc.), chloromethylmethyldichlorosilane ($Cl_2Si(CH_3)CH_2Cl$, Gelest Inc.), and allyl chloride (Sigma-Aldrich). The addition funnel was attached to the flask, and slow, dropwise addition of the contents resulted in an immediate, vigorous reaction. After the addition was complete, the suspension was heated with an oil bath to reflux for 16 hours. The resulting precipitate was separated from the solution by suction filtration under nitrogen, and the filtrate was returned to the flask. Lithium aluminum hydride was slowly added to the clear, yellow liquid. Once the addition was complete, the suspension was heated to reflux under nitrogen for 12 hours, filtered under nitrogen again, and an aqueous workup was performed.

The aqueous workup involved the slow addition of 4 M HCl to the polymer under vigorous stir and nitrogen flow. After the reaction had slowed, the liquid was transferred to a separatory funnel and the aqueous layer was removed. The organic layer was rinsed twice with 4 M HCl, separated, and finally the solvent was stripped under vacuum. The resulting viscous, liquid polymer was stored under nitrogen below 4°C for optimum shelf-life.

Pyrolysis of the polymer was performed as follows:

Liqiud polymer was loaded into a ceramic boat into a tube furnace under 100 sccm flowing UHP Argon (Airgas). The sample was heated at 2°C/minute to 1100°C, held for one hour,

and subsequently cooler. Samples heated to 1600˚C were heated at 2˚C/minute to 1600˚C under 100 sccm flowing UHP Argon, held for one hour, cooled to 800˚C at 2˚C/minute, and subsequently cooled.

3.3 Characterization

All polymer materials were characterized with Attenuated Total Reflectance Spectroscopy (ATR) using a Thermo Scientific Nicolet iS5 iD3 with a germanium plate. Temperature studies for ATR were performed by heating the polymer at 10˚C/minute and holding at the maximum temperature for 30 minutes before cooling for analysis.

^{1}H Nuclear Magnetic Resonance (NMR) was performed using a Bruker AVANCE III-400 Mhz, using a total of 16 scans. NMR peaks were assigned from a data library to identify solvent and common contaminants. $CDCl_3$ was used as the deuterated solvent and was mixed in an approximately 10:1 ratio of solvent to polymer solution. Polymer sample was synthesized in THF and the residual solvent from synthesis was not evaporated off to improve solubility for sample preparation.

Polymer samples were analyzed with Thermo-Gravimetric Analysis and Mass Spectrometry (TG-MS) Evolved Gas Analysis using a Netzsch Instruments TG 209 F1 Libra® coupled with a Netzsch Instruments QMS 403D Aëolos Quadrupole Mass Spectrometer. The Netzsch Proteus Software c-DTA® program was used to determine endothermic and exothermic events based on the difference in the theoretical liner temperature rate of heating and the temperature measured at the bottom of the sample crucible. Polymer samples were heated to 830˚C at 10˚C/minute in 50 sccm of argon and MS bar graph scans were performed for masses per charges of 1-50, at a scan speed of 0.2 seconds.

All pyrolyzed materials were examined for crystalline phases using X-Ray Diffraction (Rigaku Ultima IV X-Ray Diffractometer with Rigaku RINT2200 XG Software). Samples were heated at 10˚C / minute and held at the final temperature for 30 minutes in 50 sccm flowing

argon. Voltage settings were 44kv and 40 kv with a scan speed of 2.0 degrees per minute and slits settings of 2/3, 10, 2/3, and 0.3 mm.

All pyrolyzed materials were characterized using either a FEI Nova NanoSEM 450 Scanning Electron Microscope with a Everhart-Thornley Detector and with X-Max 80 Silicon Drift Detectory or a JEOL JSM-6335F Field Emission Scanning Electron Microscope with a voltage range of between 2.00 to 4.00 kV and a beam current of 1 -2 mA. Coating thicknesses and coating adhesion were investigated using SEM .

Energy-Dispersive X-Ray Spectroscopy was performed using an Oxford Instruments EDS with Aztec Instruments Nanotechnology Microanalysis System. Map scans were performed at a working distance of 5.3 mm with a Process Time of 4 and High Voltage at 0.2 kV. Pyrolyzed samples were heated at 10°C / minute and held at the final temperature for 30 minutes in 50 sccm flowing argon, cooled, ground with an alumina mortar and pestle, and mounted on aluminum stubs with conductive carbon tape.

3.4 Results

3.4.1. Attenuated Total Reflectance Spectroscopy

ATR was used to identify functional groups present in the synthesized polycarbosilane. Initial analysis of the liquid polymer provided the spectrum shown in *Figure 3-3*. Distinct signals were observed at 2960 cm^{-1}, 2145 cm^{-1}, 1355cm^{-1}, 1255 cm^{-1}, 1045 cm^{-1}, 935 cm^{-1}, 880 cm^{-1}, and 720 cm^{-1}.

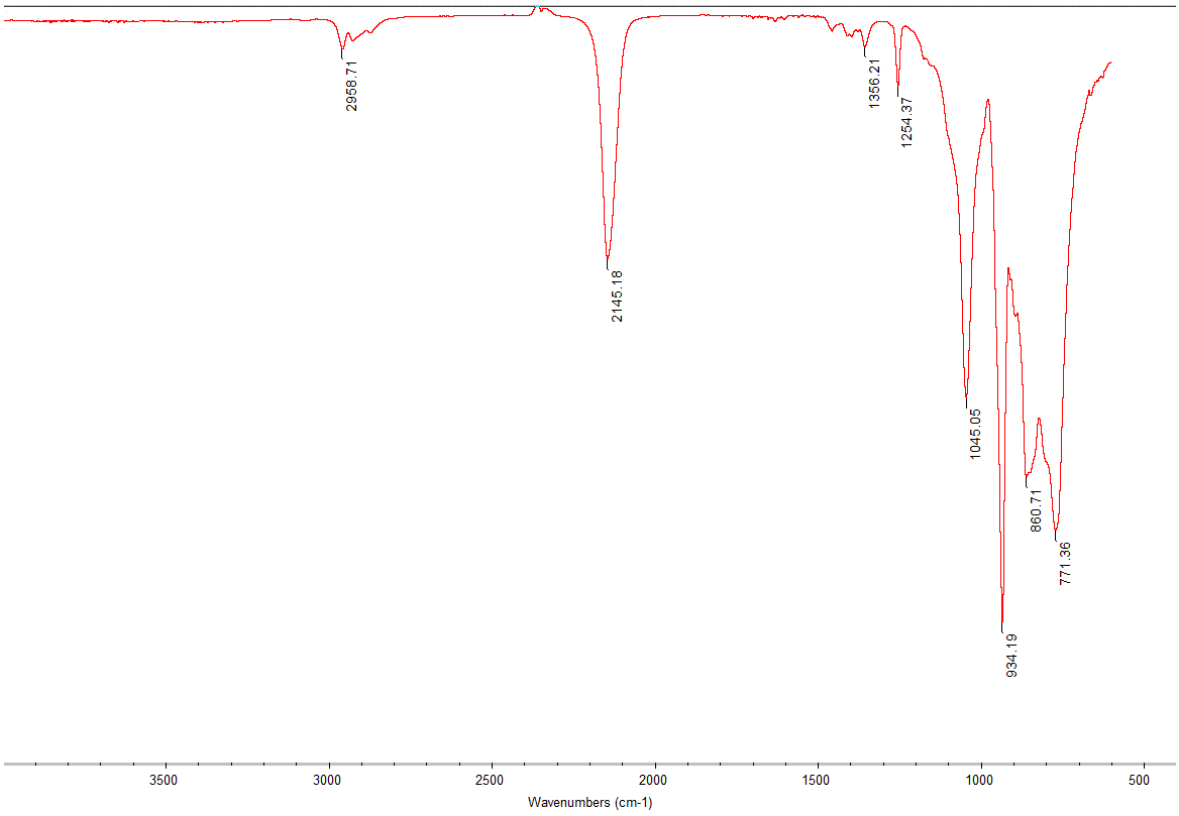

Figure 3-3. ATR Spectrum of PCS Polymer

A temperature study was performed with samples of polymer which had been heated under an argon atmosphere to determine the effect of heating on the presence of functional groups as the polymer was converted to ceramic silicon carbide. Polymer samples were heated to 300˚C, 500˚C, 700˚C, 900˚C, and 1100˚C before being cooled and analyzed. *Figure 3-4* shows the stacked plot of ATR spectra, and these data were summarized and discussed in *Table 3-3*, in the **Section 3.4.2**.

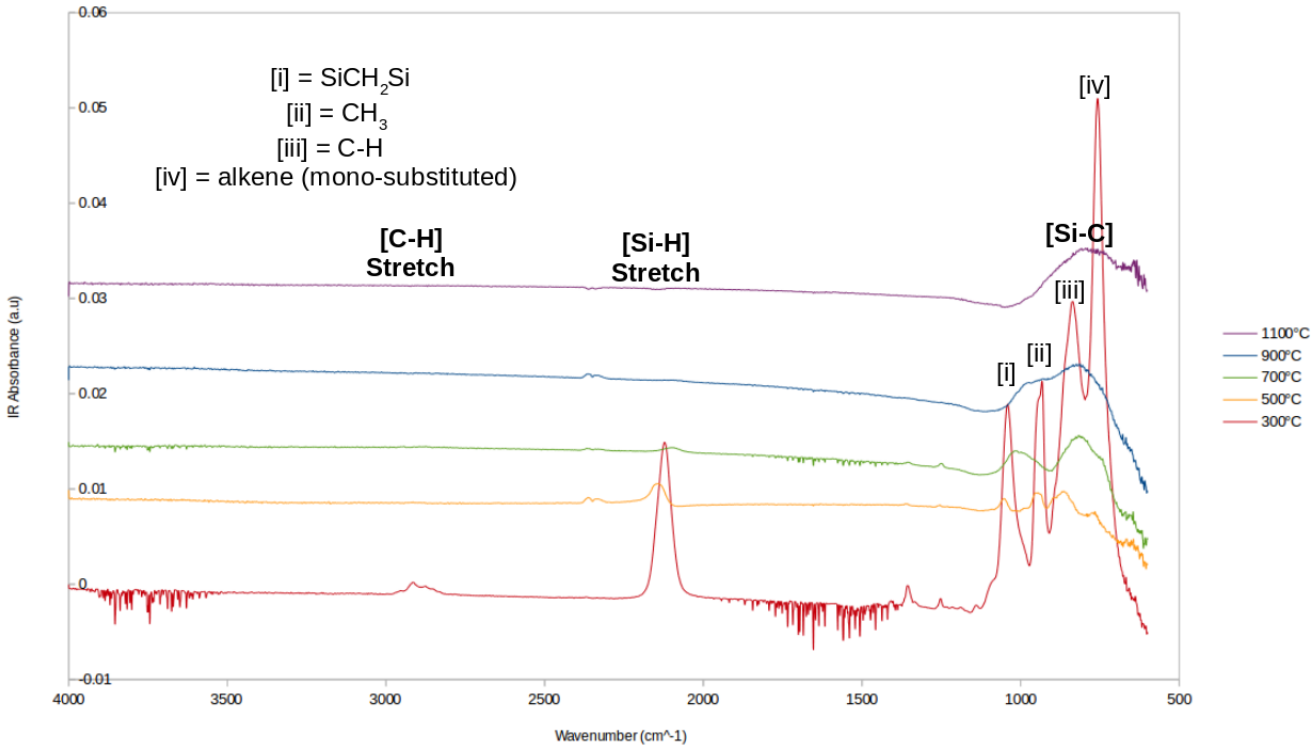

Figure 3-4. ATR Functional Group Study of Polycarbosilane During Heating Process

3.4.2 ^{1}H Nuclear Magnetic Resonance

^{1}H NMR was used to help identify the structure of the polymer and the degree of branching present in the polymer liquid. The spectrum for polymer, dissolved in $CDCl_3$ with residual THF solvent from synthesis, is shown with relevant signals in *Figure 3-5*.

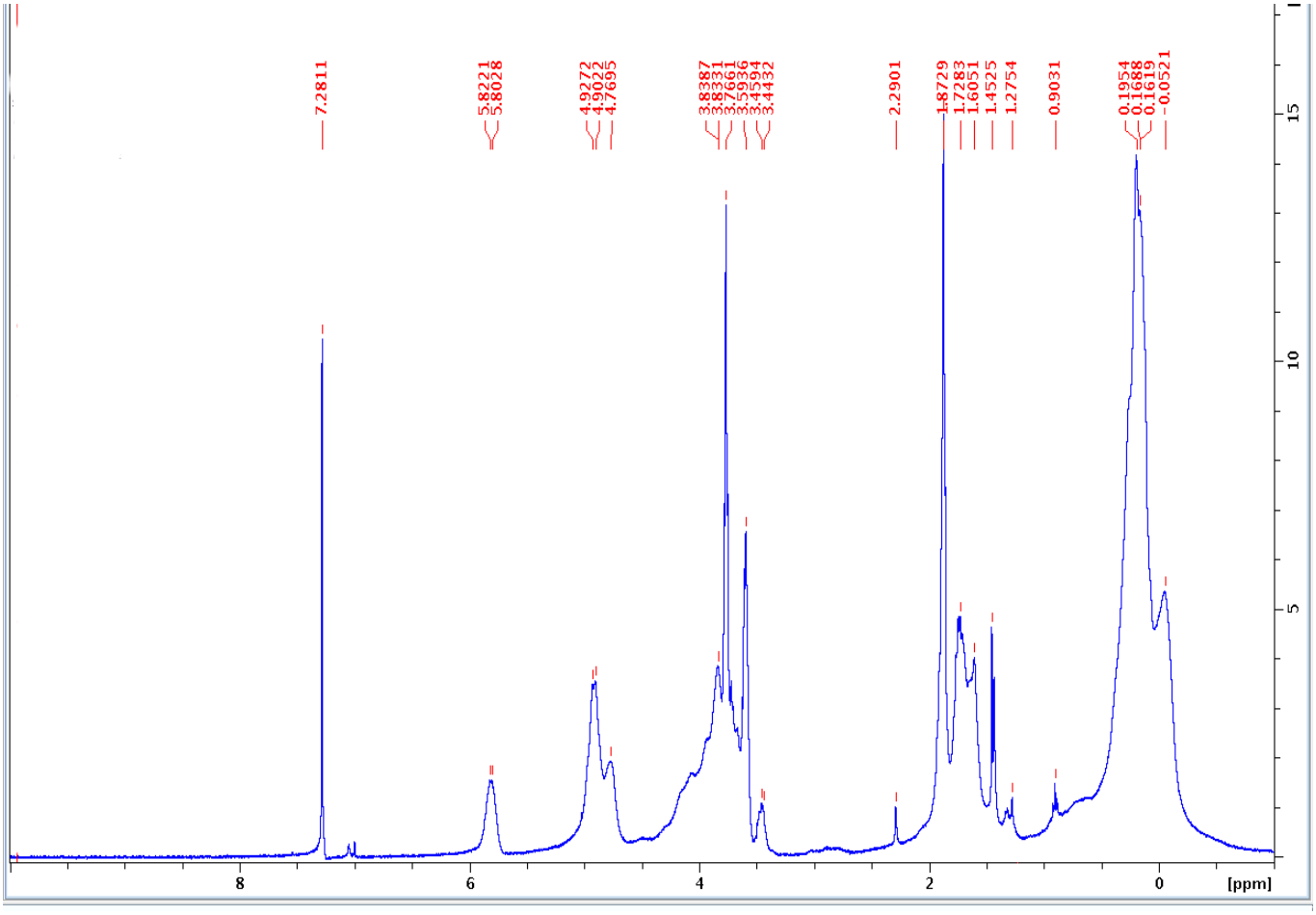

Figure 3-5. ^{1}H NMR Spectrum of PCS Polymer

Signals showed clear signs of overlapping multiplets due to slight variation in hydrogen bonding environments. Signals were generally sharp and well defined, and are summarized in *Table 3-1*.

Table 3-1. ^{1}H NMR Signals for Polycarbosilane in $CDCl_3$

^{1}H NMR Chemical Shift (ppm)
7.2811
5.8221
4.9022
4.7695
3.7661
3.5936
3.4432
2.2901
1.8729
1.7283
1.6051
1.4525
1.2754
0.9031
0.1688
0.0521

3.4.3 Thermo-Gravimetric Analysis / Mass Spectrometry

Thermo-Gravimetric Analysis was used to determine the ceramic yield resulting from the pyrolysis of the polymer and to observe mass losses corresponding to events in the ceramic-formation process. The Netzsch Proteus Software c-DTA® program was used to determine endothermic and exothermic events based on the difference in the theoretical liner temperature rate of heating and the temperature measured at the bottom of the sample crucible. Polymer samples were heated to 830°C at 10°C / minute in 50 sccm of argon. The thermogram for the polymer and c-DTA curve is shown in *Figure 3-6*.

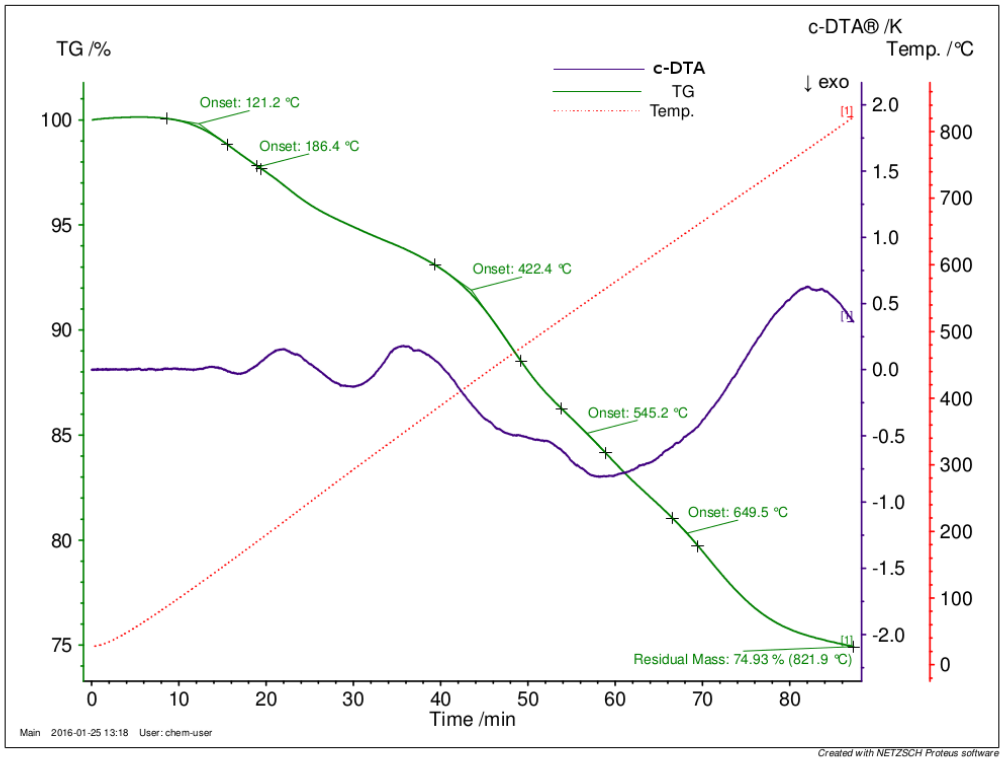

Figure 3-6. TG Curve and c-DTA® for PCS Polymer Heated to 830°C

Residual mass of the polymer (Ceramic Yield) was 74.93%, and the thermogram showed inflections at 121.2˚C, 186.4˚C, 422.4˚C, 545.2˚C, and 649.6˚C. The c-DTA® curve showed endothermoic events corresponding with the TG inflections at 186.4˚C, 422.4˚C, 649.6˚C, as well as an exothermic event at the TG inflection at 545.2˚C. Mass spectrometry was coupled with the TGA and for clarity these data were split into two separate figures, *Figures 3-7 and 3-8*, below.

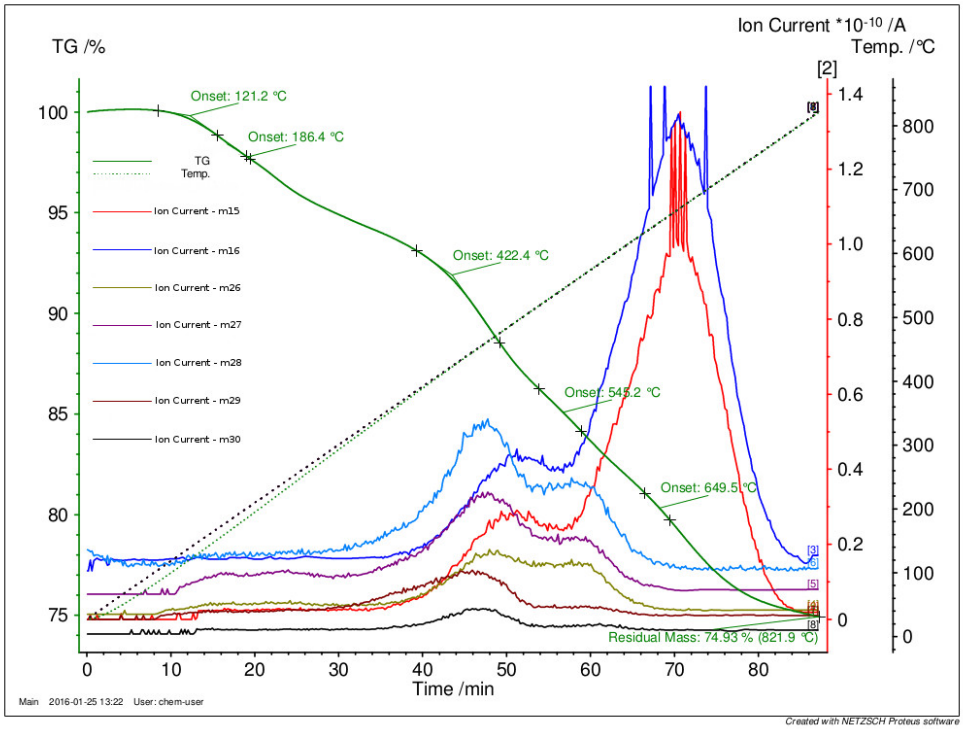

Figure 3-7. TG-MS for PCS Polymer Heated to 830°C (Select Masses)

MS peaks were present for mass/charge (m/z) = 15, 26, 26, 27, 28, and 29, with a clear correlation of masses 15 and 16, as well as for masses 26, 27, 28, and 29. These residual gas signals corresponded to mass losses on the TG curve at 422.4°C and 545.2°C to m/z = 26, 27, 28, and 29, while the signals for m/z 15 and 16 corresponded to the TG inflection at 649.5°C.

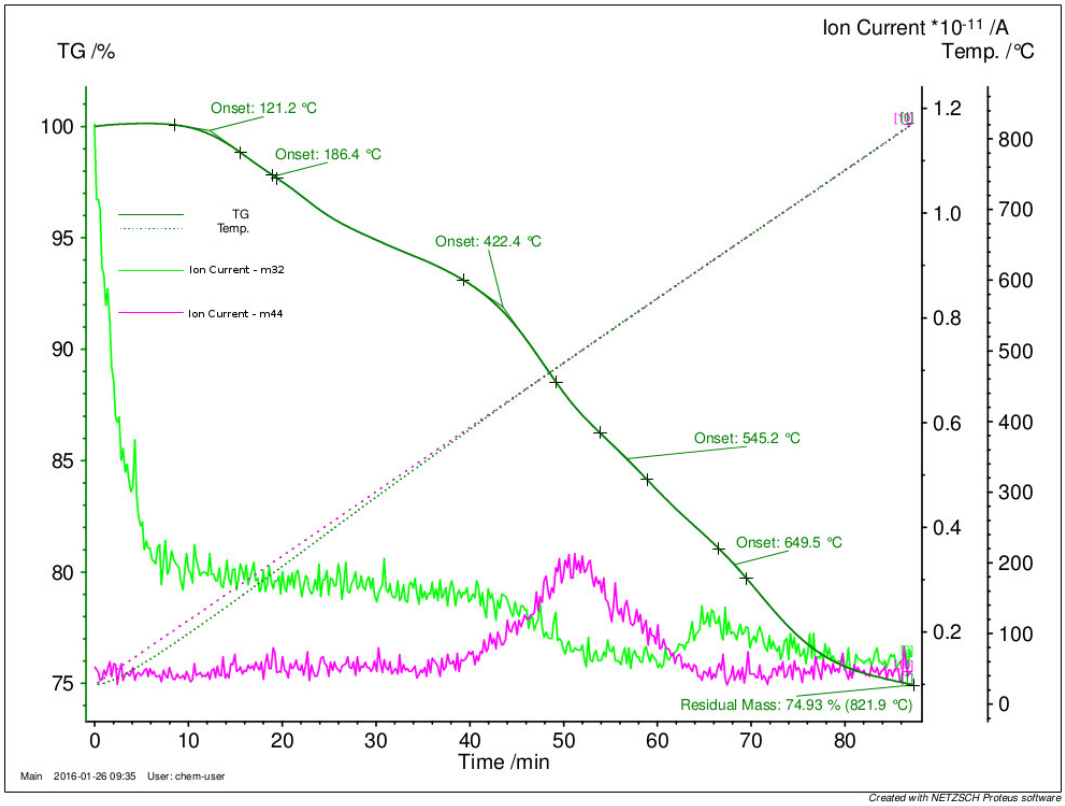

Figure 3-8. TG-MS for PCS Polymer Heated to 830°C (Masses 32 and 44)

MS signals for masses 32 and 44 were observed and were plotted separately from other masses for clarity. The increase of m44 signal directly correlated to the decrease in m32 signal and both of these trends occurred at the TG inflection at 545.2°C

3.4.4 X-Ray Diffraction

X-Ray Diffraction data was obtained for polymer samples heated to both 1100°C and 1600°C under argon. The 1100°C pattern (*Figure 3-9*) showed distinct, broadened signals at 2θ = 35.54, 59.88, and 71.74 consistent with nano to micro-crystalline character in the ceramic material. The polymer heated to 1600°C (*Figure 3-10*) showed sharpened reflections at 2θ =

34.06, 35.52, 59.98, 71.74, and 75.46 consistent with a crystalline ceramic.

Figure 3-9. XRD Pattern for PCS Polymer Pyrolyzed to 1100°C under Argon.

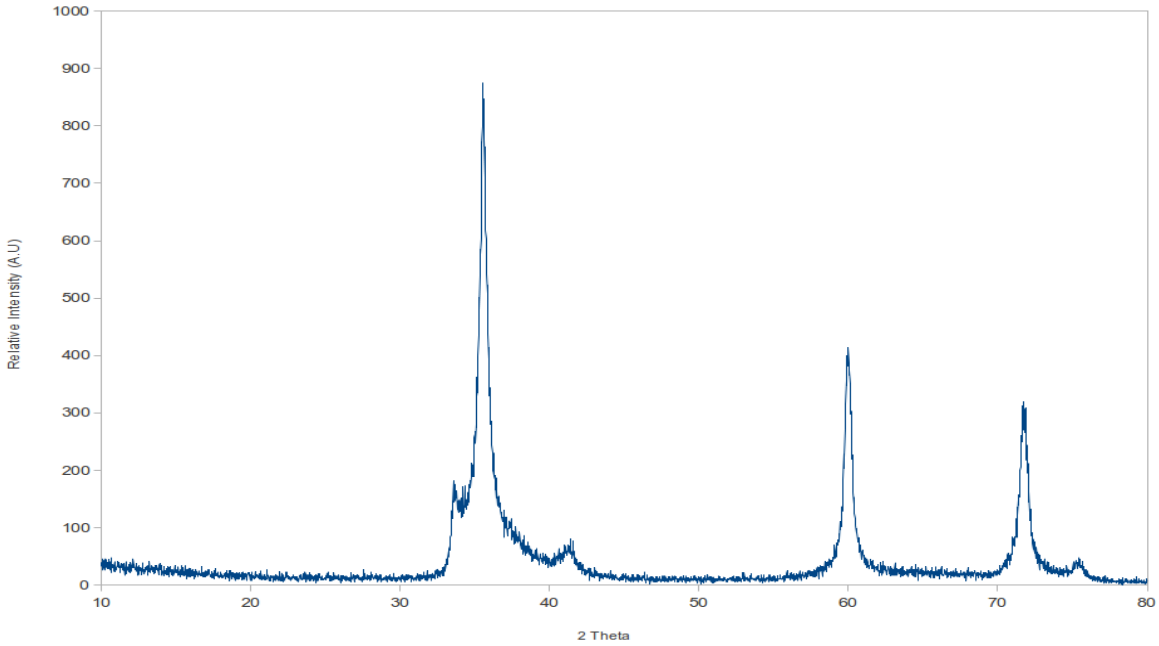

Figure 3-10. XRD Pattern for PCS Polymer Pyrolyzed to 1600°C under Argon.

Polymer samples were also heated to 900°C, 1100°C, 1400°C, 1600°C under argon and XRD patterns were obtained for each sample to compare the signals during the crystallization process. The 900°C pattern showed very subtle, broad signals for the most intense reflections, and these signals were resolved and became sharpened as the temperature was increased. The reflections observed matched those present in the pattern from *Figure 3-11*.

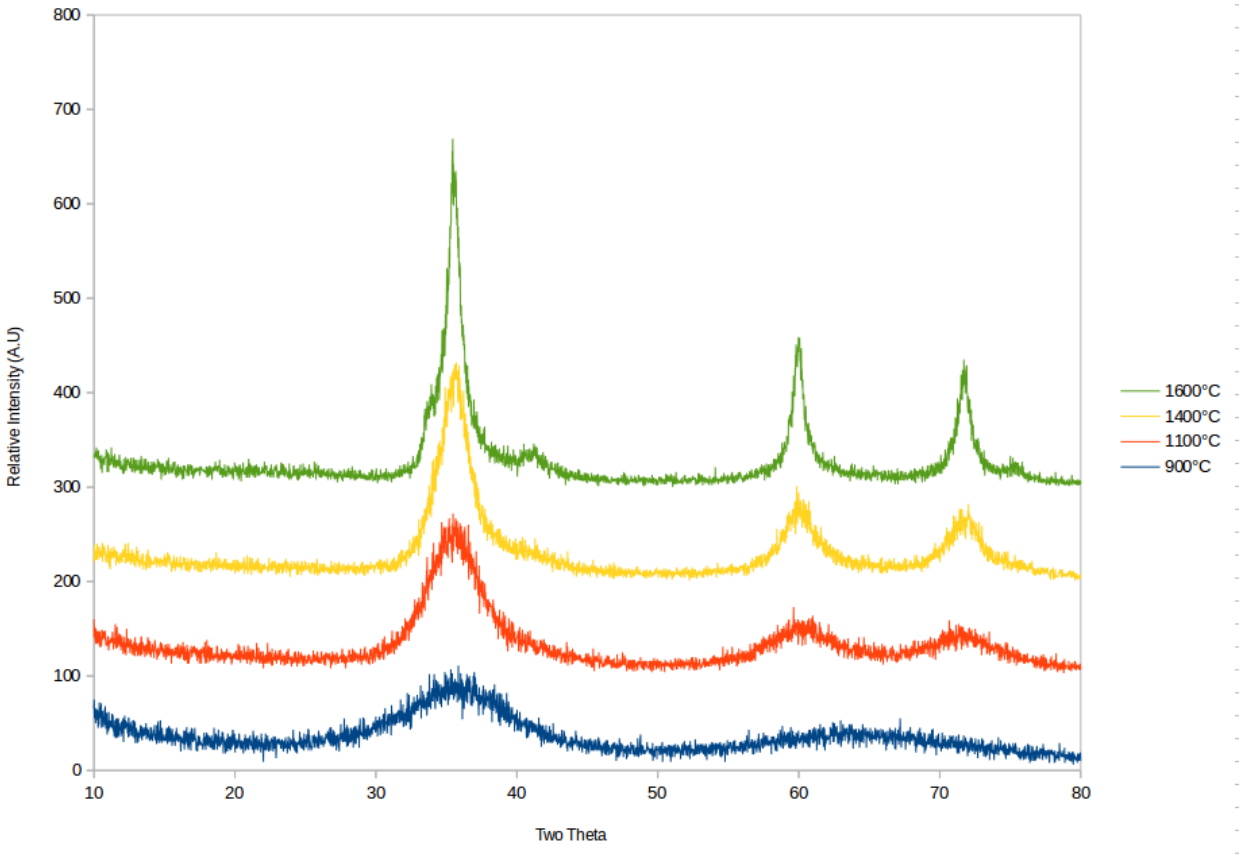

Figure 3-11. XRD Temperature Study of PCS Polymer Heated Under Argon

3.4.5 Scanning Electron Microscopy

Ceramic samples heated to both 1100˚C and 1600˚C were ground with a mortar and pestle and examined using SEM. Both polymer samples showed jagged, irregular grains of material in the 100 micron range, evident in *Figures 3-12 through 3-15*. Both samples appeared similar in grain shape and size.

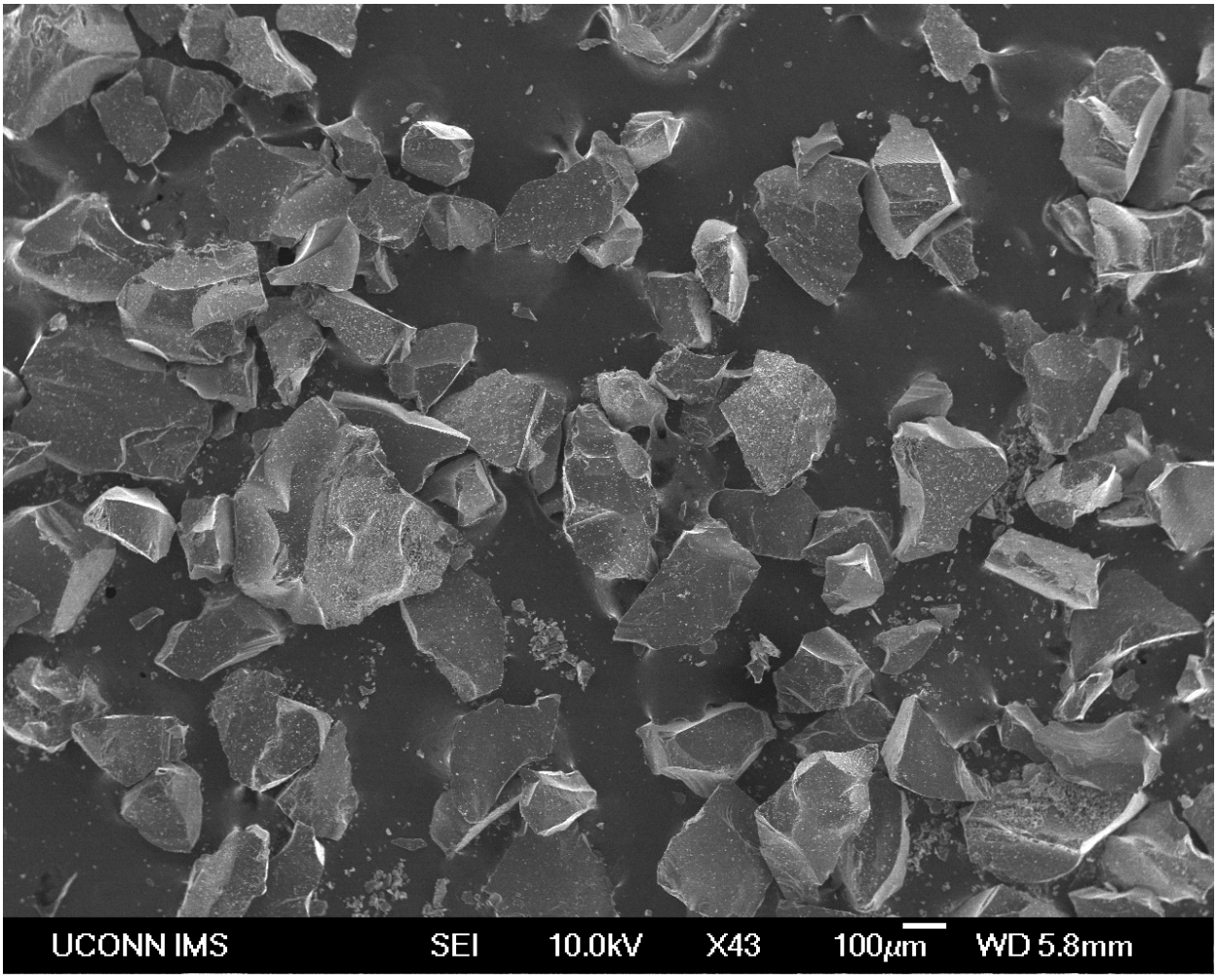

Figure 3-12. SEM Micrograph of PCS Pyrolyzed to 1100°C under Argon.

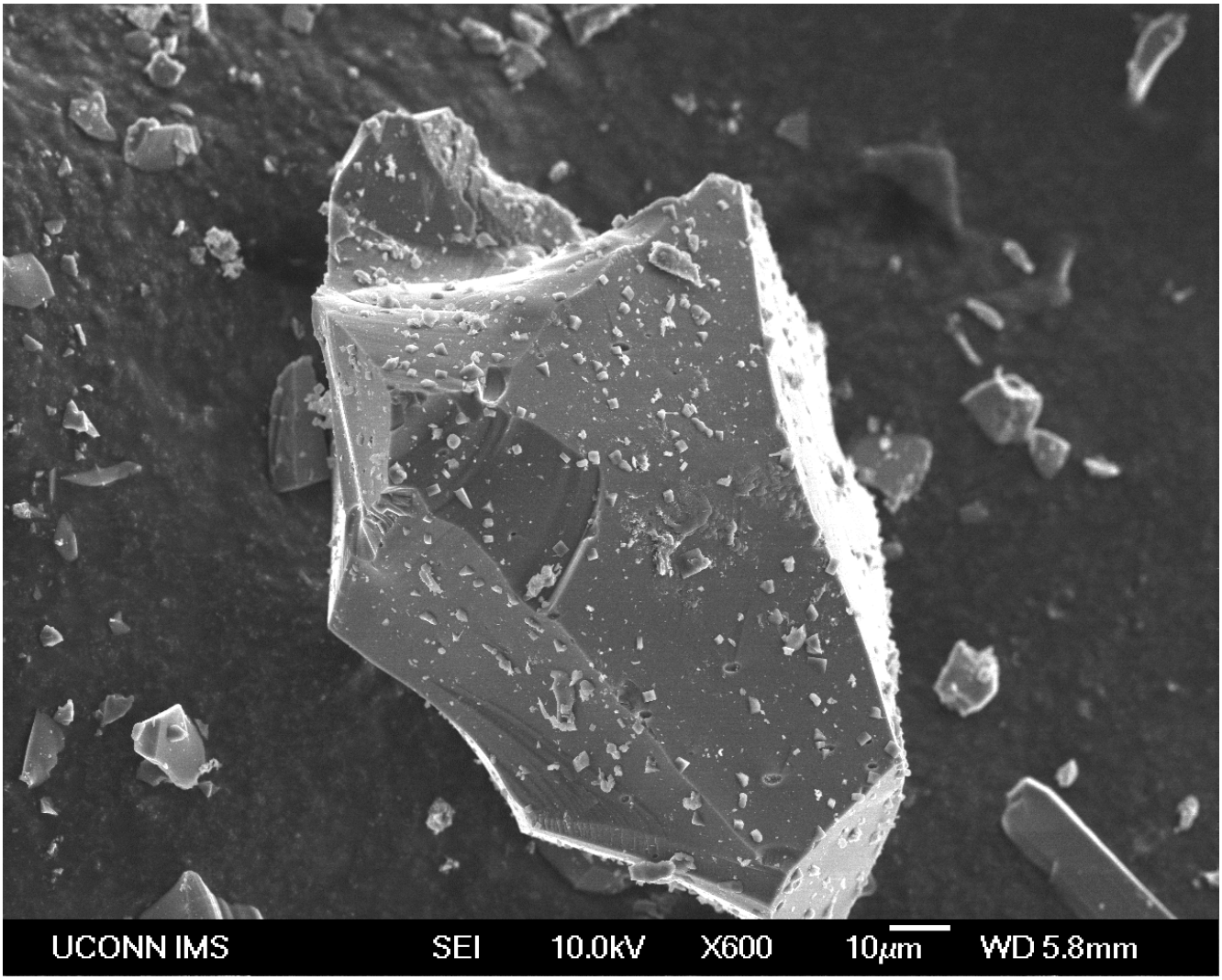

Figure 3-13. SEM Micrograph of PCS Heated to 1100°C under Argon.

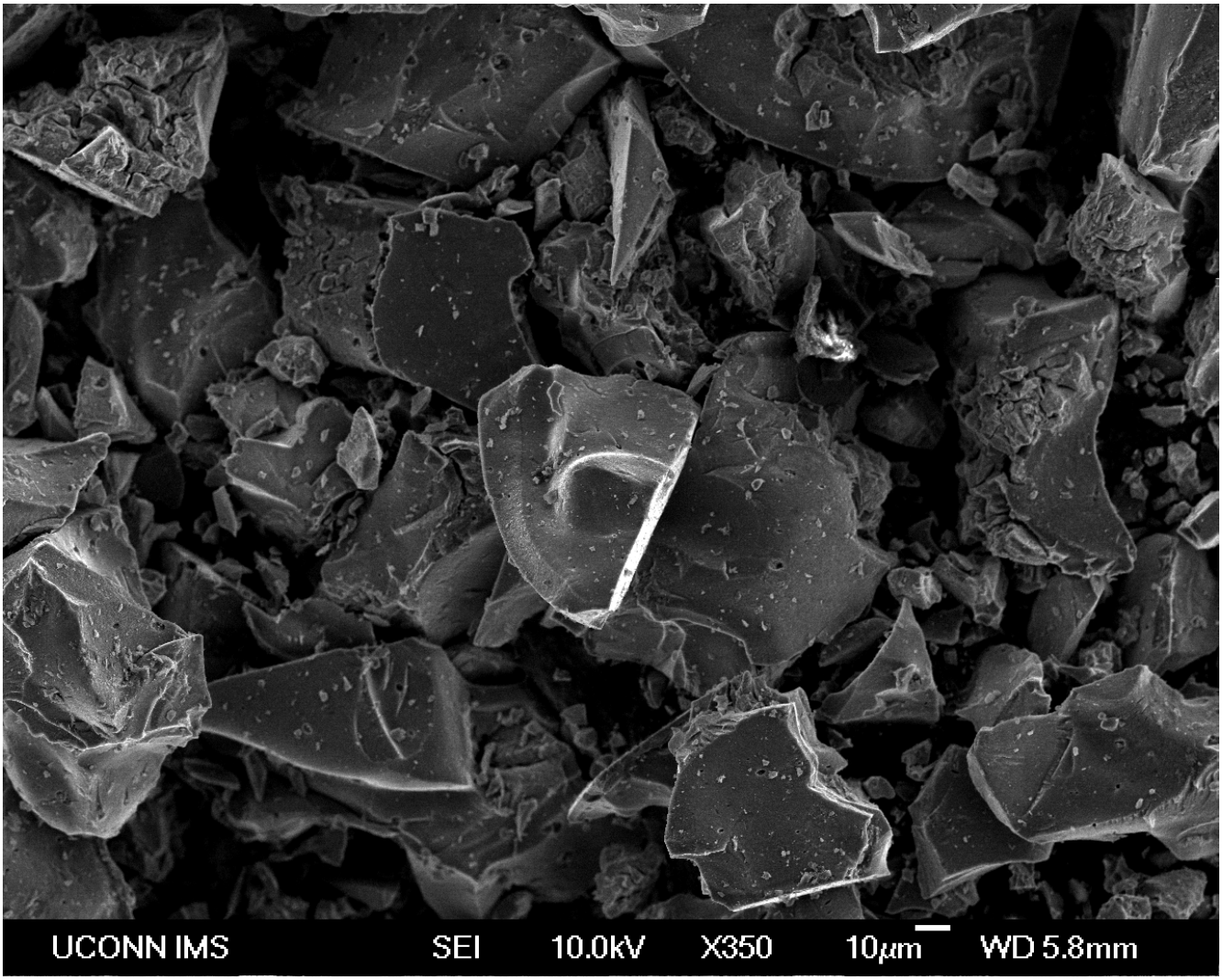

Figure 3-14. SEM Micrograph of PCS Heated to 1600°C under Argon.

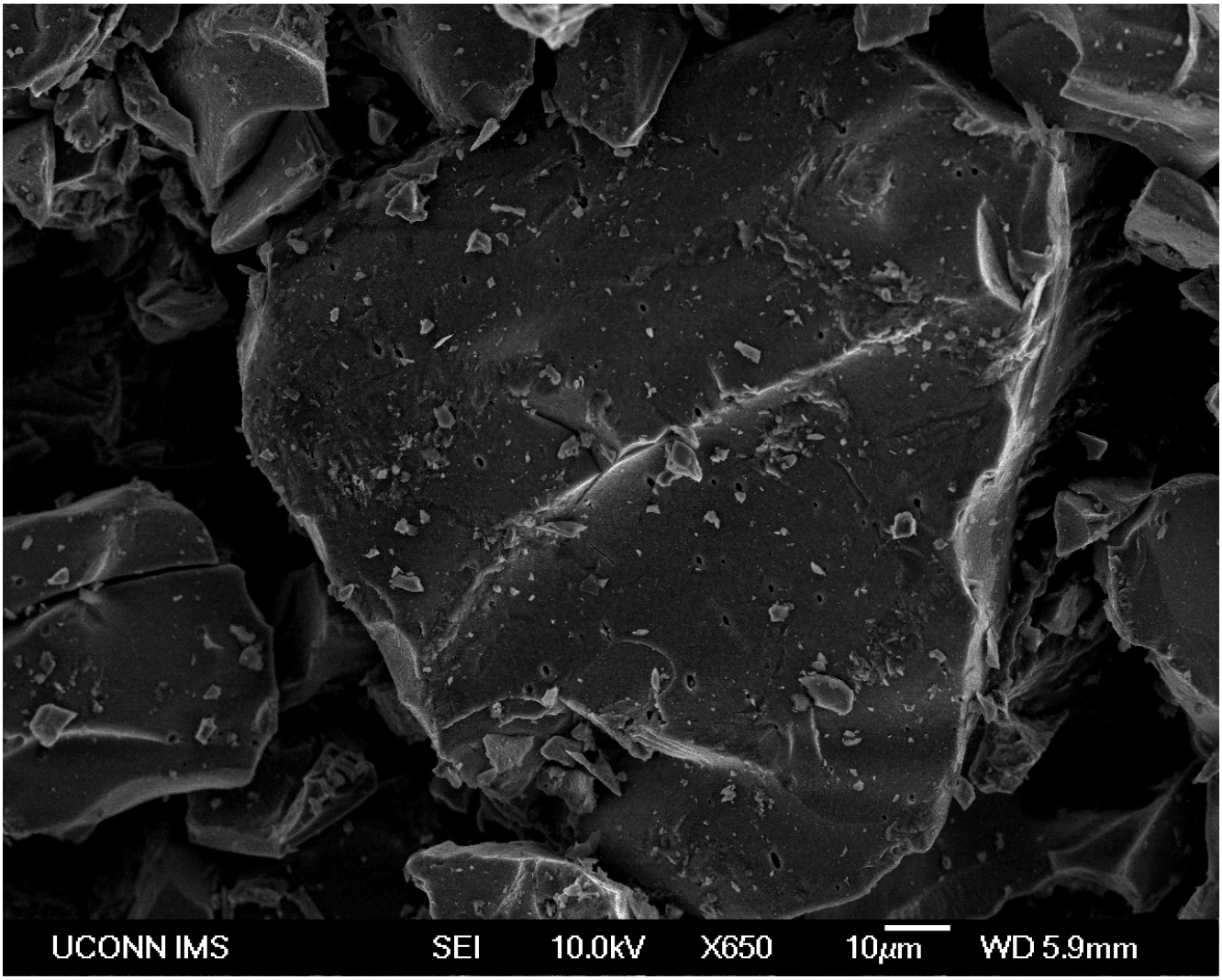

Figure 3-15. SEM Micrograph of PCS Heated to 1600°C under Argon.

3.4.6 Energy Dispersive X-Ray Spectroscopy

Samples produced for SEM were also analyzed using EDS. Polymer samples heated to both 1100˚C and 1600˚C were examined for difference in elemental composition. The plots, shown in *Figures 3-16 and 3-17*, indicated signals for silicon, carbon, and oxygen. The weight percent and atomic percent values are noted in *Table 3-2*.

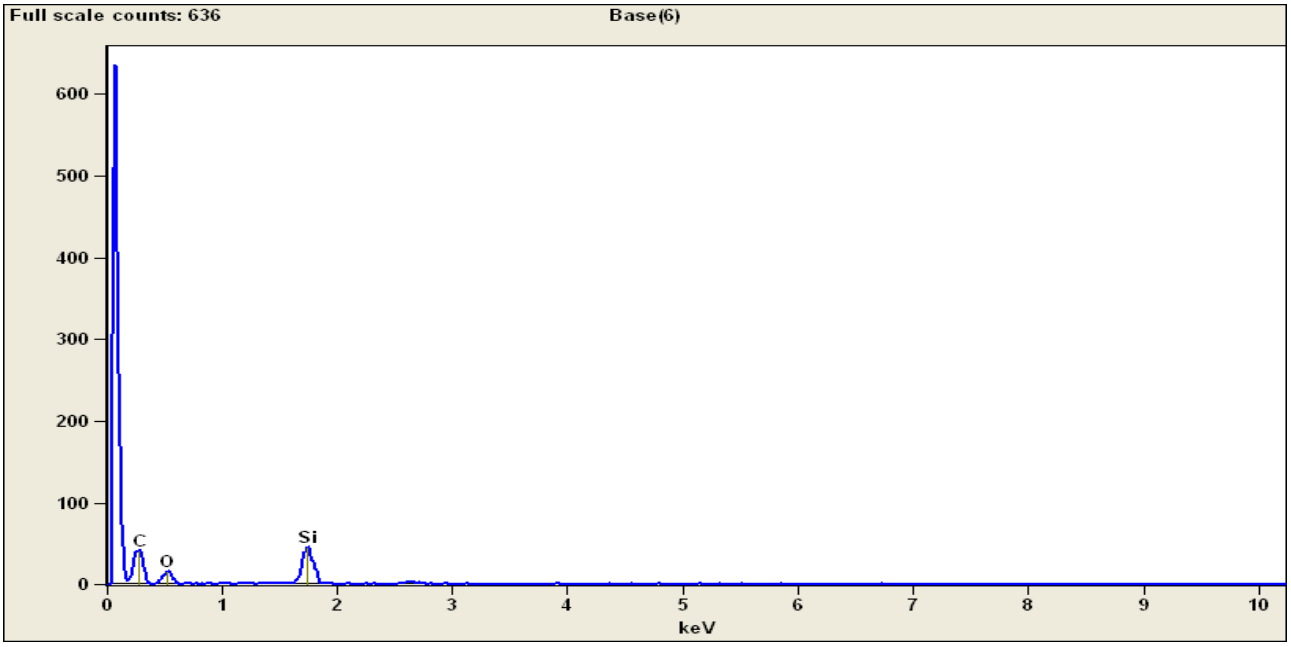

Figure 3-16. EDS Spectrum of PCS Heated to 1100°C under Argon.

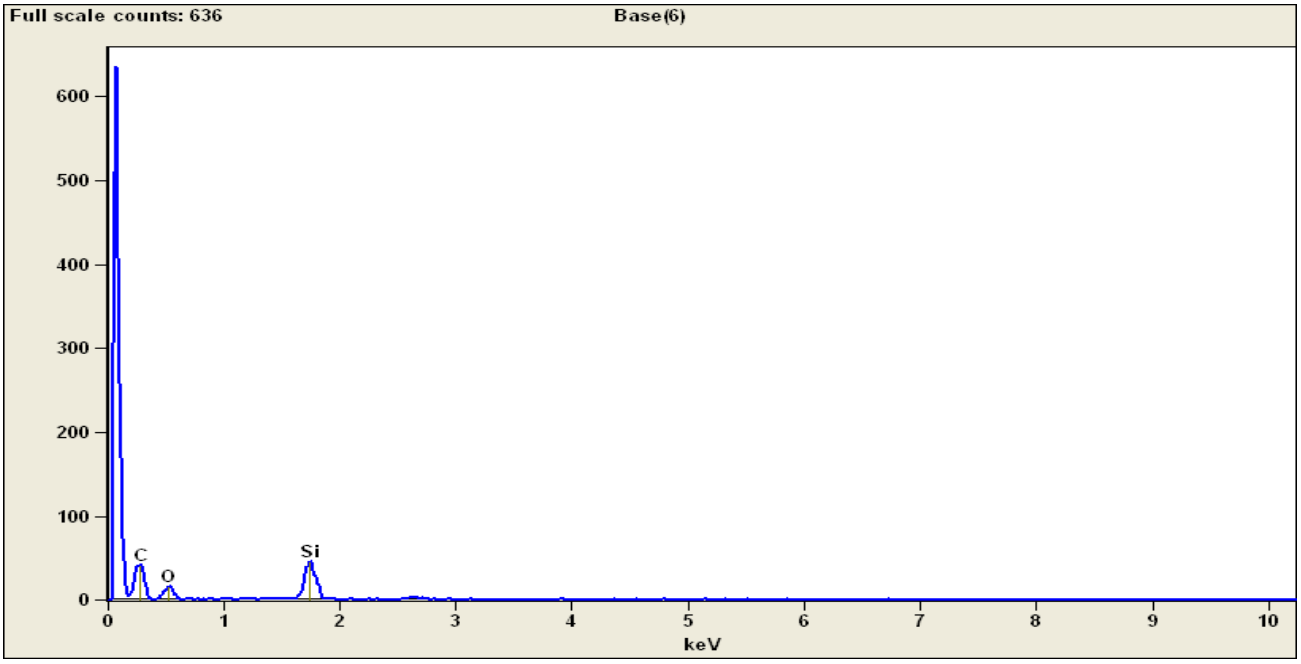

Figure 3-17. EDS Spectrum of PCS Heated to 1600°C under Argon.

Table 3-2. Atomic and Weight Percents for PCS Heated to 1100°C and 1600°C under Argon

	1100˚C PCS Weight %	1100˚C PCS Atomic %	1600˚C PCS Weight %	1600˚C PCS Atomic %
Carbon	31.9	50.9	28.7	47.5
Silicon	62.9	42.9	67.5	47.8
Oxygen	5.2	6.2	3.8	4.7

3.5 Discussion

3.5.1 Synthesis and Ceramic Formation

The method for synthesis of this polymer followed a similar synthesis as performed in Huang et. al.[96], using these chlorinated silane precursors and allyl chloride were used to promote branching in the assembled polymer. A simplified mechanism was proposed and is shown in *Figure 3-18* below.

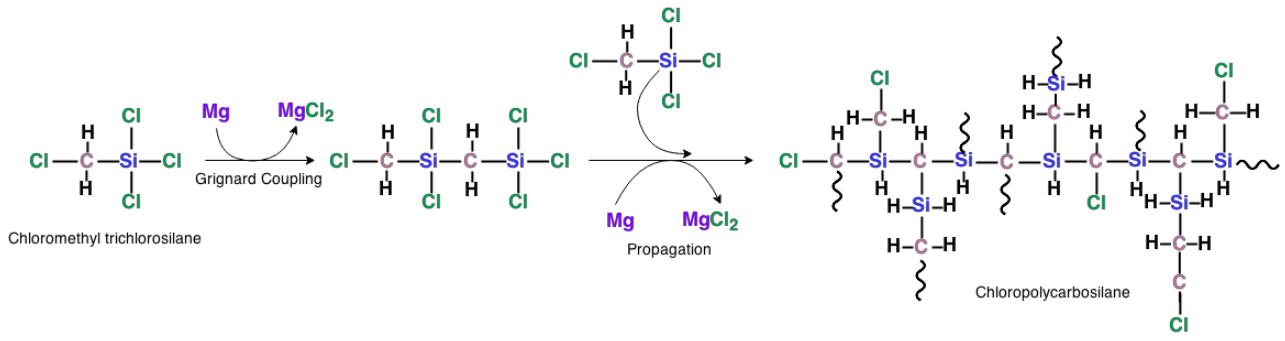

Figure 3-18. Grignard Reaction of Chlorinated Silanes and Magnesium Forming Polycarbosilane

In this simplified mechanism[97], the chlorinated silanes reacted with magnesium metal, inserting magnesium between either a silicon-bound or a carbon-bound chlorine. The formation of this in-situ Grignard reagent allowed for the formation of silicon-carbon bonds, forming the backbone of the polymer. This reaction propagated with the continued magnesium insertion into the chlorinated end groups of the silanes. Excess amounts of magnesium chloride were produced and settled to the bottom of the flask, as it was insoluble in both THF and diethyl

ether. Continued propagation of this Grignard reaction resulted in the formation of a branched polymer containing silicon and carbon in the backbone. This degree of branching was desirable to produce a higher ceramic yield when the side chains of carbon and silicon were burned away during pyrolysis, so allyl chloride was added to the original polymer design to increase this degree of branching, as well as to modify the stoichiometry of the polymer and thus the stoichiometry of the resulting ceramic. Incorporation of the allyl chloride produced stability in the polymer, as well as increased viscosity with the high degree of branching. The allyl group was incorporated into the polymer through a similar Grignard Mechanism, in which the allyl chloride reacted with magensium metal, forming the in-situ Grignard reagent allyl magnesium chloride. This Grignard reagent reacted with the chloropolycarbosilane end groups, coupling and producing excess insoluble magnesium chloride and an allyl polycarbosilane end segment in the polymer. This part of the polymer formation mechanism is shown in *Figure 3-19*.

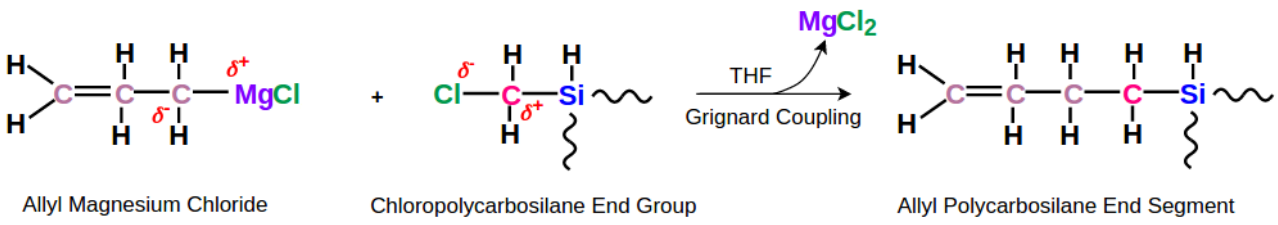

Figure 3-19. Allyl Magnesium Chloride Grignard Reaction with Polycarbosilane End Segments

Lithium aluminum hydride was then used to reduce the chlorines on the polymer and replace them with hydrogen. This dehalogenation step is shown in *Figure 3-20*.

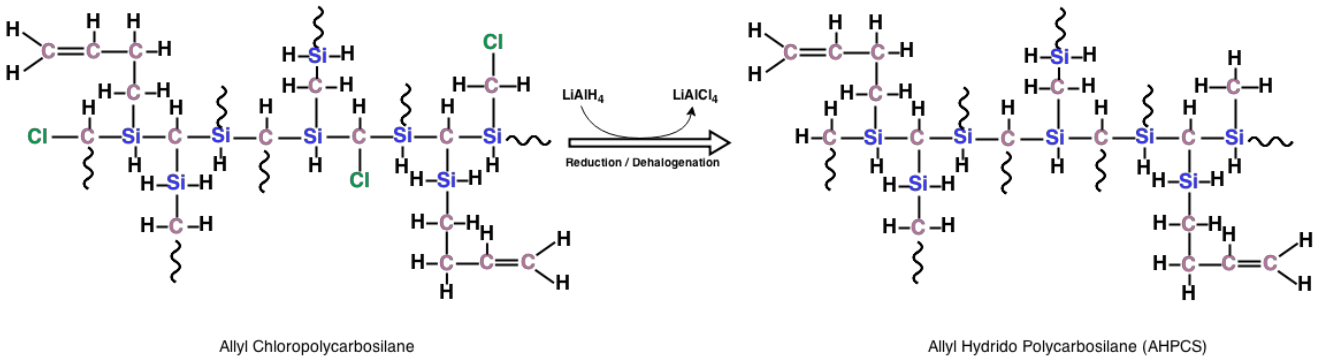

Figure 3-20. Reduction/Dehalogenation Mechanism of PCS

After the formation of the polymer, the material was heated under inert atmosphere to produce the silicon carbide ceramic. The low temperature cure produced a green body, and amorphous silicon carbide at temperatures below 1000˚C. Further pyrolysis to higher temperatures produced crystalline silicon carbide, depicted in *Figure 3-21*.

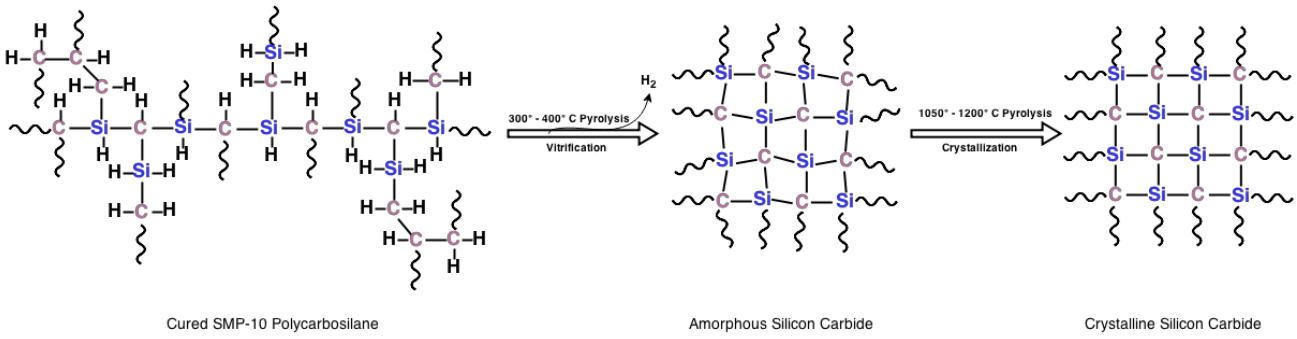

Figure 3-21. Vitrification and Crystallization Mechanism of Silicon Carbide Produced from PCS

A mechanism for cross-linking and ceramic formation was proposed based on the characterization and knowledge of the polymeric system. Polymer samples demonstrated air-sensitivity over time, as well as evolution of flammable hydrogen gas at room temperature. The hydrogen gas evolution occurred through a free-radical coupling process and produced polymer crosslinking through neighboring silicon atoms, shown in *Figure 3-22*. This process was characterized through the evolution of hydrogen over time in the polymer, as well as the visible cross linking of liquid polymer during cure process[97].

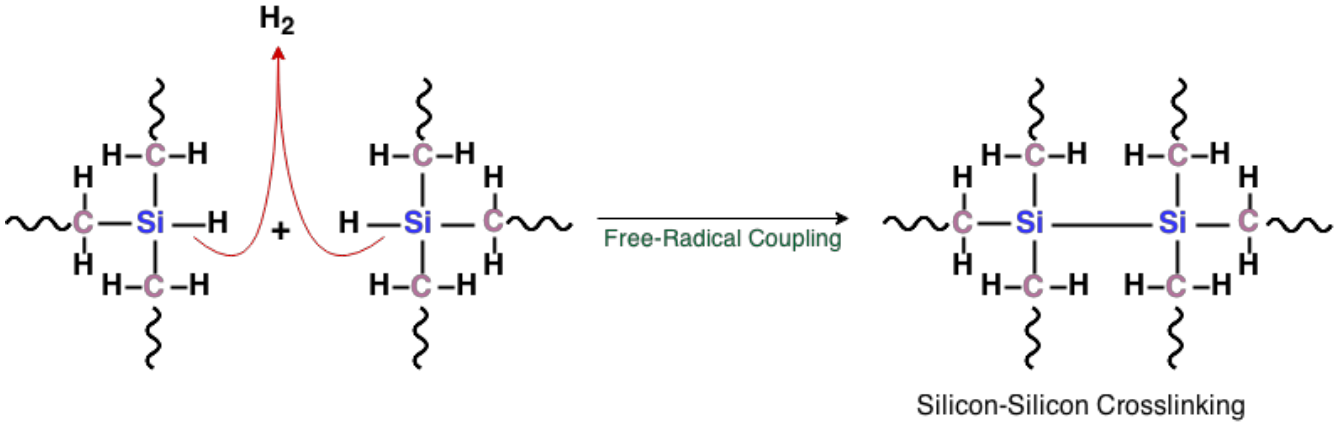

Figure 3-22. Hydrogen Evolution through Free-Radical Coupling in PCS

The polymer was also shown to be moisture sensitive, crosslinking slowly with addition to water and crosslinking over extended time with exposure to air. This process was explained though the hydration of the polymer with release of hydrogen gas, shown in *Figure 3-23*, followed by a condensation coupling reaction supported by the loss of water from the polymer evident in TG-MS studies. After this water loss, the polymer crosslinked through the incorporation of oxygen bridging the silicon bonds, forming a siloxane group during the cure process.

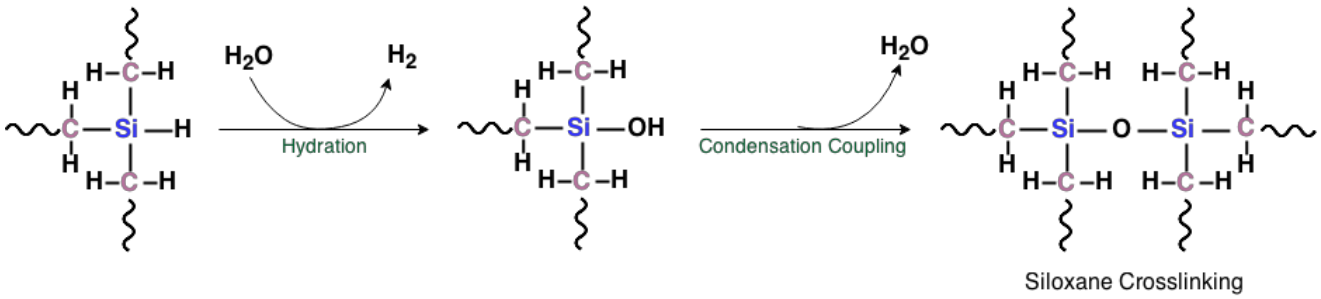

Figure 3-23. Condensation Coupling and Siloxane Crosslinking of PCS

A third proposed mechanism of crosslinking in the polymer was proposed to be oxidative coupling. This process resulted in the evolution of water, present in the TG-MS data, as well as visible cross linking of liquid polymer during cure process and extended exposure to air. During this process, shown in *Figure 3-24*, oxygen was absorbed into the polymer, reacting with terminal hydrogen groups and resulting in formation of a siloxane during the crosslinking

process. This absorption of oxygen was also evident in the TG-MS data, further supporting the possibility for this type of curing reaction.

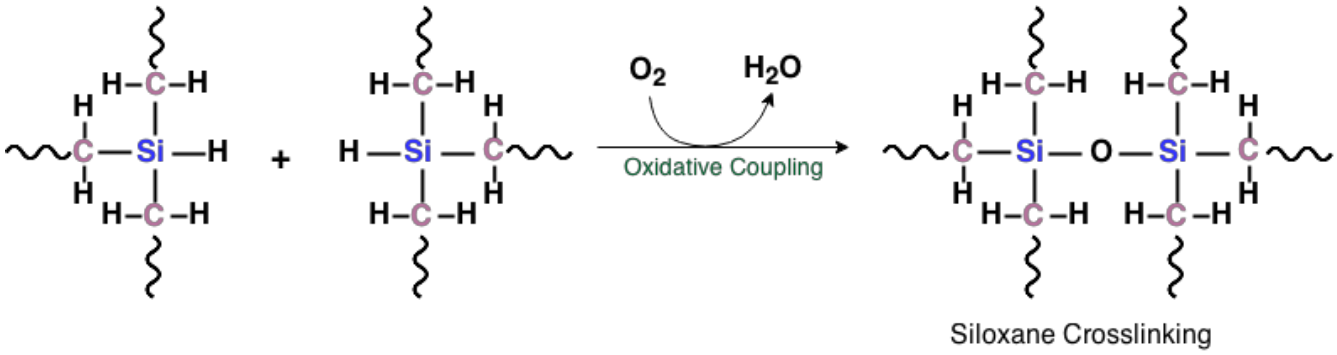

Figure 3-24. Oxidative Coupling and Siloxane Crosslinking of PCS

3.5.2 Attenuated Total Reflectance Spectroscopy

ATR was used to analyze the structure of the polymer and to determine both functional groups present and bonding environments of the unheated polymer. *Figure 3-3* showed frequencies of the liquid polymer, which are summarized in *Table 3-3*.

Table 3-3. ATR Frequencies and Corresponding Structural Groups in PCS Polymer

Frequency (cm^{-1})	Structural Group
2958.71	C-H Stretch
2145.18	Si-H Stretch
1356.21	Si-CH_2
1254.37	Si-CH_3
1045.05	Si-Allyl
934.19	C-O-C (Solvent)
860.71	=C-H
771.36	Mono-substituted alkene

These data suggest a structure in which silicon is bound to carbon in an alternating backbone with terminal Si-H_3 groups. Silicon-allyl bonds are also present, due to the allyl chloride precursor. The data also suggests few carbon-carbon bonds in the polymer, including

both the backbone and as side chains. The polymer contained residual solvent from synthesis, observed with the sharp signal at 934.19 cm^{-1}. This claim is further supported with ^{1}H NMR data.

The temperature study was performed to determine the loss of functional groups as the polymer was heated and converted to silicon carbide. Polymer samples were heated to 300˚C, 500˚C, 700˚C, 900˚C, and 1100˚C before being cooled and analyzed. ATR signals are summarized and indexed in *Table 3-4*.

Table 3-4. Indexed ATR Signals for Polycarbosilane During Heat Treatment

Wavenumber (cm^{-1})	Bond Type (Functional Group)	Temperature at which Signal is Observed (˚C)
2960	C-H Stretch	300
2145	Si-H Stretch	300, 500
1355	$Si\text{-}CH_2$	300
1255	$Si\text{-}CH_3$	300
1045	$SiCH_2Si$	300, 500, 700
935	CH_3	300, 500, 700
880	C-H	300, 500
~750 - 800	SiC	700, 900, 1100
720	Mono-substituted alkene	300, 500

As the polymer was heated, signals present in the polymer from carbon to hydrogen and silicon to hydrogen disappear when the polymer is heated past 500˚C. Signals assigned to $SiCH_2Si$, as well as alkane and alkene signals are no longer present past 700˚C, and by 900˚C, a broad signal in the 800 cm^{-1} range appears with the formation of silicon carbide.

3.5.3 ^{1}H Nuclear Magnetic Resonance

^{1}H NMR was used to characterize the bonding environments of the polymer. The signals in the spectrum (*Figure 3-5.*) are summarized in *Table 3-1. Figure 3-25* labels the referenced allyl hydrogens. These data suggest several unique silicon to C-H bonding environments, as

supported in the ATR data. The polymer backbone is composed of alternating silicon and carbon and there are terminal Si-H groups. Branching occurs from silicon to carbon, and allyl groups are preserved in these branches. A proposed structure is shown in *Figure 3-27*.

^{1}H NMR revealed signals consistent with a polymer containing silicon to carbon amd hydrogen bonds, as well as pronounced signals from the protons in THF at 3.7661 ppm and 1.8729 ppm[98]. Two signals were attributed to residual THF from the polymer synthesis process, and are identified as THF $H^{(A)}$ and THF $H^{(B)}$ in *Figure 3-25*.

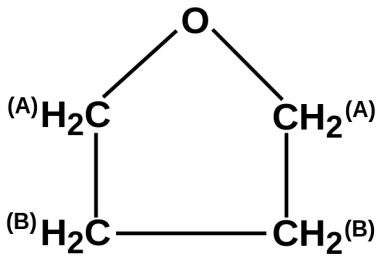

Figure 3-25. THF with Labelled Hydrogen for ^{1}H NMR

Several signals were attributed to the allyl groups in the polymer, which is labeled for clarity in *Figure 3-26* below.

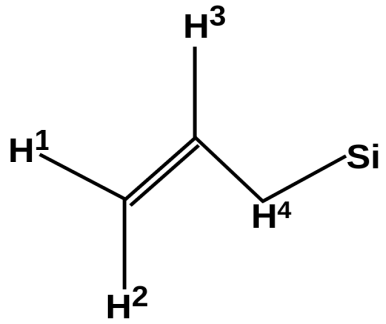

Figure 3-26. Allyl Group with Labelled Hydrogen for ^{1}H NMR

The peaks shown in *Figure 3-5* are summarized in *Table 3-5*.

Table 3-5. ^{1}H NMR Peak Shifts and Corresponding Structural Groups in PCS Polymer

Peak Shift (ppm)	Structural Group
7.2811	$CDCl_3$
5.8221	Allyl H^3
4.9272	Allyl H^2
4.7695	Allyl H^1
3.8387	THF
1.8729	THF
1.7283	Si-CH_2
1.6051	Si-CH_2
1.4525	Allyl H^4
1.2754	Si-CH_2
0.1954	Si-CH_x
0.0521	Si-CH_x

As expected, the polymer contained significant different bonding environments for silicon, bound to carbon and hydrogen. As expected, the allyl groups were preserved during the synthesis process, present in the signals for the H^1-H^4 in the allyl functional group. This lead to increased branching in the polymer when a terminal allyl group occurred, and the occurrence of multiplets and significant signal splitting for Si-CH_2 and Si-CH_x signals. A simplified polymer structure was proposed from this data and appears in *Figure 3-27*. The backbone was composed of alternating silcon and carbon atoms with terminal, reactive SiH_3 groups where no branching occurred. Allyl groups were bound to the atoms where no hydrogens were present, as no signals for this type of bonding environment was observed in the NMR spectrum. Allyl groups remained terminal, and the polymer was proposed to branch at silicon, though branching at carbon was also possible. The most important parts of the proposed structure were the silicon-carbon alternating backbone, and the isolated allyl groups.

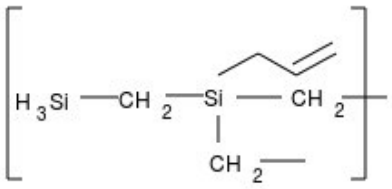

Figure 3-27. Proposed Structure of PCS Polymer

3.5.4 Thermo-Gravimetric Analysis / Mass Spectrometry

The Ceramic Yield of the polymer was determined to be 75%. Ceramic yield is the mass of a resulting ceramic expressed as a percentage of the initial mass of a ceramic precursor, in this case the PCS pre-ceramic polymer. This mass is relatively high as compared to commercially available pre-ceramic polymers like Starfire® SMP-10, a similar ceramic precursor. The TGA plot for Starfire® SMP-10 is shown in **Section 4.4.1**, and a ceramic yield of 70% when treated with the same conditions.

Mass signals were identified based on knowledge of the structure of the polymer and commonly indexed mass spectrometry signals. These data are summarized in *Table 3-6*.

Table 3-6. TG-MS Values and Corresponding Evolved Gas Analysis

M/z Value	Fragment Identification
15	CH_3
16	Methane (CH_4)
26	Ethane / Allyl Fragment ($C - CH_2$)
27	Ethane / Allyl Fragment ($C - CH_3$)
28	Ethane / Allyl Fragment ($CH - CH_3$)
29	Ethane / Allyl Fragment ($H_3C - CH_2$)
30	Ethane ($H_3C - CH_3$)
32	O_2
44	CO_2

Inflections on the TG curve corresponded to the loss of moisture, solvent, low weight organic groups at the inflections at 121.2˚C and 186.4˚C, also correlating to the first endothermic event observed in the c-DTA curve. The next onset, at 422.4˚C, was attributed to the loss of either ethane or allyl group fragments, composed of two carbons and two hydrogens (m/z=26), three hydrogens (m/z=27), four hydrogens (m/z=28, or five hydrogens (m/z=29). A signal was also observed for m/z = 30 (ethane, C_2H_6), which was associated to the mass loss and endothermic event at 422.4˚C . The next mass loss at 545.2˚C also corresponded to both these ethane or allyl fragments and appears as second, smaller signal in the MS plot for m/z = 26- through m/z= 30, as well as the initial evolution of methane from the polymer-forming ceramic, as m/z =15 and m/z=16. The two large signals that correlated to the final mass loss at 649.5˚C were also attributed to methane release during the crystallization process. This methane evolution and mass loss was in agreement with the exothermic event observed in the c-DTA® curve.

The mass spec plots for m/z=32 and m/z=44 were arranged separately from the others for clarity, as well as to identify the oxidation behavior in this material. A decrease in the oxygen signal was observed in the 550˚C range and coincided with an increase in evolution of carbon

dioxide (m/z=44). This data indicated that the oxygen reacted with the carbon in the polymer, forming and releasing carbon dioxide in this temperature range.

3.5.5 X-Ray Diffraction

X-Ray Diffraction (*Figures 3-9 and 3-10.*) showed a microcrystalline phase of silicon carbide upon pyrolysis at 1100˚C under argon and crystalline SiC upon pyrolysis to 1600˚C. *Table 3-7.* summarizes the reflection values and planes corresponding to ASTM Card No. 29-1129 [β-SiC] *Table 3-8.* summarizes reflection values and correcponding ASTM Card values for the α-SiC ceramic heated to 1600˚C.

Table 3-7. JCPDS vs. Experimental Reflections for Polycarbosilane Ceramic Material (1100°C)

h k l	SiC 2θ	SiC I/I_0	Experimental 2θ	Experimental I/I_0
1 1 1	35.59	100	35.54	100
2 2 0	59.98	35	59.88	41
3 1 1	71.78	25	71.74	30

Table 3-8. JCPDS vs. Experimental Reflections for Polycarbosilane Ceramic Material (1600°C)

h k l	SiC 2θ	SiC I/I_0	Experimental 2θ	Experimental I/I_0
0 1 2	34.06	70	34.20	34
1 1 21	35.45	100	35.52	100
1 0 28	60.02	80	59.98	82
1 1 27	71.97	70	71.74	64
1 1 24	75.44	30	75.46	10

The increase in sharpness of the reflections upon heating from 1100˚C and 1600˚C indicated that the crystallization process was not complete until the higher temperatures for pyrolysis. The polymer sample heated to 1100˚C exhibited broadened, unresolved signals, indicating nano to microcrystalline β-SiC ceramic characteristic. As the sample was heated to 1600˚C, the signals were sharped, resolved, and the formation of α-SiC was evident. The experimental 2θ and I/I_0 values were in excellent agreement with the JCPDS cards for both

the 1100˚C and 1600˚C samples.

3.5.6 Scanning Electron Microscopy

SEM images showed a similarity in bulk structure between the pyrolysis product at 1100˚C under argon and at 1600˚C under argon. Both samples showed rough, irregular grains in the 100 micron range. The variation in these grain sizes was likely due to the sample preparation and manual grinding of the powders. The ceramic heated to 1600˚C appears to have slightly more rounded, less sharp edges due to the increased heat and potential for initial sintering process of the ceramic grains.

3.5.7 Energy Dispersive X-Ray Spectroscopy

EDS was used to determine the elemental composition of the ceramic materials. Both samples showed evidence of silicon, carbon, and oxygen contamination as expected for this type of polymer. EDS values in *Table 3-2* proved a higher concentration of carbon than silicon in the 1100˚C sample, likely due to the residual allyl or carbonaceous species present in the sample. This excess carbon could also be attributed to the carbon tape used in the sample mounting process. The EDS method inherently has a high degree of error in these types of applications[99,100] and quantitative comparisons between samples have limited use. The sample heated to 1600˚C showed a silicon and carbon to have very close weight percents, as expected in a near-stoichiometric silicon carbide ceramic. Both samples showed oxygen contamination, though the values were relatively low (below six weight percent) and were as expected.

3.6 Conclusions

This work detailed the development of new, advanced pre-ceramic polymers with modifications to maximize properties like ceramic yield and ease of synthesis, as well as

minimize air sensitivity and stability results in progress in use of these materials in CMC applications.

The polymer produced used a relatively simple synthesis to produce a polycarbosilane with excellent ceramic yield and air stability. Precursors and experimental procedure were modified to react the moisture sensitive end groups of the polymer during the workup process, resulting in a polymer with excellent stability that still produced silicon carbide at temperatures as low as 1100˚C. Both polymer and ceramic were characterized at various temperatures and mechanisms of both polymer and ceramic formation were proposed based on data obtained. The polymer showed excellent properties for further use in CMCs and in aircraft applications.

Chapter 4 Heteroatom Incorporation of Titanium and Boron in A Commercially Available Pre-Ceramic Polymer

4.1 Introduction

Ceramic matrix composites have become a popular technology for high performance and high temperature applications including, but not limited to, aircraft and aerospace engines, body panels, and brake components for a variety of vehicles. As these high performance vehicles are developed, the need for a composite material with increasingly high strength, high thermal conductivity, low density and refractory properties continue to rise. Due to its inherent thermal resistance and strength properties, silicon carbide has historically been a material component for non-oxide ceramic matrix composite systems. Silicon carbide has excellent oxidation resistance, a relatively low coefficient of thermal expansion, and low density, making it an excellent candidate material for these types of applications[101].

With this in mind, improving the thermal and strength properties of the composite to surpass those of silicon carbide was a major consideration in the design of this polymer. Titanium diboride has been used in commercially available materials as a means to produce a high end fiber for use in CMC applications. The addition of titanium diboride into the silicon carbide provided the fiber with increased strength, oxidation resistance, and strength as compared to silicon carbide only fibers[102].

During the design of the polymer system, application was the main motivation during the development process. Application for the material was for dual usage in ceramic matrix composites as both fiber precursor and as a matrix material. These CMCs were designed for use in the aviation and aerospace industries for high temperature applications. The polymer

would be spun into fibers and pyrolyzed for a reinforcing material, where amorphous or nano-crystalline silicon carbide would yield increase flexibility, as well as excellent thermal properties and oxidation resistance. The polymer would also be used as a bulk matrix material in the composite, serving as the strength component and allowing for toughening mechanisms when the matrix cracks during use. The material could also be used as a materials precursor in semiconductors, chemical sensors, or biological applications, taking advantage of the electrically and thermally conductive properties of titanium diboride[103]. These applications include transformers, cathodes, sensors, and other electrical components[104, 105, 106]. The main focus of this work was to use the titanium diboride and silicon cabride based polymer for use in CMCs.

The ceramic produced from this modified polymer can be used in multiple CMC components, including the fiber and matrix of the composite, typically derived from pre-ceramic polymers. The usage of polymers allows for excellent control of the shape and form in both continuous fiber fabrication, as well as in matrix application and production for complex 3-D shaped forms. The crystallinity of the resulting ceramic in these applications is important for the strength properties. Fibers are typically amorphous to nano-crystalline to preserve strength and flexibility properties during the CMC fabrication process, while matrix materials can be micro-crystalline, as well as amorphous. With the increasing need for stronger and more temperature-resistant materials, one main shortcoming of silicon carbide has become evident in these types of applications. During the heating process and exposure to temperatures over 1600°C, silicon carbide ceramic experiences grain growth, resulting in a more brittle material prone to cracking during cool-down and with decreased strength properties[107]. The proposed solution for this problem was to introduce heteroatoms into the ceramic, including titanium and boron to function as grain growth inhibitors. Introduction of boride dopants as grain-growth inhibitors prevent the decreases in strength observed with the growth of silicon carbide grains as both cure and operational temperatures increase[108]. This work details the modification of

a commercially available silicon carbide pre-ceramic polymer to contain titanium and boron, and to produce a ceramic composed of silicon carbide and titanium diboride.

Commercially available fibers containing silicon carbide and 2-3% titanium diboride are available under the name Sylramic™. Sylramic™ SiC fiber (DOW-Corning Co, COI Ceramics, ATK Space Systems) is a high performance, full crystallized, boron-doped silicon carbide fiber. The elemental composition has previously been determined and is shown in *Table 4-1* [109].

Table 4-1. Chemical Composition of Sylramic™ Ceramic Fiber[109]

Element	Chemical Composition (Weight %)	Chemical Composition (Atomic %)
Silicon	66.6	46.7
Carbon	28.5	46.7
Oxygen	0.8	1.0
Titanium	2.1	0.9
Boron	2.3	4.2

The fiber contains titanium and boron additives for preventing large grain formation during the heating process. These materials act as grain-grown inhibitors, interrupting the formation of large particles of silicon carbide during high temperature heat-treatments[110]. This grain formation and sintering of silicon carbide results in decreased strength and durability of the fiber during high temperature applications, resulting in catastrophic component failure[111]. This ceramic fiber is available as continuous tow made of 800 x 10μm diameter filaments coated with polyvinyl alcohol sizing, or as woven fabric[109]. Sylramic™ fiber is notoriously expensive and limited quantities are produced each year. This research details a unique method for producing a polymer which pyrolyzes to a combination of ceramics similar to that of Sylramic™. The benefit of this polymer modification over other commercially available silicon carbide polymers for similar application is the incorporation of titanium and boron for prevention of grain growth during the heating process, preventing the loss of refractory properties in the material. The

advantage of this system over the similar commercially available fiber Sylramic™ is ease of synthesis, cost of production, and potential for uses outside of ceramic fiber.

The modified polymer was designed to use commercially available silicon carbide pre-ceramic polymer Starfire® SMP-10. This polymer, produced by Starfire® Systems, is relatively inexpensive, easy to use, and relatively stable under the conditions required for synthesis of the titanium modified polymer. The polymer does have some issues with air sensitivity, which are reflected in the adapted procedure for incorporation of the titanium into the polymer. General handling properties of Starfire® SMP-10 are summarized in *Table 4-2*, below[92].

Table 4-2. Properties of Starfire® SMP-10

Density	0.998 g/cm^3
Viscosity	40 – 100 cPs at 25°C
Solvent Compatibility	Hexanes, THF, Toluene. Insoluble in Water
Storage	Vacuum Container or Inert Environment, 1-2°C
Green Cure Temperature	180 – 400°C
Amorphous SiC Formation Temperature	850 – 1200°C
Nano-crystalline SiC Formation Temp.	1250 – 1600°C
Ceramic Yield*	72-78%
Silicon Carbide Formed	Near-stoichiometric

*** According to Technical Data Sheet**

Starfire® SMP-10 was chosen as the polymer for further modification due to a familiarity with its properties, as well as the ease of purchase, cost, and reasonable stability. The polymer was modified in a two step process, incorporating titanium and boron into the material separately. First, titanium isopropoxide was used as a precursor, incorporating titanium into the structure of the polymer and resulting in a color change and eventual gelling of the polycarbosilane. The second step incorporated boron into the polymer during a boron trichloride heat treatment, taking advantage of titanium's property as a scavenger for atoms like carbon and boron and forming titanium diboride simultaneous with silicon carbide as the polymer was heated[112,113,114]. The two step-process simplified the conditions under which the titanium and boron were

incorporated by combining the polymer cure process with the boron incorporation step. The material was characterized extensively at several steps during the synthesis process, as well as during the ceramic formation process to determine the effect of temperature on the material and to identify phases during the crystallization process. These characterization methods were compared to the neat SMP-10 polymer to determine the effects of adding both titanium and boron to the polymer. Two 4"x4" CMC panels were fabricated, one of neat SMP-10 and one of TiB_2-Modified SMP-10, to determine differences in the fabrication process and the effect of the dopants on overall composite strength.

4.2 Experimental

4.2.1 Polymer Synthesis

A typical synthesis of the titanium modified polymer was carried out as follows:

Toluene (Sigma-Aldrich) SMP-10 (Starfire®) and titanium isopropoxide (Alfa Aesar) were added to a flask under constant nitrogen purge and stir. Concentrations of titanium isopropoxide were varied as required for the polymer synthesis and characterization, varying from between 5 and 50 weight percent titanium isopropoxide to SMP-10. The liquid was heated to just below reflux until the clear yellow liquid turned opaque and black, or for about one hour. This titanium incorporated liquid polymer was transferred to an alumina boat and placed into a tube furnace with Cajon fittings, shown in *Figure 4-1*.

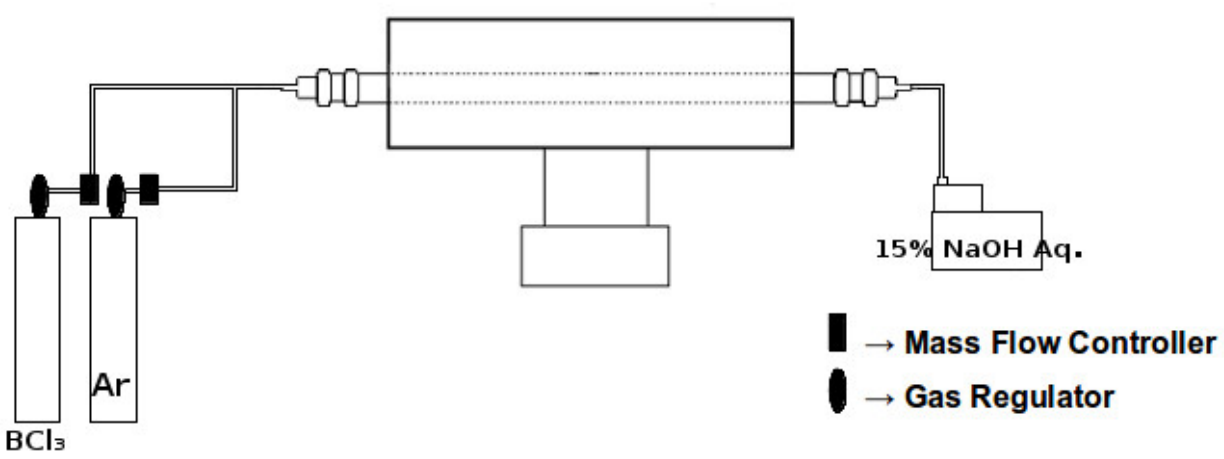

Figure 4-1. Reactor Setup for Boron Trichloride Heat Treatments

Argon (UHP, 200 sccm, Airgas) was flowed through the furnace to purge the entire system of all air. Once purged, the sample was heated at 10°C per minute until the desired temperature at which boron trichloride would be introduced. In an example heat treatment, the titanium incorporated polymer was heated to 900°C at 10°C/ minute, then boron trichloride gas (Sigma Aldrich, 20 sccm) was introduced to the system with the flowing argon (200 sccm) from 900°C to 1200°C at the 10°C/ minute ramp rate. The boron trichloride was then shut off and the sample was continuously heated to 1600°C at 10°C/minute, held for 20 minutes, and cooled to 800°C at 10°C/minute before cooling to room temperature under flowing argon.

4.2.2 Continuous Fiber Reinforced (CFR) Ceramic Matrix Composite Fabrication

CFR CMCs were fabricated using both Neat SMP-10 and TiB_2-Modified SMP-10. CG-Nicalon™ SiC Fabric (approximately 25" x 30") was coated with a duplex interface coating of ~100 nm of boron nitride and ~50 nm of silicon carbide using LP-CVD procedures described in **Section 2.4.2.2**. This fabric was then cut into 4.5"x4.5" plies, producing a total of 8 panels

for each composite. Plies were arranged in alternating-warp direction and set aside. Polymer (~300 grams) was mixed with 20 grams of fine silicon carbide powder (Alfa Aesar, <10 micron, Alpha phase) until combined. Individual fabric plies were saturated with the polymer mixture through dip-coating and were carefully aligned in a steel compression mold lined with Kapton®.

Plies were dipped quickly and assembled in the press, minimizing the time exposed to air. The compression mold was then closed and the bolts were fastened and tightened until the mold could not be compressed anymore. The entire compression mold was put into a vacuum furnace, sealed to 30 mm Hg, and heated to 250°C for 24 hours. After this cure process, the mold was cooled, opened, and the green-body composite was removed. The frayed edges were trimmed using a circular saw with a diamond cutting blade, reducing the panel to about 4" x 4". The panel was then cut into four 1"x4" sections and pyrolyzed to 1600°C under argon (for the neat SMP-10 CMC) using the same heating procedure described in **Section 3.3**. The Ti-modified CMC was heat treated using BCl_3 using the procedure described in **Section 4.2.1**.

Impregnations were performed using 20 mL of either SMP-10 for the Neat composite or 20 mL of freshly synthesized Ti-Modified SMP-10 for the TiB_2-CMC. Composite pieces were placed in a plastic bag with the polymer and saturated completely before being placed inside a vacuum oven at 30 mm Hg overnight. The CMC pieces were then removed from the plastic bag, returned to the vacuum furnace, and heated to 250°C for 24 hours to cure the polymer. Pyrolysis and BCl_3 heat treatment procedures to 1600°C were followed as described in the previous paragraph. Impregnations were performed until a maximum density plateau was achieved.

4.3 Characterization

Polymer samples were analyzed with Thermo-Gravimetric Analysis and Mass Spectrometry (TG-MS) Evolved Gas Analysis using a Netzsch Instruments TG 209 F1 Libra® TGA coupled with a Netzsch Instruments QMS 403D Aëolos Quadrupole Mass Spectrometer. The Netzsch

Proteus Software c-DTA® program was used to determine endothermic and exothermic events based on the difference in the theoretical liner temperature rate of heating and the temperature measured at the bottom of the sample crucible. Polymer samples were heated to 900°C at 10°C / minute in 50 sccm of argon and MS bar graph scans were performed for masses 1-50 sensitivity at a scan speed of 0.2 seconds.

All pyrolyzed materials were examined for crystalline phases using X-Ray Diffraction with a Rigaku Ultima IV X-Ray Diffractometer with Rigaku RINT2200 XG Software and a Cu Kα X-Ray source with a beam voltage of 44 kV and 40 mA beam current with slit lengths at 2/3, 10, 2/3, and 0.3 mm. Scans were performed from 20 to 80° with a scan rate of 2.0°/ min. Samples were heated at 10°C / minute and held at the final temperature for 30 minutes in 50 sccm flowing argon. X-Ray diffraction patterns and phases were verified by JCPDS and Rigaku RINT2200 XG Software.

All pyrolyzed materials were characterized using either a FEI Nova NanoSEM 450 Scanning Electron Microscope with a Everhart-Thornley Detector and with X-Max 80 Silicon Drift Detectory or a JEOL JSM-6335F Field Emission Scanning Electron Microscope with a voltage range of between 2.00 to 4.00 kV and a beam current of 1 -2 mA. Coating thicknesses and coating adhesion were investigated using SEM .

Energy-Dispersive X-Ray Spectroscopy was used to determine elemental distribution and was performed using an Oxford Instruments EDS with Aztec Instruments Nanotechnology Microanalysis System. Map scans were performed at a working distance of 5.3 mm with a Process Time of 4 and High Voltage at 0.2 kV.

Three-Point Bend Testing was used to determine the maximum Flexural Stress of the composites. This was performed using an Instron™ 5869 Testing Machine with a 3-Point Contact System. The support span was 10 cm and the rate of the crosshead piece was 0.5 mm/ second. Pyrolyzed samples were heated at 10°C / minute and held at the final temperature for

30 minutes in 50 sccm flowing argon, cooled, ground with an alumina mortar and pestle, and mounted on aluminum stubs with conductive carbon tape.

4.4 Results

4.4.1 Thermo-Gravimetric Analysis / Mass Spectrometry

Thermo-Gravimetric Analysis was used to determine the ceramic yield of both Starfire® SMP-10 and titanium-modified Starfire® SMP-10 during the pyrolysis process of the polymers, as well as to observe mass losses corresponding to events occurring during the formation of the ceramic. Starfire® SMP-10 was studied extensively to propose a mechanism of ceramic formation based on the Evolved Gas Analysis. The Netzsch Proteus Software c-DTA® program was used to determine both endothermic and exothermic events based on the difference in the theoretical liner temperature rate of heating and the temperature measured at the bottom of the sample crucible. Polymer samples were heated to 900˚C at 10˚C / minute in 50 sccm of argon. The thermograms for both the neat and Ti-modified polymer and c-DTA® curves are shown in *Figures 4-2 and 4-3*.

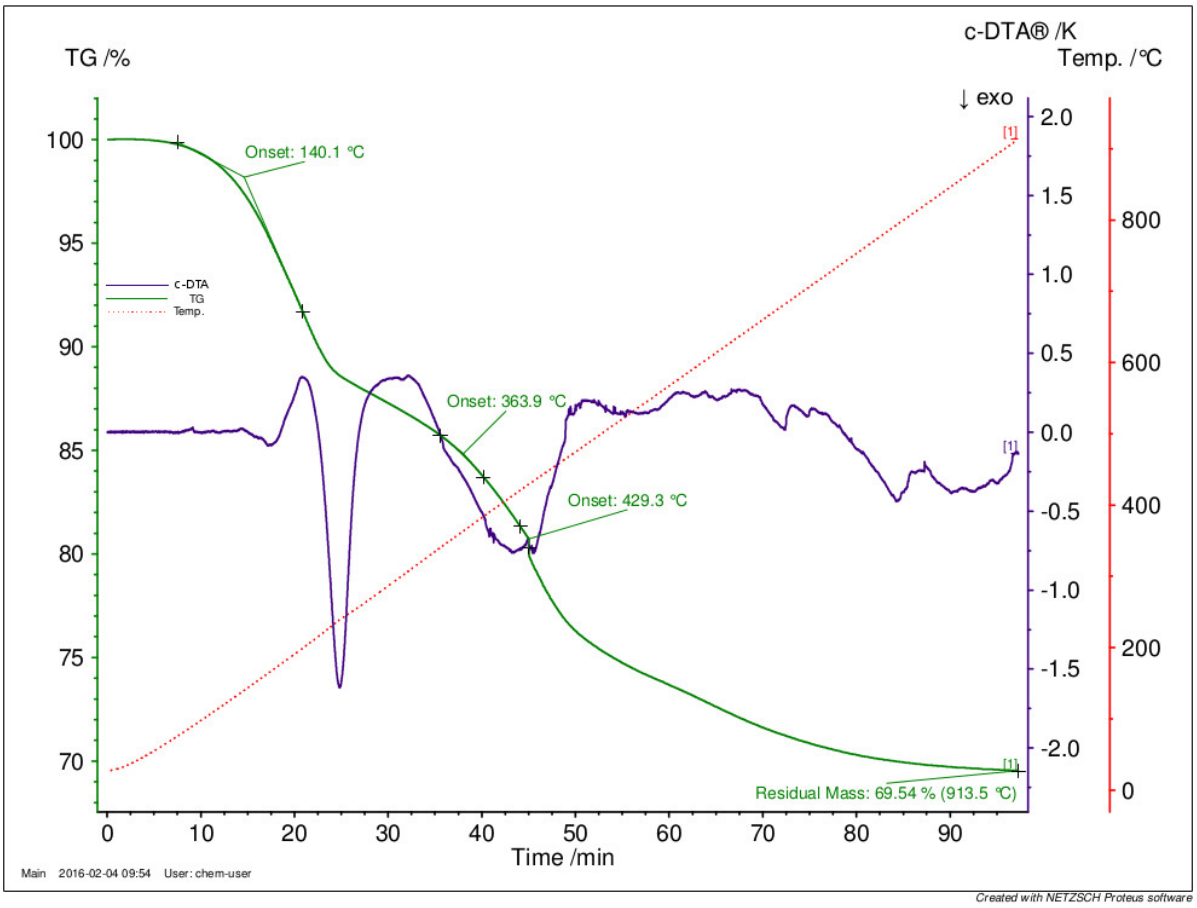

Figure 4-2. TG Curve and c-DTA® for SMP-10 Polymer Heated to 900°C

The residual mass of the neat SMP-10 was reported to be 69.54%, and inflections were observed at 140.1°C and 363.9°C and 429.3°C. These mass losses corresponded to exothermic events in the c-DTA® at both 140.1°C and 363.9°C, as seen in *Figure 4-3*.

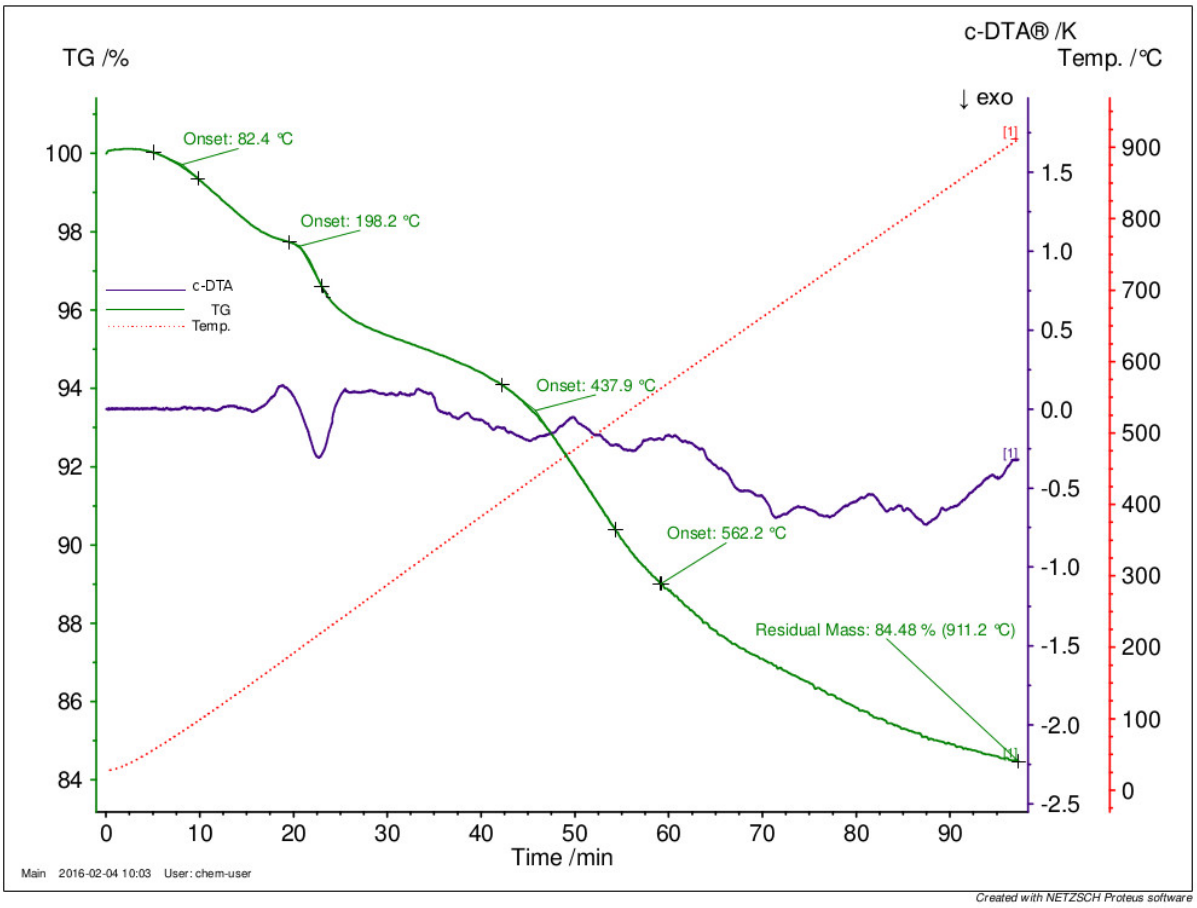

Figure 4-3. TG Curve and c-DTA® for Ti-Modified SMP-10 Polymer Heated to 900°C

The residual mass of the Ti-modified polymer was 84.48%, and mass losses were observed at 80.4°C, 198.2°C, 437.9°C, and 562.2°C. The c-DTA® showed an exothermic event at 198.2°C and slight exothermic nature in the 562.2°C range.

ThermoGravimetric Analysis coupled with Mass Spectrometry (TG-MS) was used to identify the evolved gas species produced as the polymer was heated for both the near SMP-10 and the Ti-modified polymer. These data were correlated to the mass losses on the TG curve and appear in the stacked plots in *Figures 4-4 and 4-5*. The MS data for the neat SMP-10 showed signals for masses 15, 18, 30, 32, and 44. The signal for m/z 18 exhibited an increased

signal corresponding with the mass loss at 140.1°C, and m/z 15, 30, and 44 showed increases in signal correlating with the mass losses at 363.9°C and 429.3°C.

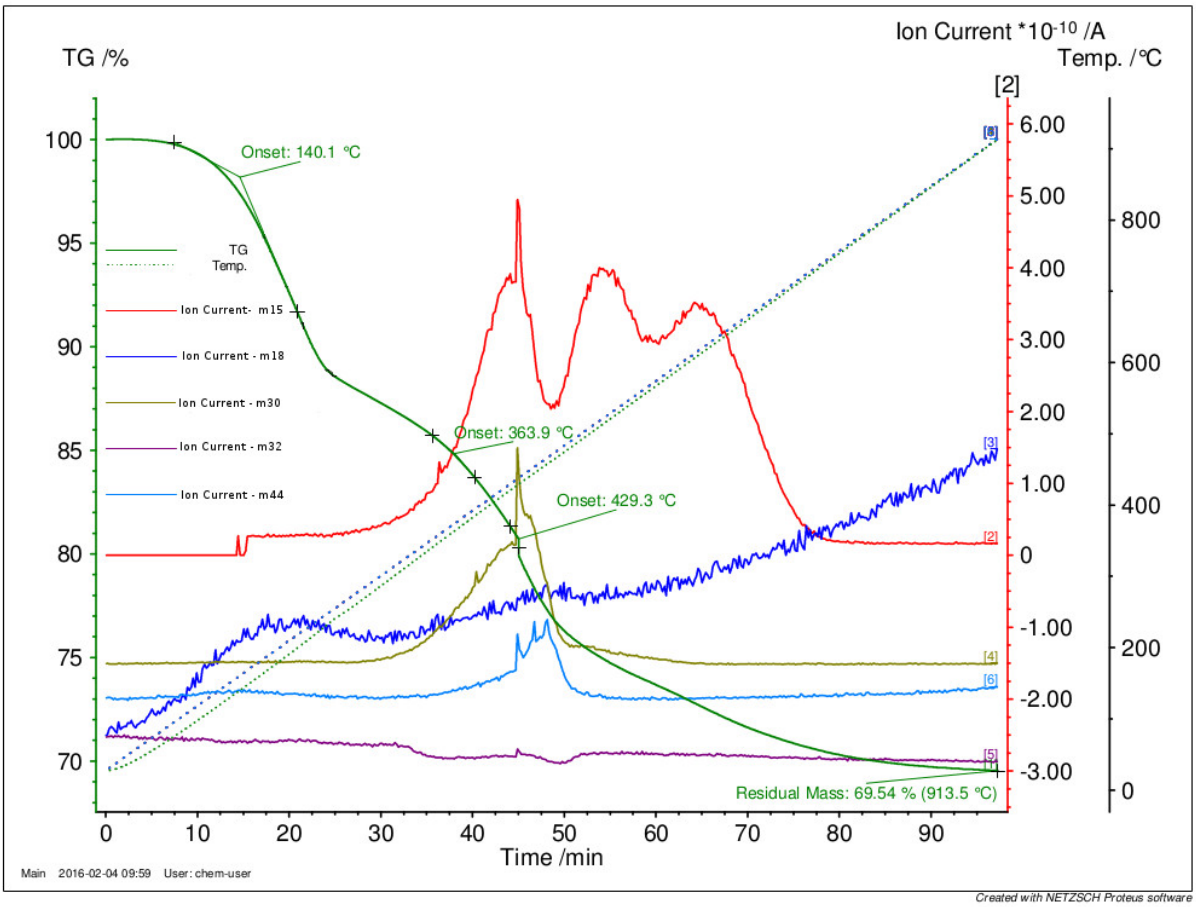

Figure 4-4. TG Curve and MS Data for SMP-10 Polymer Heated to 900°C

The MS data for the Ti-modified SMP-10 showed signals for mass/charges (m/z) 15, 18, 27, 28, 32, and 44. The signal for m/z 18 exhibited an increased signal corresponding with the mass loss at 82.4°C and 198.2°C, and m/z 15, 27, and 28 showed increases in signal correlating with the mass loss at 198.2°C. Signals for m/z 15, 27, 28, 30 correlated with the mass losses in the TG curve between 437.9°C and 562.2°C.

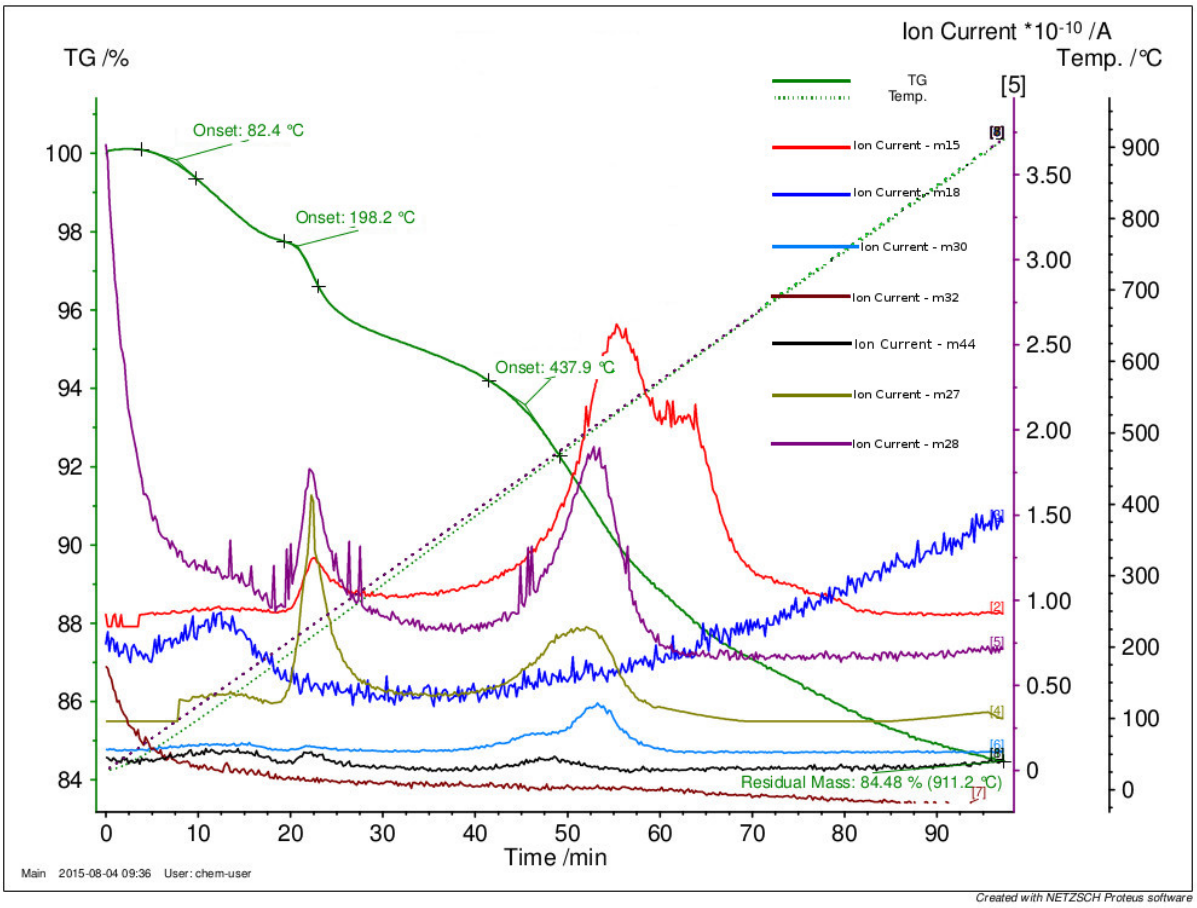

Figure 4-5. TG Curve and MS Data Ti-Modified SMP-10 Polymer Heated to 900°C

4.4.2 X-Ray Diffraction

X-Ray Diffraction data was obtained for variations of neat SMP-10 and of Ti-modified SMP-10 and TiB_2-modified SMP-10 polymer samples heated 1600°C under argon. The diffraction patterns for the neat SMP-10 is shown in *Figure 4-6*.

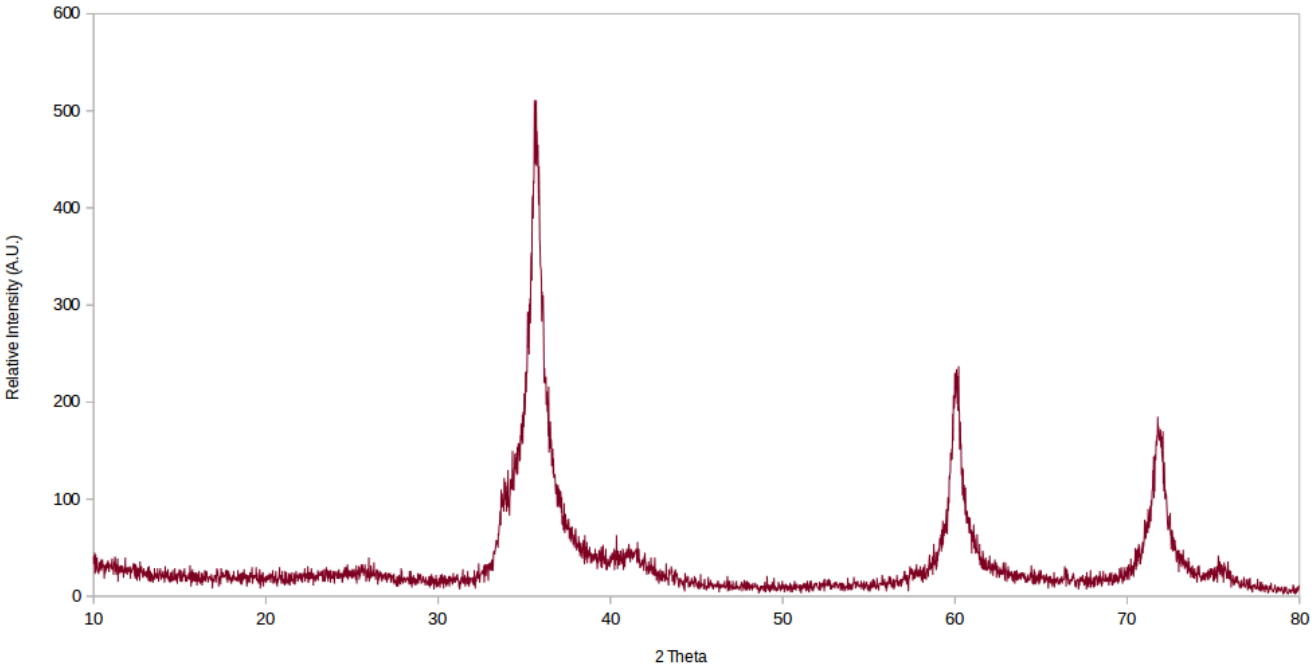

Figure 4-6. XRD Pattern for Starfire SMP-10 Pyrolyzed to 1600°C under Argon.

The diffraction pattern for neat SMP-10 showed five relatively sharp reflections at 2θ = 35.72, 44.48, 60.06, 71.82, and 75.64, with the most intense reflection at 2θ = 35.72

SMP-10 polymer modified with only titanium isopropoxide was pyrolyzed to 1600°C under argon to determine the effect of the titanium precursor only on the resulting ceramic. This plot, shown in *Figure 4-7*, contained reflections at 2θ= 35.72, 44.48, 60.06, 71.82, and 75.64.

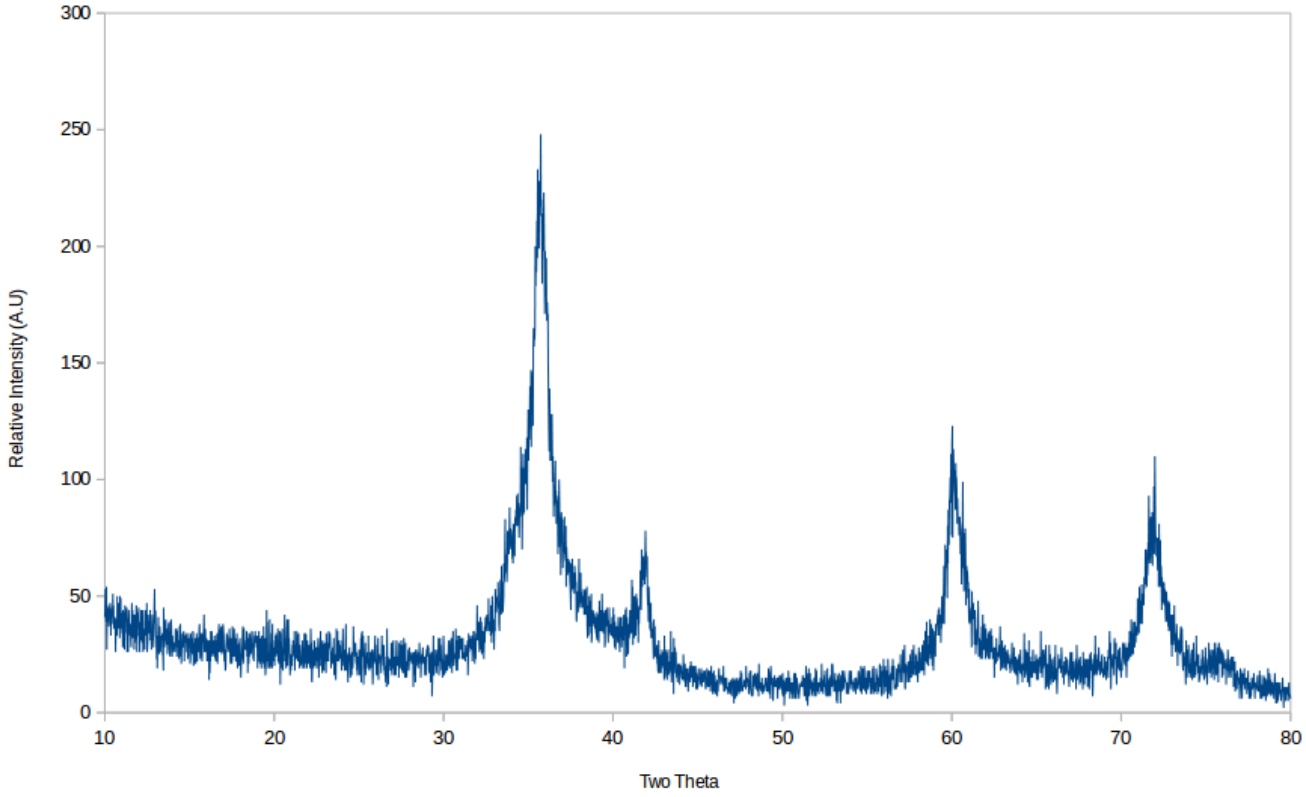

Figure 4-7. XRD Pattern for Ti-Modified Starfire® SMP-10 Pyrolyzed to 1600°C under Argon.

Polymers modified with both titanium precursor and boron heat-treatment were analyzed for their diffraction patterns. *Figure 4-8* displays the diffraction patterns for SMP-10 modified with both 10 weight percent and 50 weight percent titanium isopropoxide. This experiment was performed to further resolve the smaller signals initially observed in the diffraction pattern. These signals are summarized in *Table 4-3*, and signals that were observed in the 50% Ti-incorporated sample but not the 10% Ti-incorporated sample are designated with a "-".

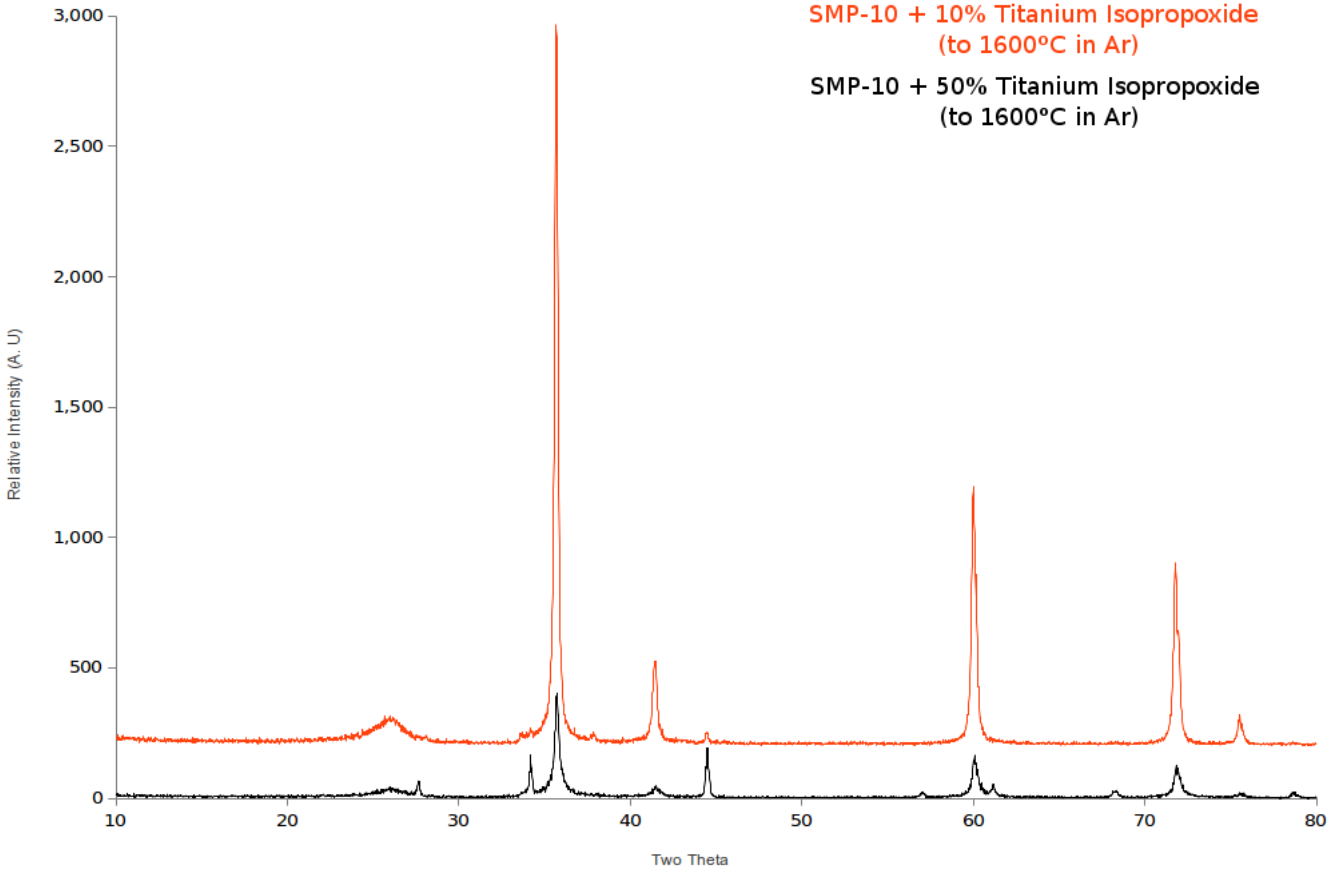

Figure 4-8. XRD Pattern for 10% and 50% Ti and Boron-Modified Starfire® SMP-10 Pyrolyzed to 1600°C under Argon.

Table 4-3. Summarized 2θ Values for XRD of 10% and 50% Ti-Modified SMP-10 Ceramic

10% Ti-Modified SMP-10	50% Ti-Modified SMP-10
~26.22	26.42
-	27.68
-	34.20
35.66	35.52
41.44	41.50
44.48	44.50
-	56.94
60.02	59.98
-	61.18
-	68.34
71.78	71.74
75.52	75.46
-	78.66

A temperature study was performed to determine the effect of the temperature at which the boron-heat treatment occurred at on the phases present and the crystallinity of the resulting ceramic. Titanium-modified SMP-10 samples were heated at 10°C per minute under argon until the desired temperature was reached, after which heating of the samples continued under flowing boron trichloride. The temperature ranges at which the samples were exposed to BCl_3 is noted in *Figure 4-9*. All samples were heated to 1600°C during this temperature study and the reflections present were near-identical to the reflections in *Table 4-3*.

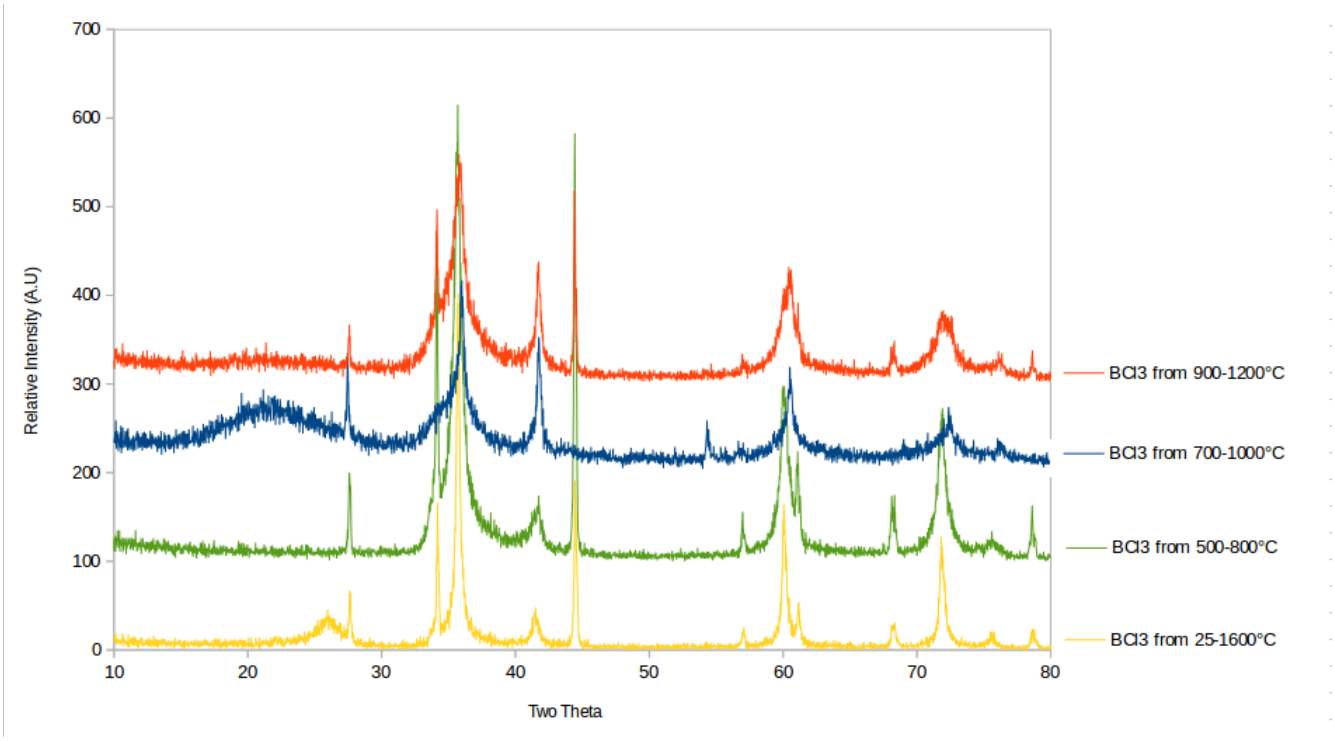

Figure 4-9. XRD Temperature Study of BCl_3 Treatment on Ti-Modified SMP-10

4.4.3 Scanning Electron Microscopy

Ceramic samples of SMP-10, 5% Ti-modified SMP-10, and TiB_2-modified SMP-10 after pyrolysis to 1600˚C were analyzed using SEM to determine the effect on bulk and surface morphology and grain size. These micrographs appear in *Figures 4-10, 4-11, and 4-12*, respectively.

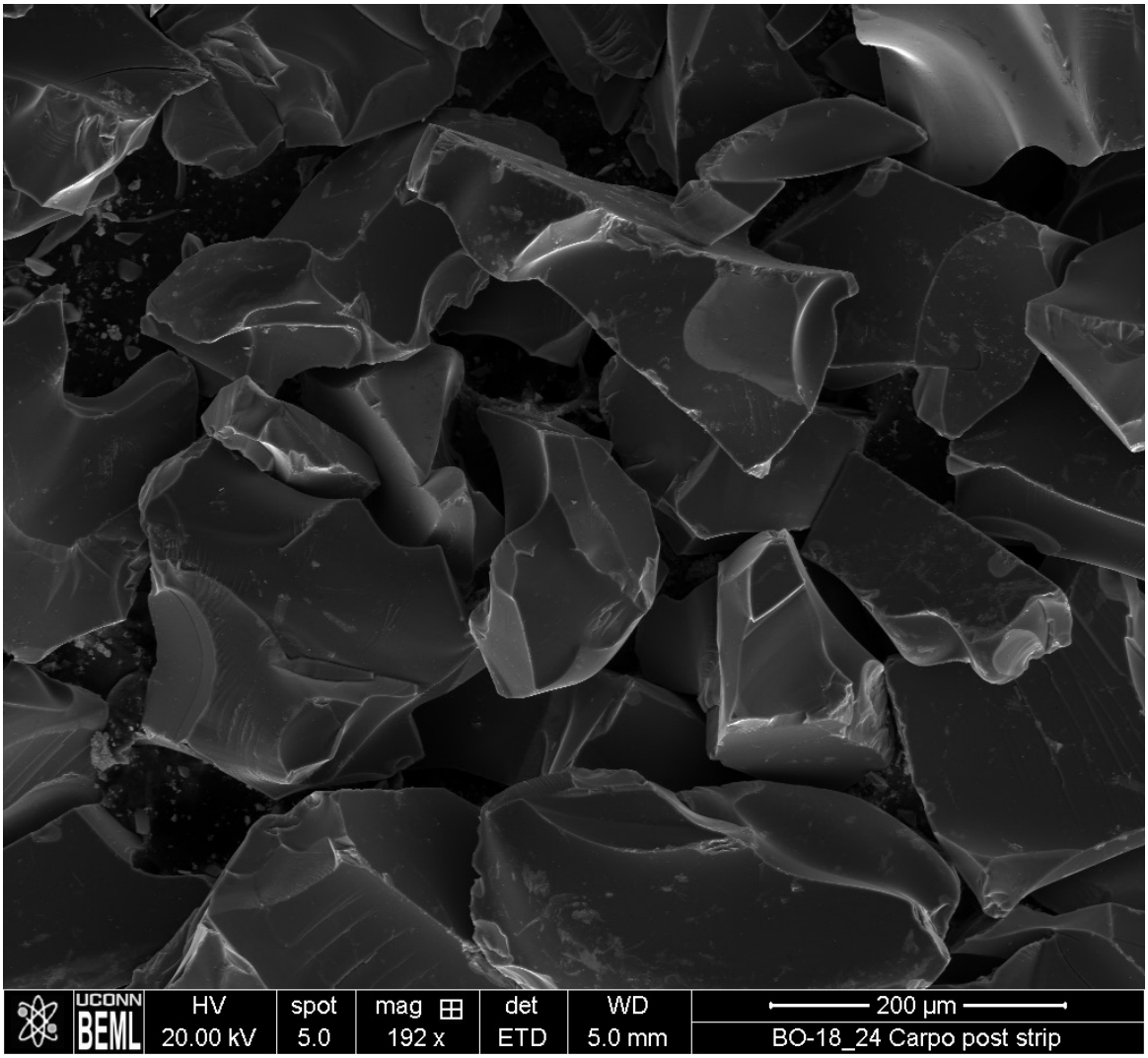

Figure 4-10. SEM Micrograph of Neat SMP-10 Pyrolyzed to 1600°C

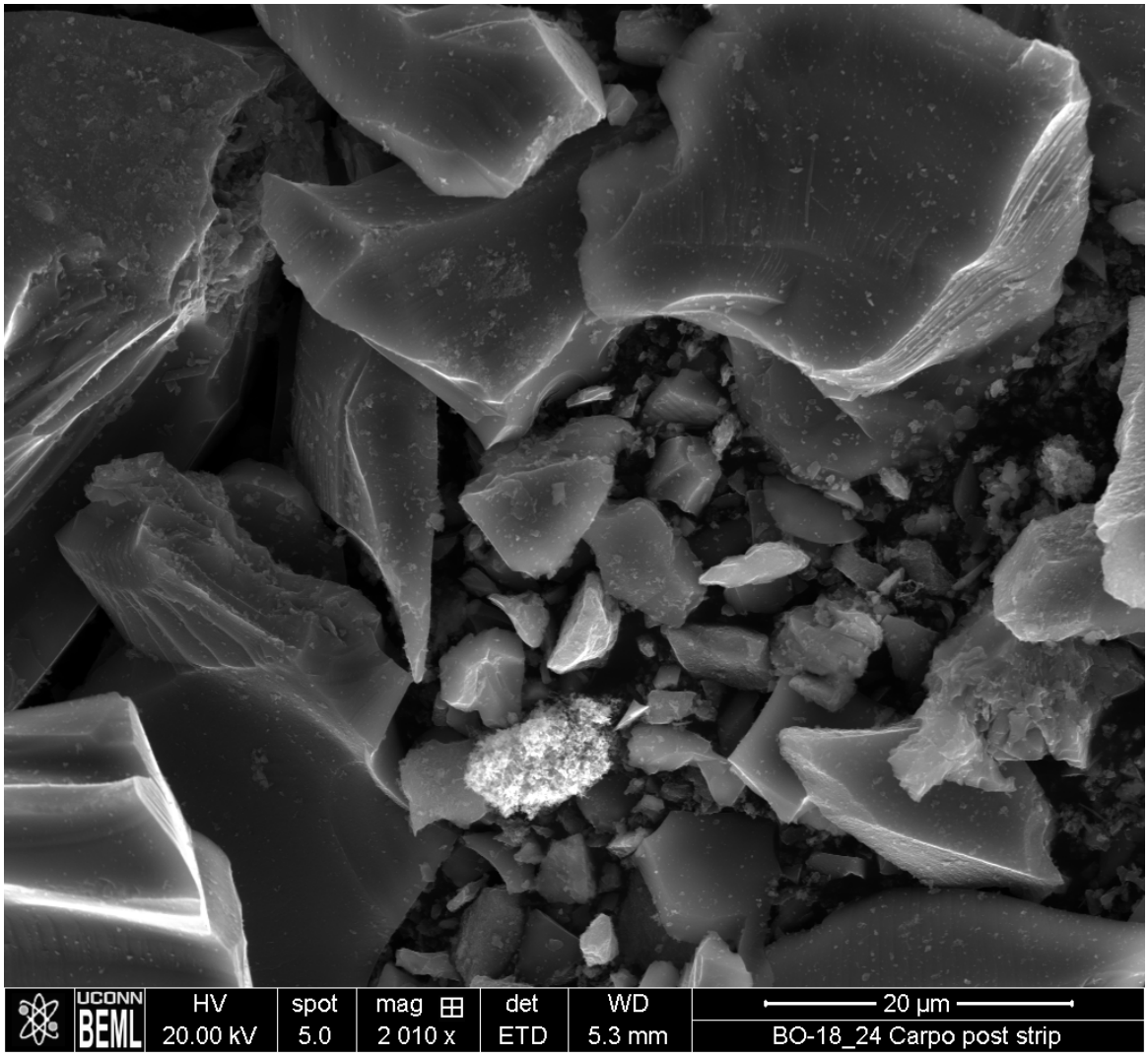

Figure 4-11. SEM Micrograph of Ti-Modified SMP-10 Pyrolyzed to 1600°C

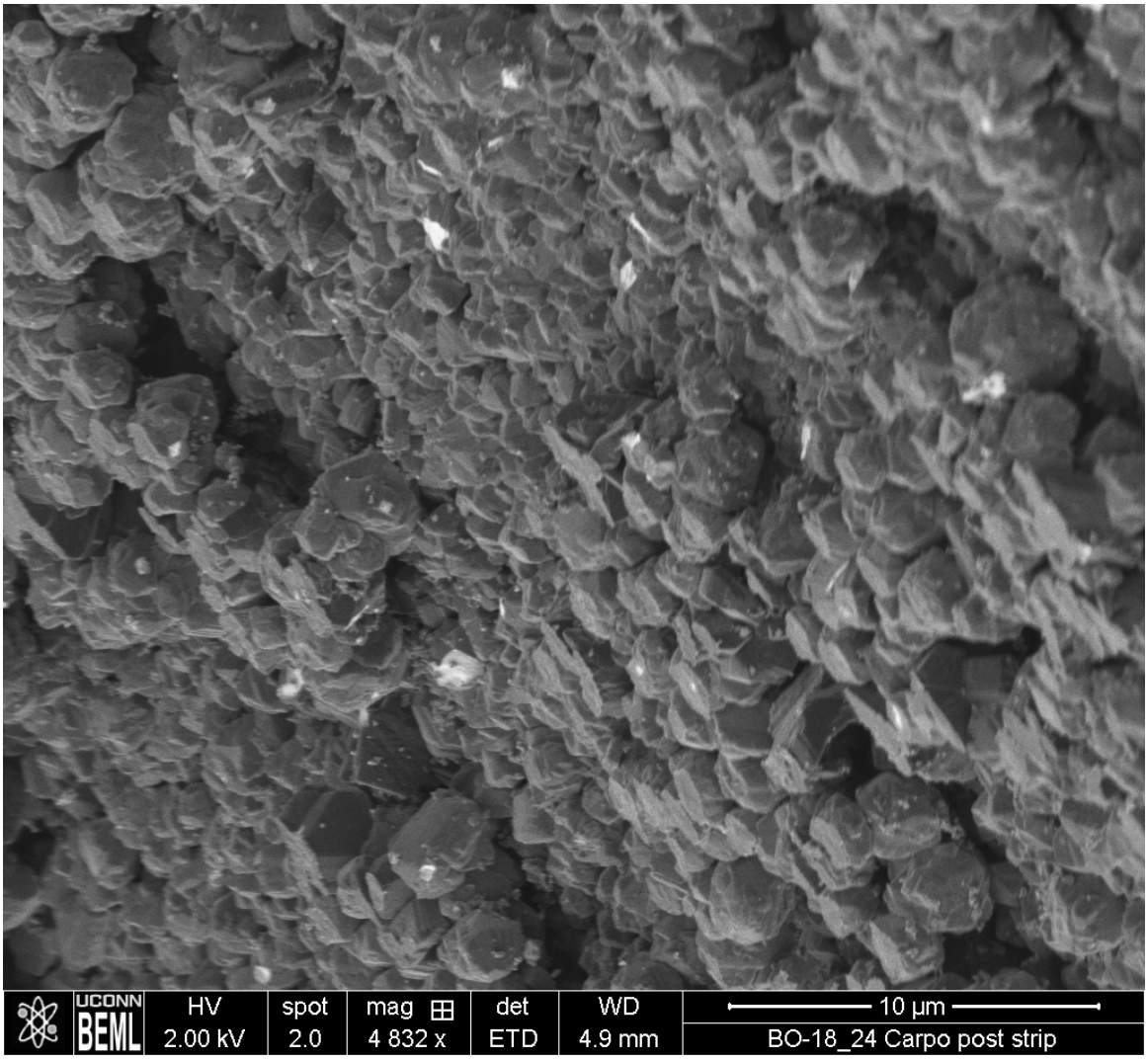

Figure 4-12. SEM Micrograph of TiB_2 Modified SMP-10 Pyrolyzed to 1600°C

The micrographs in *Figures 4-10 and 4-11* showed jagged, irregular fragments of ceramic material. The edges were angled and sharp and the surfaces were smooth and relatively uniform. The neat SMP-10 contained grains in the hundreds of micron range, while the Ti-modified SMP-10 contained slightly smaller grains in the 20-100 micron size range. The TiB_2-modified SMP-10 (*Figure 4-12*) had an entirely different morphology, contrasting with small, uniform cluster-like structures in the 1-5 micron range. These clusters were clumped together in a consistent plane and appeared to be polyhedra-like, as compared with the jagged and irregular grains in the other ceramic samples.

4.4.4 Energy Dispersive X-Ray Spectroscopy

Ceramic samples produced for SEM were also analyzed using EDS to determine elemental composition and distribution. Ceramic samples of SMP-10, Ti-modified SMP-10, and TiB_2-modified SMP-10 after pyrolysis to 1600°C were analyzed using EDS. The spectrum for Neat SMP-10 is shown in *Figure 4-13* and showed the presence of carbon, silicon, and oxygen as expected for this polymer.

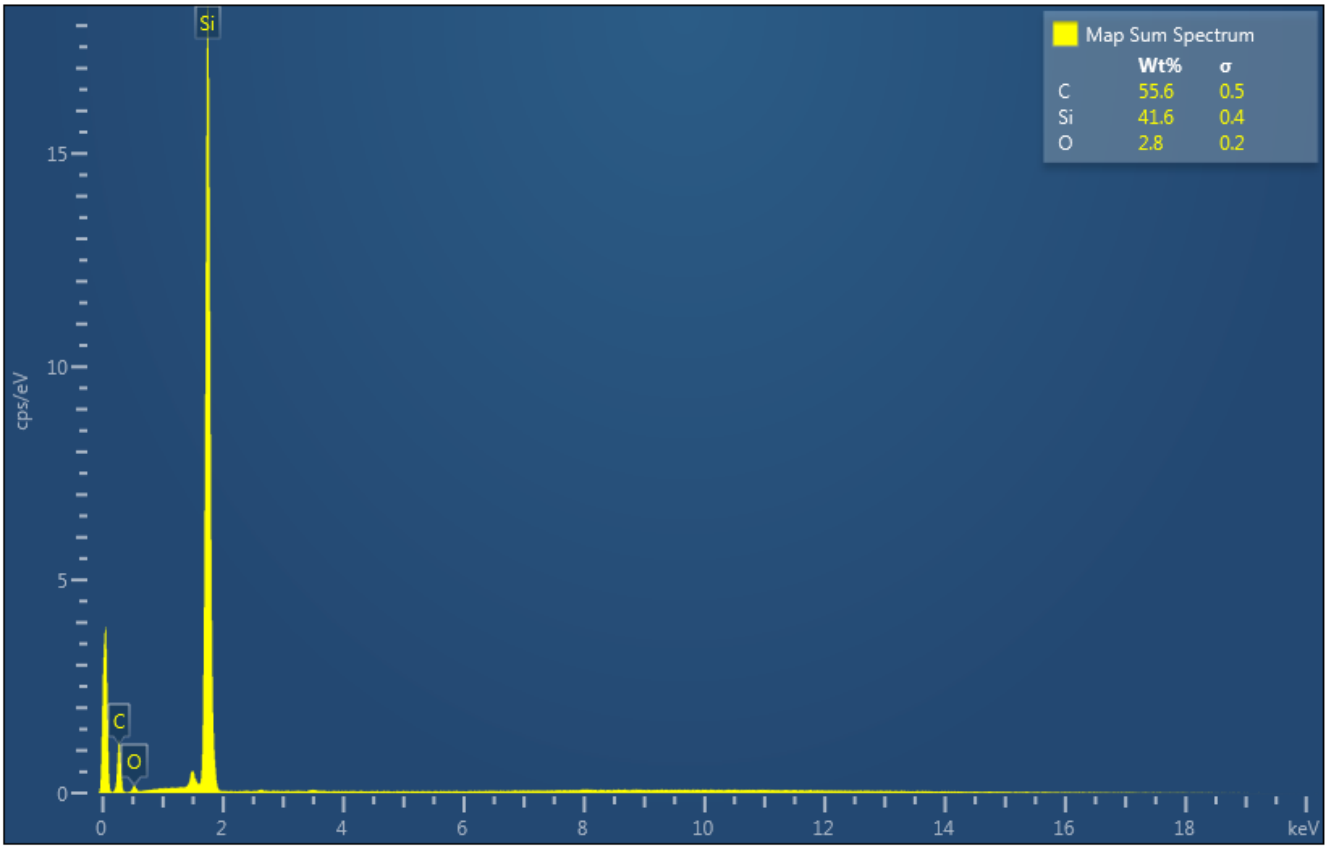

Figure 4-13. EDS Spectrum of Neat SMP-10 Cured to 1600°C

Elemental mapping was used for the Neat SMP-10 in *Figure 4-14* and showed an even distribution of both carbon and silicon across the sample. The oxygen concentration was low (below 3 Wt %) and did not appear significant in the elemental mapping.

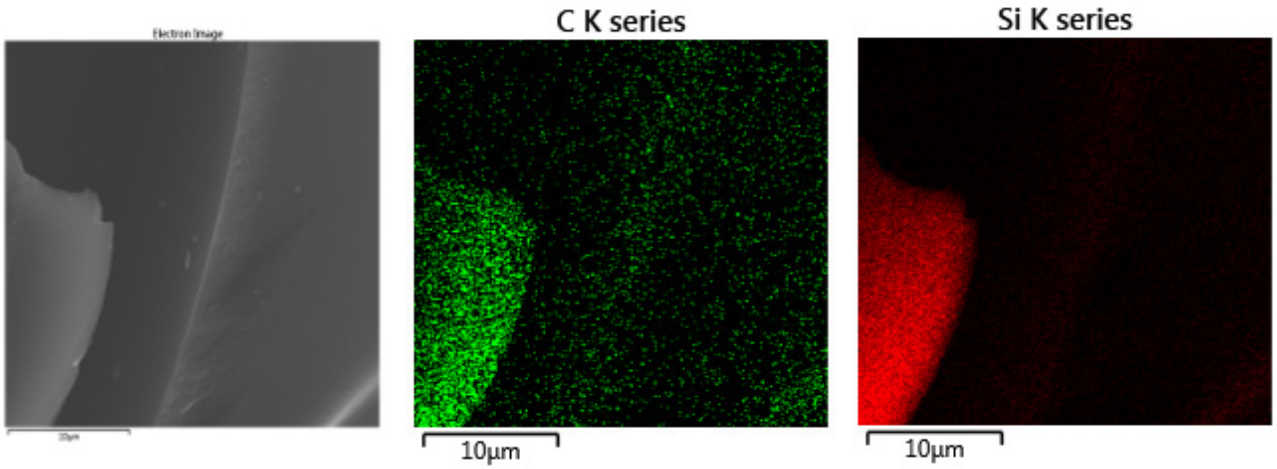

Figure 4-14. Electron Image and EDS Elemental Mapping of Si and C in Neat SMP-10

The EDS spectrum for the 5% Ti-modified SMP-10, observed in *Figure 4-15* indicated the presence of silicon, carbon, oxygen, and titanium, with residual signals from chlorine contaminants. The concentrations of carbon and silicon were similar to each other, and the concentration of oxygen was higher than that of the neat SMP-10, and the weight percent of titanium was 3.2%. Elemental mapping of the 5% titanium-incorporated polymer is shown in *Figure 4-16* and showed an even distribution of carbon, silicon, and titanium across the material.

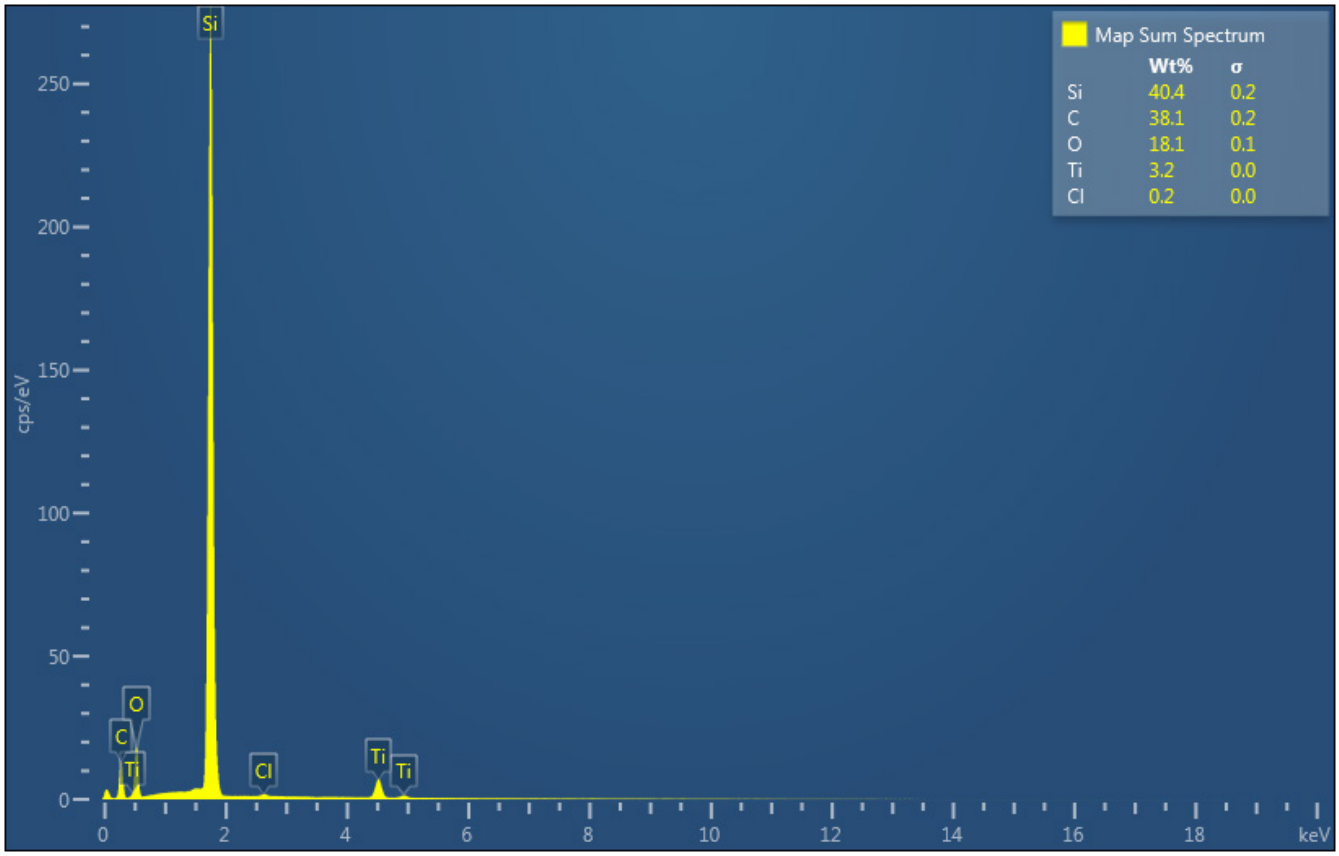

Figure 4-15. EDS Spectrum of Titanium Incorporated SMP-10 Cured to 1600°C in Argon

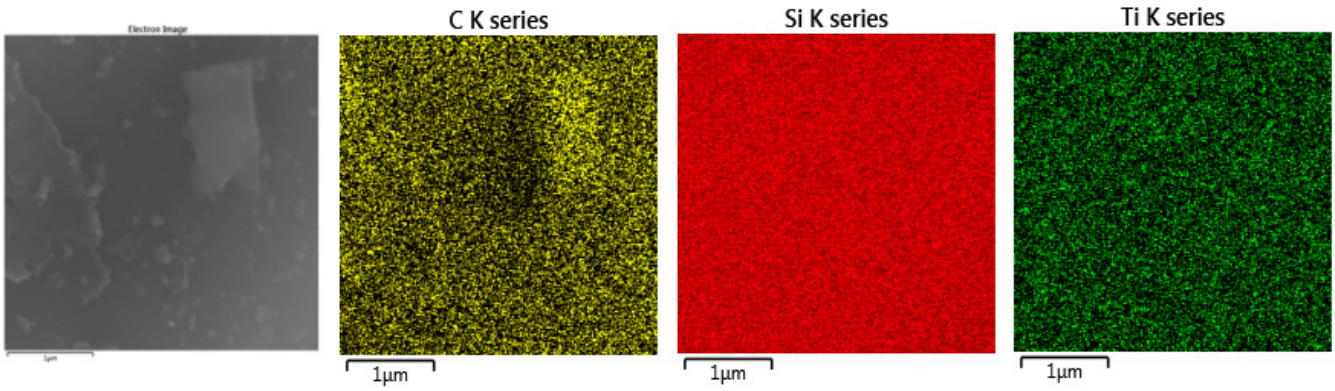

Figure 4-16. Electron Image and EDS Elemental Mapping of Si, C and Ti in Ti-Incorporated SMP-10

The EDS spectrum for the titanium and boron-modified SMP-10 appears in *Figure 4-17* and showed the presence of boron, carbon, silicon, and titanium. The weight percent of boron,

carbon, and silicon were similar to each other, and the weight percent for titanium was quite low, at 0.1%. Elemental mapping of the ceramic is displayed in *Figure 4-18*, and showed a direct correlation between silicon and carbon in the material, as well as between boron and titanium. There was no overlap of the Si-C mapped areas and the Ti-B areas.

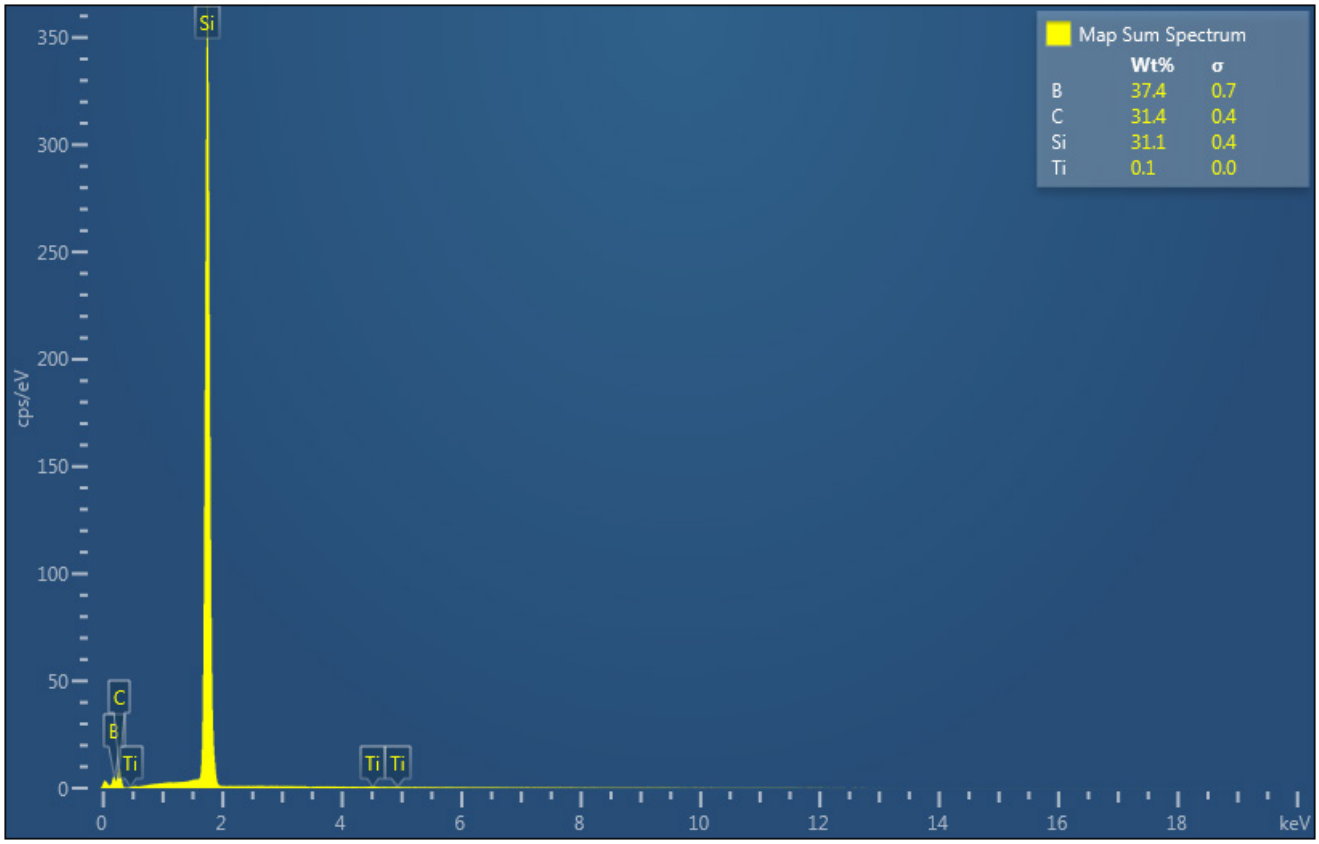

Figure 4-17. EDS Spectrum of Titanium and Boron Incorporated SMP-10

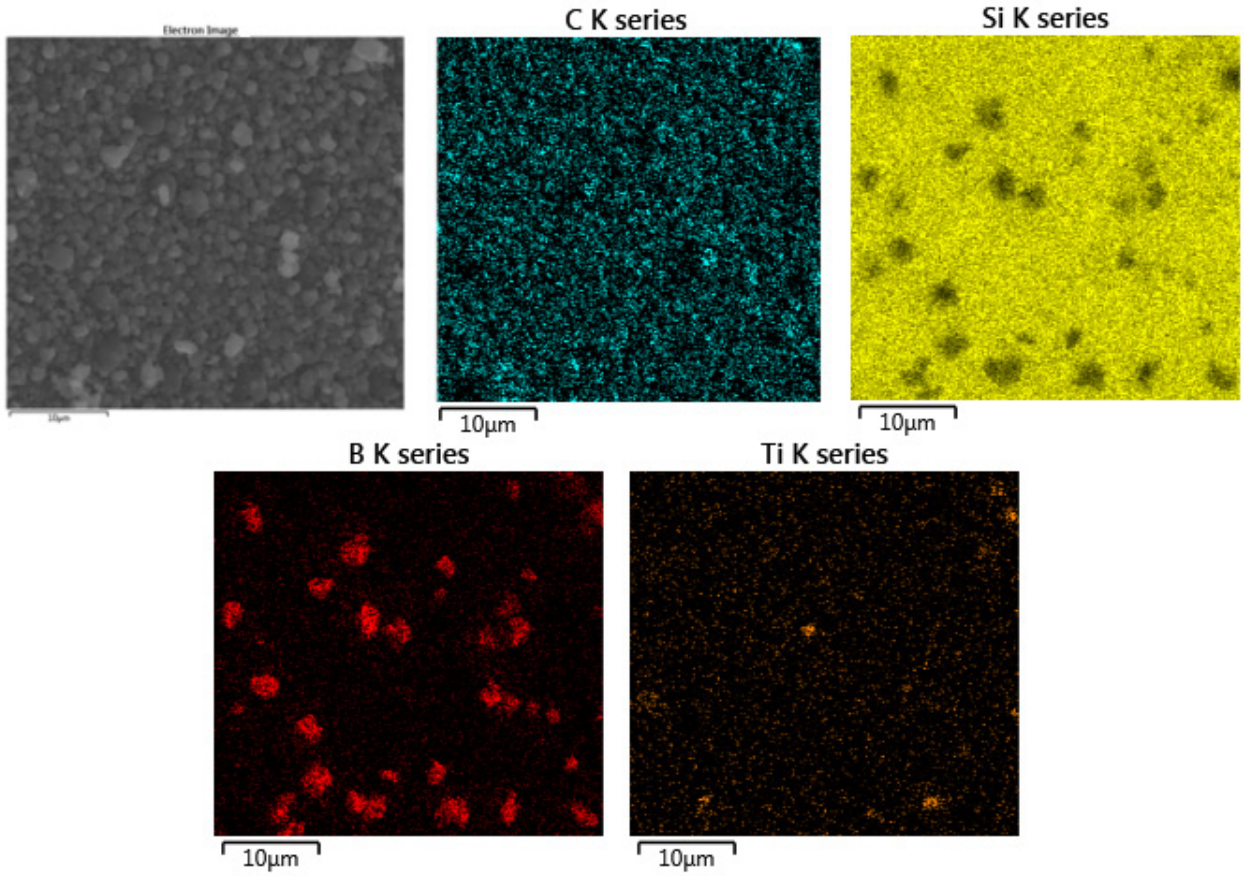

Figure 4-18 Electron Image and EDS Elemental Mapping of C, Si, B and Ti in Ti and B-Incorporated SMP-10

4.4.5 Composite Fabrication and Mechanical Testing

Ceramic matrix composites were fabricated according to the procedures described in **Section 4.2.2**. Both the Neat SMP-10 composite, as well as the SMP-10 TiB_2 composite were impregnated until the density no longer increased per impregnation. Average density was determined for each 1" x 4" piece by calculating the volume by measuring the length, width and height with a digital caliper, dividing this volume by the mass, and averaging the densities of the four pieces. Plots showing the average density for the panels per impregnation cycle are shown in *Figures 4-19 and 4-20*, and the maximum density for the Neat SMP-10 CMC was 2.05 g/cm^3 while the density for the SMP-10 TiB_2 CMC was 1.84 g/cm^3.

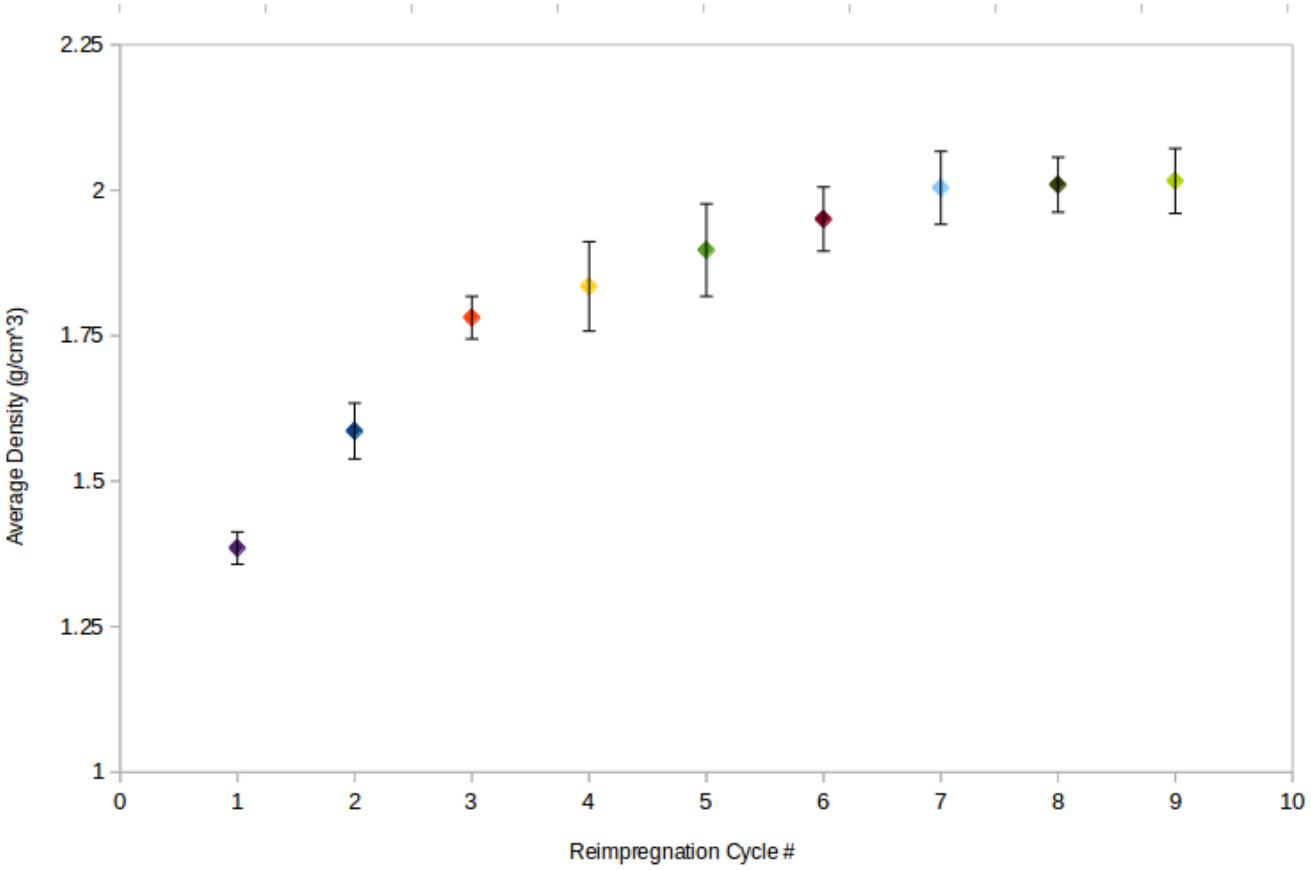

Figure 4-19. Density for Impregnation Cycles for Neat SMP-10 Composite

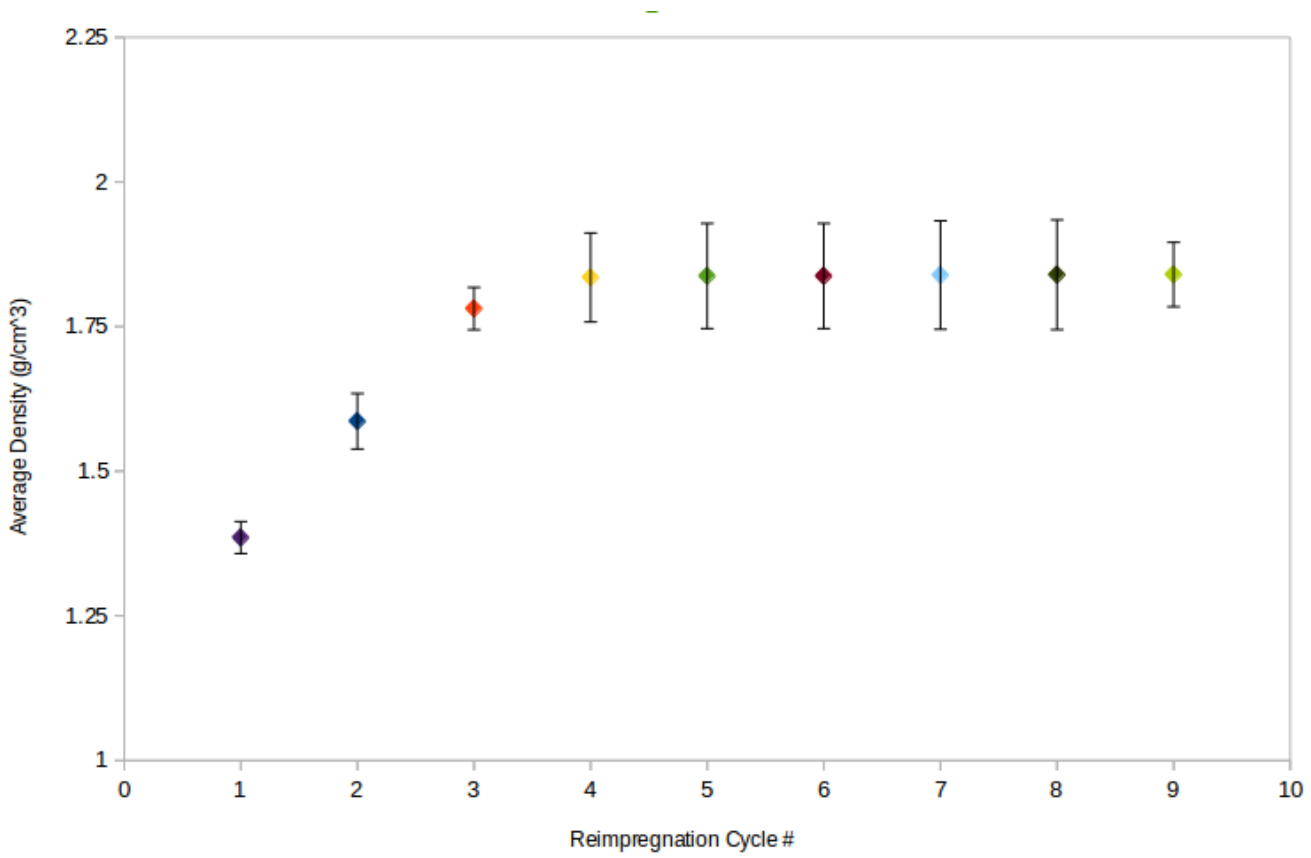

Figure 4-20. Density for Impregnation Cycles for SMP-10 TIB2 Composite

Three-point bend testing was performed on each of the composite strips for both the Neat SMP-10 CMC and the SMP-10 TiB_2 CMC. A sample plot for Flexural Strength vs. Flexural Strain for the neat composite is shown in *Figure 4-21*. Averages for all the tests performed were calculated and are shown in *Table 4-4*.

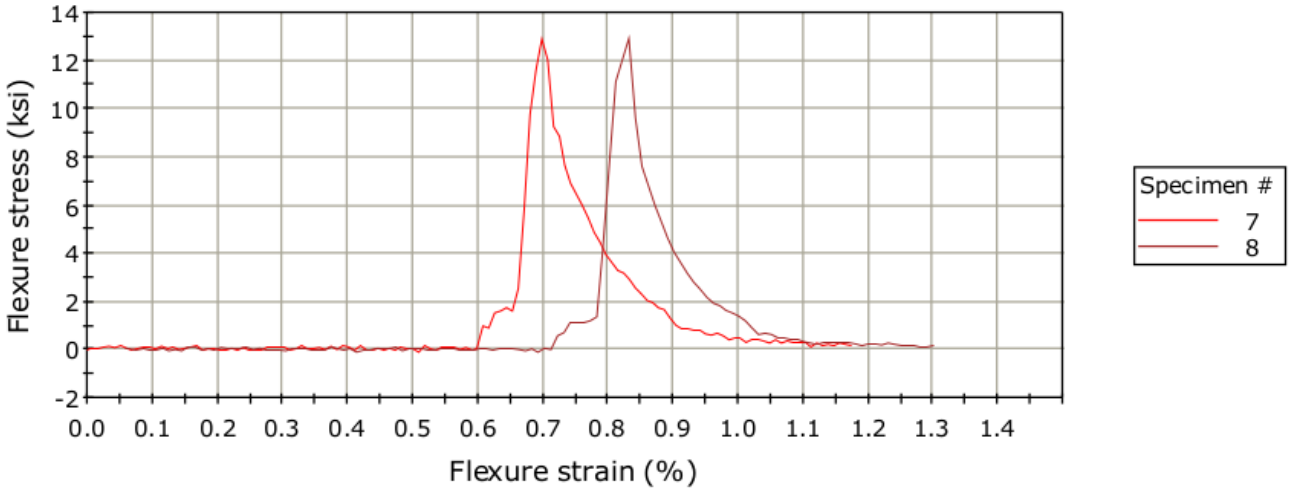

Figure 4-21. Plot of Flexural Stress vs. Flexural Stress from Three-Point Bend Test of SMP-10 CMC

Table 4-4. Average Flexural Stress for both PIP CMCs

	Flexural Stress (KSI)
Neat SMP-10 CMC	14.66 ± 2.15
SMP-10 TiB_2 CMC	15.20 ± 1.28

4.5 Discussion

4.5.1 Synthesis

Synthesis of titanium-modified polymer was achieved according to the detailed Experimental in **Section 4.2.1**. Time of reaction was dependent on the initial concentration of titanium isopropoxide. Higher concentrations (50 wt%) took less time to change to the green-black color and were much more prone to crosslinking, which was undesirable for composite fabrication. Lower concentrations of titanium isopropoxide incorporation (10 wt%, 5 wt%) resulted in slightly longer reaction times (~90 minutes) and were less prone to crosslinking. Crosslinked samples of any Ti concentration reverted back to the original state within a few hours after they were removed from the heat. Crosslinked samples, as well as liquid samples, were soluble

in ether, THF, and toluene, providing a variety of solvents for working use in an industrial application. The polymer was incompatible with water and became cloudy and gelled upon contact. This was expected with SMP-10 and was specified on the Technical Data Sheet[95].

Composites were fabricated according to the procedure described in **Section 4.2.2**. Both composites were fabricated with the addition of silicon carbide filler powder to the polymer used to coat the CG-Nicalon™ – BN-SiC Fabric. This filler was stirred in manually, and made the polymer very viscous and difficult to work with in the composite assembly. For the neat-SMP-10, crosslinking was not a significant concern because the polymer has moderate stability in air. Panels were dipped and assembled quickly to reduce exposure to air and moisture and the composite was loaded into compression form within a few minutes. Crosslinking of the SMP-10 was not experienced before the compression form was tightened and loaded into the vacuum furnace. In the case of the Ti-modified SMP-10, the polymer began to crosslink upon mixing with the silicon carbide filler. The polymer mixture was very viscous and the panels were difficult to coat uniformly with polymer. To ensure the panels were coated, the polymer mixture was rubbed into each panel before the panels were assembled into the compression form. The bolts in the form were difficult to tighten due to the viscosity and increased gelling of the polymer the longer it was exposed to air. Assembly of the CMC and tightening of the compression mold took about five minutes and the resulting composite was notably thicker than the neat SMP-10 CMC. Generally, increased viscosity and gelling of the polymer during CMC fabrication resulted in increased porosity and potential for decreased strength overall due to more pores and decreased density in the composite. The titanium-modified polymer was expected to be more air sensitive than the neat polymer, and future work could be modified to assemble the CMC under inert conditions to minimize crosslinking during the lay up process.

4.5.2 Thermo-Gravimetric Analysis / Mass Spectrometry

The TG curve of the Neat SMP-10 showed a residual mass of 69.54% while the TG curve of the Ti-modified SMP-10 had a residual mass of 84.48%. This increase in mass was likely due to the presence of titanium or titanium containing materials that remained in the ceramic and contributed to the increase in mass after pyrolysis.

C-DTA® curves for the Neat SMP-10 showed exothermic events near 250˚C, near the onset at 363.9˚C, and a general exothermic trend after 800˚C. The first exothermic event correlated to the loss of residual water in the polymer, while the second, less intense even was related to the loss of organic species like methane and ethane. The final series of exothermic events occurred due to the formation of silicon carbide near 800˚C and the beginning of crystallization of the ceramic from an amorphous material.

The TG curve and c-DTA® plot for the titanium modified polymer showed similarities to the neat polymer, with similar mass loss and exothermic event in the 200˚C range corresponding to the loss of water during the pyrolysis process. The Ti-modified polymer showed no significant exothermic event near 400˚C, but did undergo a mass loss slightly above this temperature range (437.9˚C) due to the loss of organic species. The Ti-modified polymer also showed a similar trend of exothermic events past 800˚C due to the formation of silicon carbide ceramic and the initial crystallization process. The TG-MS data for both the Neat SMP-10 and the titanium-incorporated polymer are summarized in *Table 4-5*.

Table 4-5. TG-MS m/z Values and Corresponding Species for SMP-10 and Ti-Modified SMP-10

	m/z ((g/mol)*charge-1)	Chemical Species Identified
Neat SMP-10	15	Mono-Atomic Oxygen (O)
	18	Water
	30	Ethane (C_2H_6)
	32	Diatomic Oxygen (O_2)
	44	Carbon Dioxide (CO_2)
Ti-Modified SMP-10	15	Mono-Atomic Oxygen (O)
	18	Water
	27	Vinyl Radical (C_2H_3)
	28	Ethylene (C_2H_4)
	30	Ethane (C_2H_6)
	32	Diatomic Oxygen (O_2)
	44	Carbon Dioxide (CO_2)

In the Neat SMP-10, the first inflection corresponded with a mass decrease occurring from loss of water, shown in the blue curve in *Figure 4-4*. Water loss was detected throughout the heating process of the polymer, though the noise in the signal indicated a low detection throughout the pyrolysis. The inflections at 363.9°C and 429.3°C correlated to the initial loss of methane and ethane from residual carbonaceous species in the polymer. Methane release appeared in three wave-like signals, consistent with the mass losses below 500°C. This TG signal also corresponded with a small decrease in the oxygen signal, simultaneous with the detection of a carbon dioxide signal. These data suggested oxygen was absorbed into the material and reacted with residual carbon to produce carbon dioxide[115].

The TG-MS plot for the titanium modified SMP-10 polymer (*Figure 4-5*) exhibited similar curves as in the neat polymer. The first onset occurred at 82.4°C was also attributed to water, again showing a low intensity signal throughout the heating of the polymer. A weight loss correlating to methane occurred earlier than in the un-doped polymer, but methane and ethane releases were also observed in the 500 °C temperature range, corresponding with mass decreases

at these same temperatures. No oxygen absorption was observed in the titanium containing polymer, nor was a significant carbon dioxide release consistent with oxygen reacting with carbon in the sample. This could be due to the titanium working as a carbon scavenger in the inert experimental environment, reacting with excess free carbon and preventing oxidation of the silicon carbide ceramic. The titanium-containing polymer also showed MS signals at m/z 27 and m/z 28, where the neat-polymer did not exhibit such signals. These signals were from various carbonaceous species like ethylene or vinyl radicals present from C=C double bonds in the polymer, suggesting the incorporation of titanium into the polymer may disrupt the original structure of the material, affecting not only its ceramic formation as demonstrated in the increased residual mass, but also in the modification of organic segments of the polymer, resulting in loss of different organic species than in the neat polymer.

4.5.3 X-Ray Diffraction

All reflections in the X-Ray diffraction pattern for Neat SMP-10 pyrolyzed to 1600°C were assigned to α-SiC in JCPDS DB Card No. 01-075-0254 and were summarized in the *Table 4-6*.

Table 4-6. JCPDS vs. Experimental Reflections for neat SMP-10 Ceramic (1600°C)

h k l	SiC 2θ	SiC I/I_0	Experimental 2θ	Experimental I/I_0
(1 1 1)	35.65	100	35.52	100
(2 0 0)	44.40	17	44.50	48
(2 2 0)	59.99	40	59.98	41
(3 1 1)	71.78	23	71.74	32
(2 2 2)	75.51	3.3	75.46	5.0

DB Card No. 01-075-0254

The diffraction pattern for the Ti-modified only ceramic (*Figure 4-7*) indicated no signs of other phases besides silicon carbide and the reflections are summarized in *Table 4-7*.

Table 4-7. JCPDS vs. Experimental Reflections for Ti-Modified SMP-10 Ceramic (1600°C)

h k l	SiC 2θ	SiC I/I_0	Experimental 2θ	Experimental I/I_0
(1 1 1)	35.65	100	35.74	100
(2 0 0)	44.40	17	44.26	8.5
(2 2 0)	59.99	40	60.04	49
(3 1 1)	71.78	23	72.00	44
(2 2 2)	75.51	3.3	75.56	12

DB Card No. 01-075-0254

The presence of only reflections that index to silicon carbide suggested that no crystalline titanium containing species were present in the polymer, despite evidence of polymer modification as confirmed by changes in the TG-MS data. Titanium was likely still present in the polymer in the form of amorphous titanium containing ceramics such as titanium dioxide or titanium carbide.

X-Ray diffraction patterns were initially obtained for the 10% titanium-modified SMP-10 heat treated in BCl_3, but several signals in the pattern were unresolved when initial reflection patterns were analyzed to produce more highly resolved signals for phase identification. A second sample, with 50% titanium modification was synthesized and heat treated in flowing boron trichloride using the same method as the 10% Ti sample. Diffraction patterns for this increased concentration sample provided improved resolution of the less intense signals that were previously difficult to resolve. *Table 4-3* showed nearly identical 2θ values between the two concentrations, with extra signals present for the 50%-Ti sample. The intensity of several of the signals are inverted between the two samples, suggestion a preferential orientation of the TiB_2 between the 10% and 50%-Ti-incorporated samples. XRD patterns for both samples showed crystalline phases of silicon carbide and titanium diboride. *Table 4-8* summarizes these reflection values and the planes and phases corresponding to DB Card No. 01-075-0254 for silicon carbide and *Table 4-9* summarizes DB Card No. 00-008-0121 for titanium diboride. All signals in both concentrations of titanium precursors were attributed to silicon carbide and titanium diboride, except for one broad reflection at approximately 27 2θ that indexed to

silicon dioxide from the glass sample slide. All reflections showed excellent agreement with JCPDS Card values. The diffraction pattern with labeled reflections is shown in *Figure 4-22*.

Tables 4-8 and 4-9 summarizes the reflection values and planes corresponding to ASTM Card No. 01-075-0254 (SiC) and ASTM Card No. 00-008-0121 (TiB_2).

Table 4-8. JCPDS vs. Experimental Reflections for SiC in 50% TiB-SMP-10 Ceramic (1600°C)

h k l	SiC 2θ	SiC I/I_0	Experimental 2θ	Experimental I/I_0
(1 1 1)	35.65	100	35.72	100
(2 0 0)	44.40	17	44.48	47
(2 2 0)	59.99	40	60.06	41
(3 1 1)	71.78	23	71.82	32
(2 2 2)	75.51	3.3	75.64	4.9

DB Card No. 01-075-0254

Table 4-9. JCPDS vs. Experimental Reflections for TiB_2 in Polymer Derived Ceramic

	TiB_2		Experimental	
(h k l)	2θ	I/I_0	2θ	I/I_0
(0 0 1)	27.68	20	27.62	35
(1 0 0)	34.20	60	34.20	70
(1 0 1)	41.46	100	41.50	100
(0 0 2)	57.05	14	56.94	9.4
(1 1 0)	61.16	20	61.18	28
(1 0 2)	68.20	16	68.34	16
(2 0 1)	78.69	14	78.66	12

DB Card No. 00-008-0121

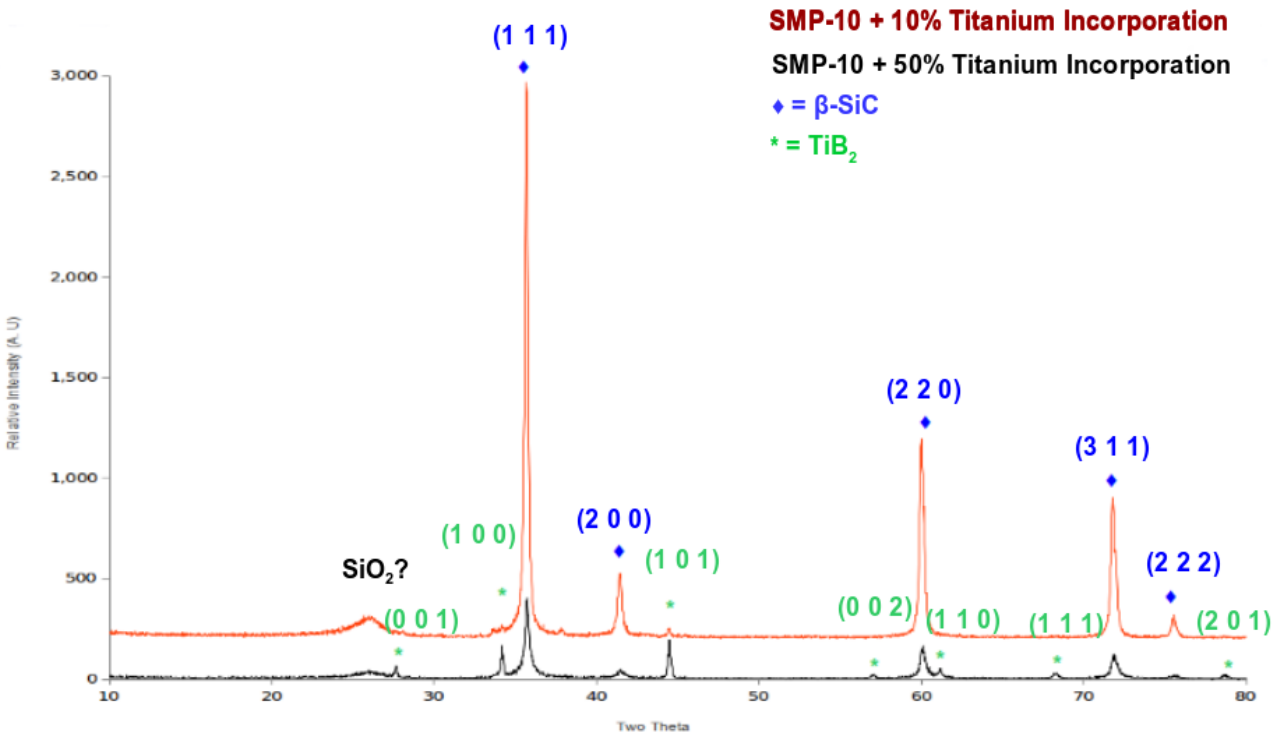

Figure 4-22. XRD Pattern of Ceramic Resulting from SMP-10 Modified with 10% and 50% Titanium Isopropoxide Incorporation Heat Treated in BCl_3

Heat treatment studies were performed to determine the effect of temperature at the pre-ceramic sample was exposed to boron trichloride gas. Boron trichloride had proven difficult to work with and required special safety handling, so reducing both the amount used and the temperature at which flowing boron trichloride was used as was very important. Initially, samples were heat treated in BCl_3 from room temperature to 1600˚C. Further studies exposed the samples to BCl_3 at lower temperatures and for smaller temperature ranges and less time. These samples were still heated to 1600˚C in argon after BCl_3 exposure. These results (*Figure 4-23*) showed only signals indexed to TiB_2 and SiC, nearly identical to those in *Figure 4-22*. *Figure 4-23* also demonstrated that boron incorporation at a lower temperature (500˚C-800˚C) resulted in the most crystalline titanium diboride and silicon carbide.

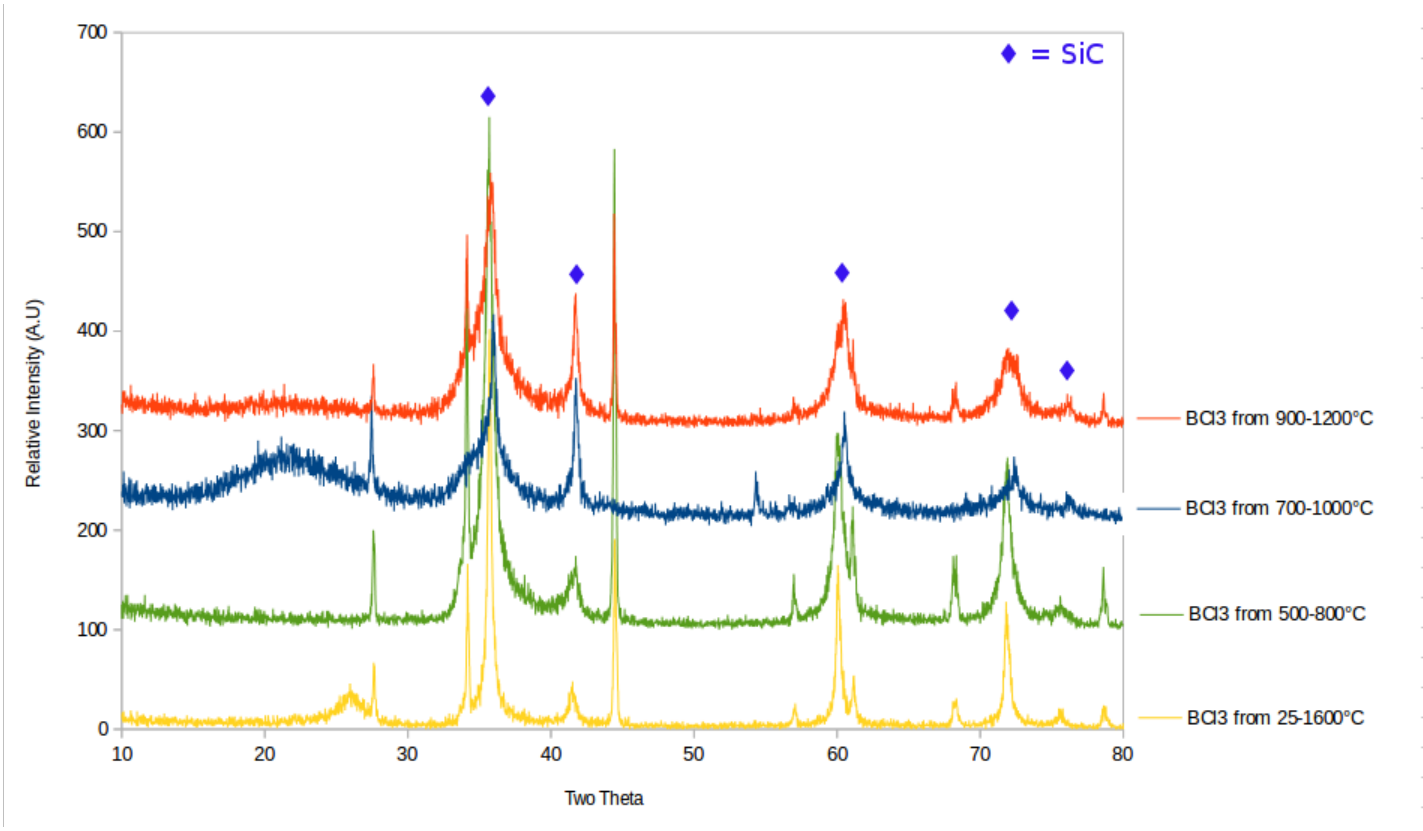

Figure 4-23 XRD Patterns of Temperature Studies for BCl_3 Exposure of Ti-Incorporated SMP-10

Boron trichloride exposure at higher temperatures (700˚C-1000˚C and 900˚C-1200˚C) still resulted in titanium diboride formation, though a decrease in crystallinity was observed. These data indicated that incorporation of boron into the material could occur at lower temperatures and was not necessary for the entirety of the 1600˚C heating. These data also suggest that titanium diboride played a critical role in the inhibition of larger, crystalline grain formation of silicon carbide. Both silicon carbide and titanium diboride signals appeared broader, indicating nano-crystallinity in both material phases as compared to the sharp signals observed in the materials that had been exposed to BCl_3 throughout the entire heating process. These diffraction patterns were indexed to silicon carbide and titanium diboride, and the signals for silicon carbide were noted in the diagram, while all other signals correlated to titanium diboride but marker symbols were omitted for clarity.

4.5.4 Scanning Electron Microscopy

Scanning Electron Microscopy images showed a similarity in bulk structure between the ceramic pyrolysis product of neat SMP-10 and Ti-containing SMP-10, both heated to 1600°C under argon. The sharp and angled edges were expected from a ceramic and both samples exhibited similar bulk characteristic in shape. The sizes of the particles in the SMP-10 were in the hundreds of micron range, while the Ti-modified SMP-10 had slightly smaller grain sizes, in the 20-100 micron size range. This may have been attributed to the sample preparation through grinding in a mortar and pestle. The sizes of particles were not significantly different between the Neat and Ti-modified polymers. The TiB_2-modified SMP-10 appeared very different in both size, shape, and morphology. These particles were much smaller, in the 1-5 micron range, and were arranged in uniform clusters, despite also being ground in a mortar and pestle. The individual grains were polyhedra shaped and appeared slightly rounded and very regular as compared to the irregular, jagged grains in the other two samples. This result supported the idea of grain-growth inhibition of silicon carbide caused by the introduction of titanium diboride dopants.

4.5.5 Energy Dispersive X-Ray Spectroscopy

EDS was used to determine the elemental composition of the ceramic materials and how they different with the addition of titanium and boron. All three samples showed evidence of silicon, carbon, and the EDS weight percent values of elements were summarized in *Table 4-10*.

Table 4-10. EDS Weight Percents for Neat SMP-10, Ti-SMP-10 and TiB-SMP-10

	Wt% C	WT% Si	WT% O	Wt% Ti	Wt% B	Wt%Cl
Neat SMP-10	55.6	41.6	2.8	-	-	-
Ti - SMP-10	38.1	40.4	18.1	3.2	-	0.2
TiB- SMP-10	31.4	31.1	-	0.1	37.4	-

- = Not Detected

Neat SMP-10 contained more carbon than silicon, as expected for the slightly-carbon rich silicon carbide ceramic which SMP-10 is known to produce. The concentration of oxygen was relatively low, also as expected in this type of material. The elemental mapping showed an even distribution of carbon and silicon, as well as oxygen, which was not show for clarity. This was as expected for a polymer which forms silicon carbide upon pyrolysis.

The titanium-incorporated SMP-10 showed near-stoichiometric silicon and carbon concentrations and a significantly higher concentration of oxygen. This result was likely due to the oxygen scavenging nature of titanium[116]. The state of the titanium was unknown, but during the heating process was expected to pick up oxygen from both the titanium isopropoxide precursor as well as the atmosphere, accounting for the increase in weight percent of oxygen. Chlorine was present in the elemental composition, though the concentration was so low that it could be in the margin of error, or residual chlorine present from the SMP-10, which uses chlorinated precursors to form the polymer. The 3.2 wt% titanium was within the range of error for the initial 10% wt percent titanium isopropoxide used in this polymer modification and this method of analysis was used to confirm the presence of titanium as opposed to attempting to quantify it. Elemental mapping showed an even distribution of silicon, carbon, and titanium, as expected from the corresponding micrographs showing similar morphology as the Neat SMP-10. The ceramic was likely composed of silicon carbide with evenly distributed titanium throughout the ceramic. Titanium or titanium species were not observed in the X-Ray diffraction data due to the titanium species being non-crystalline, and EDS was used

to confirm the presence of titanium in the ceramic in the titanium-only modified polymer, despite this only being a middle step in the SiC/TiB_2 ceramic formation process.

The titanium and boron modified SMP-10 polymer contained silicon, carbon, titanium, and boron. This supported the XRD pattern showing only silicon carbide and titanium diboride. The weight percent of silicon and carbon were relatively close, however the value of boron is much higher than expected for a sample that contained only 10 wt% titanium isopropoxide. This high value could be due to the low molecular weight of boron and the limitations in measuring capabilities of the instrument for boron, as well as the instrument adjusting calculations to ensure calculated values added up to 100%. The concentration of titanium was also quite low (3.2 Wt %), but also within the error of the analysis method. More importantly, the elemental mapping provided interesting data, showing a direct correlation of silicon and carbon in the sample, as well as a separate but direct correlation of titanium and boron together. This suggested that the ceramic was comprised of both silicon carbide and titanium diboride in separate grains. This also helped to explain the grain growth inhibition phenomenon observed in the micrographs, in which the presence of titanium diboride inhibits the grain growth in silicon carbide formation, producing smaller grains of silicon carbide and the potential for increased strength properties.

4.5.6 Mechanical Testing

Composites were fabricated according to the conditions described in **Section 4.2.2** and both the Neat SMP-10 composite and the SMP-10 TiB_2 composite reached a density plateau after seven impregnation cycles. The density of bulk silicon carbide is 3.21 g/cm^3 and the maximum density of the neat SMP-10 CMC was 2.05 g/cm^3. This decrease in density is accounted for through the porosity in the voids both between the individual fibers, as well as voids between the layers of fabric plies. The composite also contained a coating of

boron nitride (Density = 2.1 g/cm^3), which could have a minor effect on reducing the density of the composite overall as compared to bulk silicon carbide.

The SMP-10 TiB_2 CMC reached a density plateau at 1.84 g/cm^3, slightly less than that of the neat CMC. This was likely due to fabrication issues, as discussed in **Section 4.4**. The density of bulk titanium diboride was 4.52 g/cm^3, though the 5 wt% titanium isopropoxide addition would result in a TiB_2 concentration in the 1-3% range and would have a small effect on the overall density of the composite, as would the thin coating of boron nitride applied as an interface material.

The average maximum flexural stresses for the SMP-10 CMC and the TiB_2 CMC were 14.66 ± 2.15 KSI and 15.20 ± 1.28 KSI respectively. The ultimate values were relatively similar, with the TiB_2 CMC having a 3.62% greater strength than the neat composite. Despite this numerical value, the measured KSI strengths lie within the same margins of error, making it difficult to describe the modified compote as stronger. Another consideration was the processing issues experienced during the fabrication of the TiB_2 CMC and the lower density. This lower density was indicative of greater porosity, more void space, and higher expectation of defects in the composite. Original expectation from this result was that the ultimate flexural stress of the composite would suffer as a result of this low density. This was not the case, suggesting that despite the lower density, the modified CMC had no appreciable decrease in strength than the neat SMP-10 CMC.

During the three-point bend testing, the TiB_2 CMCs appeared to fracture differently than the SMP-10 CMCs. The neat polymer based composites broke clean through, producing two separate pieces across a fracture point. The TiB_2 modified CMC did not fracture all the way through, instead leaving one piece of material held together by pieces of fiber and matrix. The bulk of the material had broken, but the composite showed excellent strengthening mechanisms, resulting in energy dispersion throughout the material and an increased flexural stress experienced before mechanical failure. The addition of TiB_2 into the polymer and the

reduced grain size of the silicon carbide resulted in increased strength properties, obtaining the goal of the heteroatom additions into the polymer.

4.6 Conclusions

Titanium and boron heteroatoms were incorporated into a silicon and carbon based pre-ceramic polymer, resulting in the production of a ceramic containing both silicon carbide and titanium diboride when the polymer was pyrolyzed. The polymer was characterized extensively, showing distinct phases of silicon carbide and titanium diboride, as well as a clear sensitivity of grain size and shape of the resulting ceramic with the addition of the titanium and boron containing precursors. Temperature was determined to have a distinct effect on the resulting crystallinity of the ceramic produced, which will be important in the variety of uses of the newly designed polymer. Applications like ceramic fibers require nano-crystalline to amorphous ceramics to maintain flexibility in processing applications, while matrix materials are generally more crystalline. The amount of TiB_2 incorporation, as well as the temperature of heat treatment can be varied to modify the degree of crystallinty and general properties of the ceramic.

The future of this material lies in a variety of applications for use in CMCs and similar composite materials. The polymer showed promising results as a matrix material in a PIP composite, providing excellent strength properties as compared to a CMC using undoped polymer (14.66 ± 2.15 KSI for the neat SMP-10 CMC and 15.20 ± 1.28 KSI for the TiB_2-Modified CMC), a 3.62% greater strength in the TiB_2 composite despite a lower density and greater porosity in the fabricated CMC. This value, though not a significant increase considering the margin of error, shows there was comparable strength in the modified composite and it showed promising results for future research. A major goal of this work was to produce a material with greater strength properties than silicon carbide alone, and the CMC produced met this expectation.

Chapter 5 Development and Fabrication of Multi-Layer Magnetic Composite

5.1 Introduction

Ceramic matrix composites have been a popular technology for use in high temperature applications due to their high strength and thermal properties. Recent advancements in these materials have expanded the properties of these systems to include specialty properties including magnetism. The incorporation of magnetic material into a CMC provides a variety of new applications for use in the aviation and aerospace industries, providing unique properties in military applications by taking advantage of the inherent properties of magnetic materials[117,118]. Other advanced applications include magnetic sensors for use in high temperature and oxidizing environments and use of the magnetic material coated substrate in spray-on paints or adhesives[119,120]. These magnetic composites may also be used as information storage devices, as well as pathways for synthetic intermediates to make a variety of composite-like materials[121].

Current technologies to incorporate magnetic materials into CMCs use solid metal magnetic components added as filler to PIP composites or thick coatings applied using electroless deposition or physical vapor deposition[122]. In these PIP composites, fine particles of magnetic metals are added as filler instead of the fine ceramic particles typically used in this fabrication process[123]. The resulting magnetic composites are heavy due to the added mass of metal filler and have no means of preventing the oxidation of the metals and are for use at room temperature or low temperatures only. Magnetic metals like cobalt, iron, and nickel are prone to oxidation and oxidize readily at temperatures ranging from room temperature to 500°C[124, 125, 126] and composite systems designed with magnetic filler are no exception from this oxidation and the loss of magnetic properties. With this in mind, the composite system in this section was designed with high temperature use in mind and was assembled with a

oxidation resistant coating that was applied to the magnetic material, resulting in protection of the metal and preservation of both the magnetic properties and the composite strength during exposure to heat and oxidation.

The composite was initially designed with the incorporation of magnetic filler for PIP composites using hollow mullite spheres as the coated substrate. These spheres, branded cenospheres, were small, uniform, hollow spheres filled with inert gas, produced as a byproduct of coal combustion[127]. This substrate was extremely inexpensive, easy to coat with magnetic metals and effectively reduced the mass by only using a thin film of magnetic material as opposed to fine metal particles used as filler. Use in aircraft or aerospace applications, density was of importance in the final fabricated composite to ensure the weight of the vehicle was low enough to fly efficiently.

With this in consideration, a second system was designed building off this concept. A CVI composite in which ceramic fibers were directly coated with magnetic material was also fabricated, effectively keeping the mass low due to the thin coating of magnetic material as opposed to magnetic filler particles. The ceramic fibers were coated with an interface (see **Section 2.2.2**) before being coated with magnetic metal to ensure strength was preserved as the coatings were applied to the fibers.

Another consideration in the design of this composite was a means to protect the magnetic metal from oxidation during both processing and throughout application. This allowed the materials to be used in high temperature, oxidizing environments like those seen in aviation[128]. Without the protective coating, the metals oxidize at high temperatures, losing their magnetic properties. Initial thoughts were to use CVI silicon carbide to protect the metal from oxidation and provide a matrix for the composite, but it was determined that in the case of cobalt, the metal of focus for this section, reactions occurred during the coating process that destroyed the magnetic properties of the metal. To overcome this issue, a flash coating of CVD silicon dioxide was deposited over the cobalt metal, followed by the application of a CVI silicon

carbide matrix. This method preserved the magnetism of the metal, as well as completing the composite.

The composite was designed to incorporate a ferromagnetic metal into the CMC in a multilayer system. The coatings could be applied as either a single layer of magnetic material and protective coating, or as multiple iterations of magnetic and protective coatings, as shown in *Figure 5-1*.

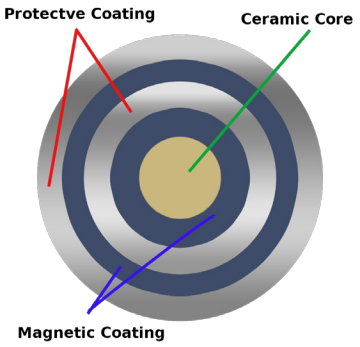

Figure 5-1. Diagram of the Multi-Layered Coating Magnetic System

The magnetic material and protective coating could be applied to continuous fibers, fiber whiskers, or cenospheres, depending on the desired application. Initial studies were performed to coat cobalt, nickel, and iron onto the substrates, but it was determined that the most efficient metal for these coatings was cobalt. The proposed uses for the material was for both as a lightweight filler in PIP composites, as well as a fiber coating in CVI CMCs, and both fillers and coated fibers were fabricated. The best results were achieved with the cobalt applied to interface-coated CG-Nicalon® fibers, and further studies including tensile strength, magnetism, and oxidation studies were performed on this system.

The multilayer magnetic CMC provided a new system combining the strength and oxidation properties of traditional CMCs with the added benefit of magnetism for advanced applications. These new materials were capable of subjection to high temperature oxidations while maintaining magnetic properties. The process was designed to be inexpensive and have a

wide range of possible variations in both metal and substrates. The ability to use these materials under various environments was also an advantage of this system.

5.2 Experimental

Experiments were performed with varying conditions for the application of a magnetic material and a protective coating. Typical experiments for these processes were carried out as follows:

5.2.1 Magnetic Material: Cobalt Reduction

A 1.0 M solution of cobalt nitrate was made by dissolving 29.57 g of $Co(NO_3)_2 \cdot 6H_2O$ (Mallinckrodt) in 100 mL DI water. CG-Nicalon® fiber tow coated with CVD BN/SiC (**Section 2.2.2**) was added to a tray containing the cobalt solution and submerged entirely. The wetted fiber was then transferred to a ceramic boat and dried in a drying oven at 100°C. The resulting material was then reduced under hydrogen in a 1" quartz tube in a tube furnace to form the metallic coating. Hydrogen reductions were carried out at atmospheric pressure using UHP hydrogen at a flow rate of 150 sccm with a ramp rate of 1°C/min to 350°C. The reduction was performed for 16 hrs, producing a highly magnetic coating. Similar procedures were carried out on various ceramic substrates, including cenospheres Brand P-Lite 150F™ hollow spheres (for future use in PIP Composites), continuous fibers, whiskers, and woven fabric. The fibers used were either non-oxide based ceramic cloth like Nicalon® or oxide based cloth like Nextel™.

5.2.2 Deposition of Protective Coatings

5.2.2.1 Silicon Dioxide

Silicon dioxide coatings were deposited using a CVD process, both at atmospheric and low pressures. These coatings were all deposited by the thermal decomposition of tetraethylorthosilicate (TEOS) in the presence of either nitrogen, argon, or hydrogen. The reactor shown in *Figure 5-2* consisted of a tube furnace, a bubbler, mass flow controllers to control the flow of the gases, and a vacuum pump and throttling valve to control the pressure. The deposition temperature was varied from 500˚C to 700˚C with 700˚C producing the best overall coating. To deposit the SiO_2 coatings, either UHP nitrogen, argon, or hydrogen was bubbled through TEOS (Gelest, Inc.) at a flow rate of 400 sccm for 0.5 to 1 hr depending on the desired thickness of the coating. This process was performed at either reduced or atmospheric pressure. For the low pressure runs the pressure was held constant at one Torr. Once the temperature had stabilized, flow was redirected through a bubbler filled with TEOS and the flow adjusted to 400 sccm for the desired time.

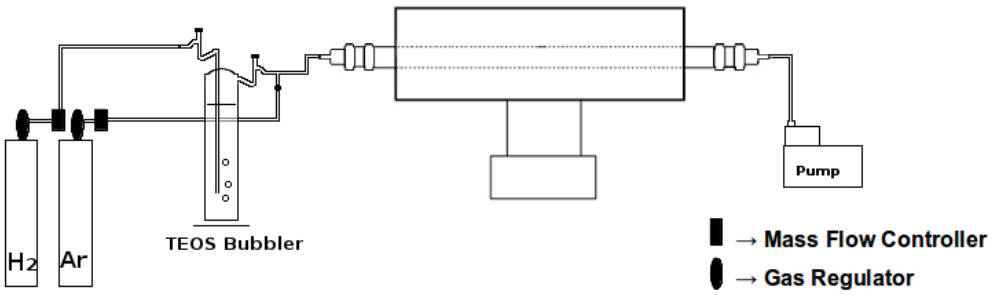

Figure 5-2. Experimental set-up used to deposit SiO_2 on Cenospheres and Ceramic Fabric

5.2.2.2 Silicon Carbide

For silicon carbide protective coatings, a flash coating of silicon dioxide was first deposited. (30 minutes under the conditions listed in **Section 5.2.3**) The silicon carbide was then deposited

using CVI of methyltrichlorosilane (MTS, Gelest, Inc.) in a reactor similar to the one above. The reactor (*Figure 5-3.*) was heated to 1050°C under argon, and silicon carbide was deposited by bubbling hydrogen through MTS at 0.150 sccm for 2 hours. The reactor was cooled under flowing argon.

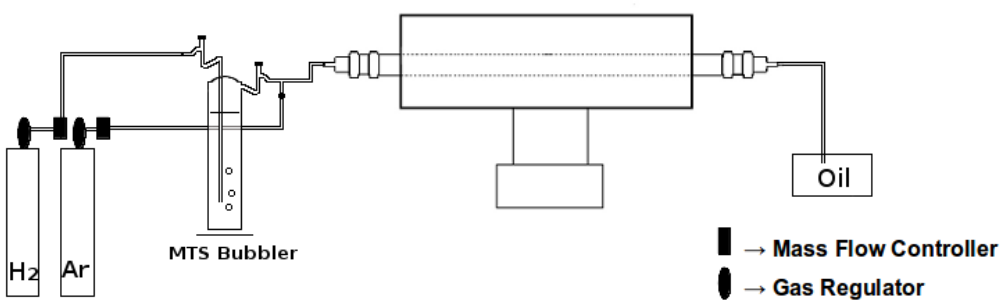

Figure 5-3. Reactor Diagram for Silicon Carbide Deposition

The same procedures were applied to continuous fiber and fiber whiskers (CG-Nicalon®, Nextel™ 440) for use in a PIP Composite. Iterations of each coating were produced if a multi-layered system was desired.

5.2.3 Fabrication of Magnetic Composites

A typical Magnetic Single Strand composite (Mini-C) was fabricated as follows:

Single strand unidirectional composites were fabricated by first coating CG-Nicalon® fibers with a boron nitride and silicon carbide interface using the method described in **Section 2.2.2**. The interfacial material was used to provide the correct bonding/debonding properties in a ceramic matrix composite. The multi-layered magnetic component was applied using the method described in **Section 5.2.1** to deposit cobalt metal over the interface-coated fiber, followed by a coating of CVD SiO_2 (**Section 5.2.2.1**) This multi-layer material was then placed inside a quartz tube for SiC infiltration. Silicon carbide was infiltrated into the tow by reacting hydrogen with methyltrichlorosilane at 1050-1100°C for 4-6 hours. These Mini-Cs

were tested for magnetic properties with a handheld magnet to determine if they would adhere to a permanent magnet or not.

5.2.4 Oxidation of Magnetic Composites

The CN-Nicalon®/BN/SiC/Co/SiO_2/SiC composites were oxidized to determine the effect of oxidation on both the magnetic properties and the tensile strength of the material. These materials were heated to 800°C in flowing air for 36 hours and cooled to room temperature before characterization.

5.3 Characterization

All materials and coatings were examined for crystalline phases using X-Ray Diffraction patterns obtained using a Rigaku Ultima IV X-Ray Diffractometer with a Cu Kα X-Ray source with a beam voltage of 44 kV and 40 mA beam current. Scans were performed from 10 to 80° with a scan rate of 2.0°/min. X-Ray diffraction patterns and phases were verified by JCPDS and Rigaku RINT2200 XG Software.

All materials and coatings were characterized using either a FEI Nova NanoSEM 450 Scanning Electron Microscope with a Everhart-Thornley Detector and with X-Max 80 Silicon Drift Detectory or a Zeiss DSM 982 Gemini FE-SEM with a Schotty Emitter with a voltage range of between 2.00 to 4.00 kV and a beam current of 1 -2 mA. Coating thicknesses and coating adhesion were investigated using SEM .

Energy-Dispersive X-Ray Spectroscopy was performed using an Oxford Instruments EDS with Aztec Instruments Nanotechnology Microanalysis System. Map scans were performed at a working distance of 5.3 mm with a Process Time of 4 and High Voltage at 0.2 kV.

Select materials were tested for magnetic properties using a Quantum Design MPMS SQUID (Superconducting Quantum Interference Device) Magnetic Property Measurement

System to determine the effect of coating application and oxidation on the magnetic properties of the materials. The samples were analyzed for the long moment (emu) over a magnetic field between -60000 and +60000 Oe with a DC scan at a temperature of 300 K. The plots were corrected for the mass of the cup and cotton used for sample loading and the mass of the sample was used to determine the magnetic moment in emu per gram.

Tensile testing of the fibers was performed using an Instron 5869 Testing Machine with mechanical clamps and a ±50 kN load cell. Tensile extension was performed at 0.2000 inches per minute. Tensile strength was determined before and after oxidation to determine the effect of strength on magnetic composites with and without protective coatings. Tows were affixed to card-stock tabs illustrated in *Figure 5-4* and acrylic binder was applied to the composites prior to testing to ensure uniform breakage of the tow during testing.

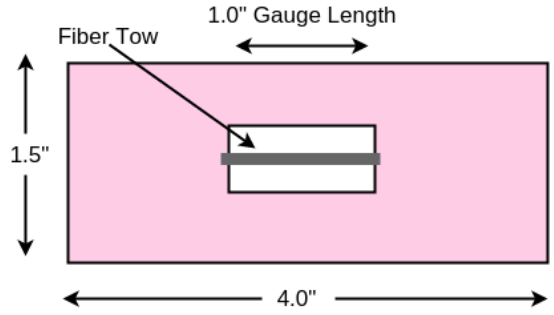

Figure 5-4. Cardstock Mounting Setup for Fiber Tow Tensile Testing

Testing was performed on multiple composites and an average was taken. Ultimate tensile strengths in KSI were calculated using the cross-sectional area assumed with a single tow containing 500 filaments at a fiber diameter of 14μm.

5.4 Results

During the reduction of cobalt nitrate on ceramic substrates, a visual color change occurred, beginning with a pink solution and ending with a grey, solid powder after the hydrogen heat treatment, shown in *Figures 5-5 and 5-6* This color change was indicative of the reduction of

the nitrate groups and the formation of cobalt metal. The resulting powder was also determined to be magnetic.

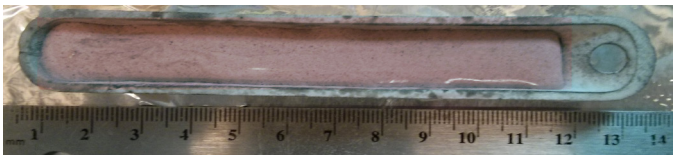

Figure 5-5. Cenospheres and $Co(NO_3)_2$ Before Hydrogen Reduction

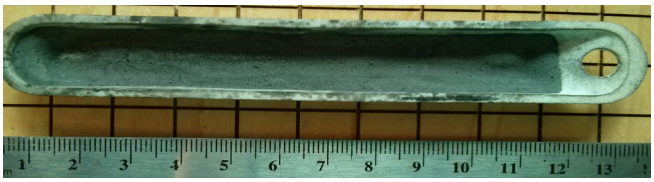

Figure 5-6. Cenospheres with Cobalt Metal After Hydrogen Reduction

Tests of magnetism were performed periodically with a hand-held magnet, allowing confirmation of magnetism prior to analysis with other methods. This bulk characterization method allowed for an immediate determination of the magnetic nature of the materials without waiting for more complicated characterization methods.

5.4.1 X-Ray Diffraction

Cenospheres were characterized using XRD to determine the crystalline phases present in the material. The diffraction pattern is shown in *Figure 5-7*, below, and reflections are summarized in and indexed in **Section 5.5.2**, *Table 5-2*.

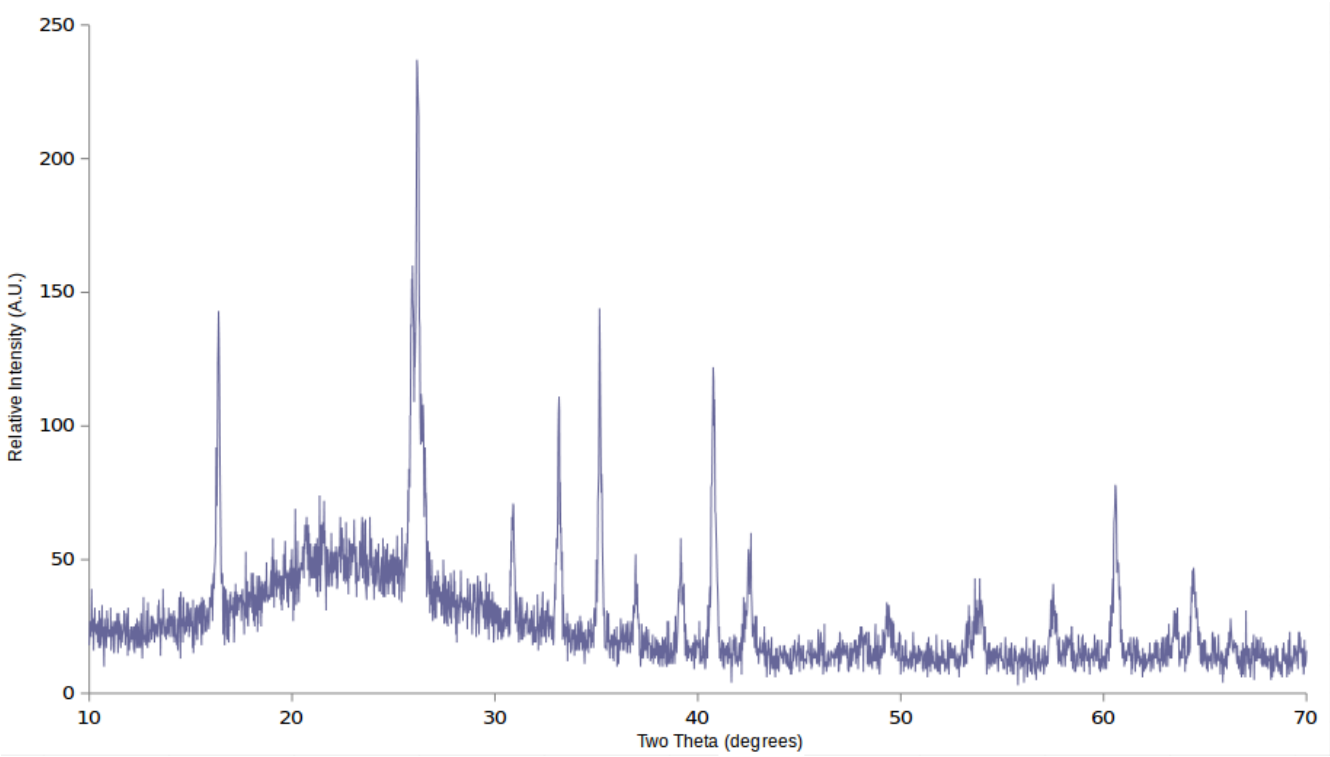

Figure 5-7. XRD Pattern of As-Received Cenospheres

The diffraction pattern showed primarily sharp, resolved signals, with one broadened signal near 27 2θ. The pattern had some noise, as expected for the rounded, fine grain spheres.

A diffraction pattern was also obtained for the cobalt coated ceramic spheres. This diffraction pattern, shown in *Figure 5-8*, also showed relatively sharp signals with the same broadened signal as in *Figure 5-7*. The reflections are summarized and indexed in **Section 5.5.2**.

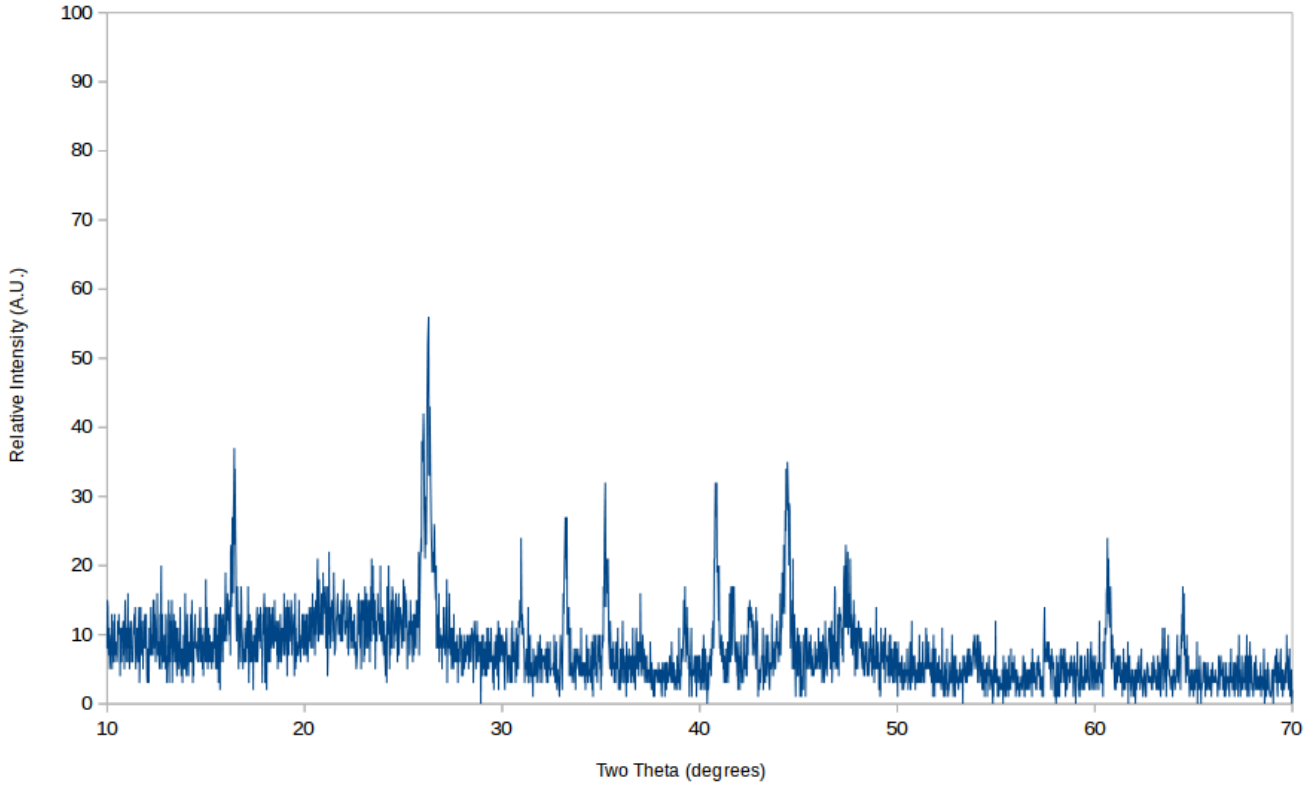

Figure 5-8. XRD Pattern of Cobalt Coated Cenospheres

5.4.2 Scanning Electron Microscopy

Micrographs were obtained for all materials to observe the bulk morphology and uniformity of the coating. Uncoated cenospheres were examined for the their shape, size, and surface properties. Micrographs of the uncoated cenospheres are shown in *Figure 5-9*.

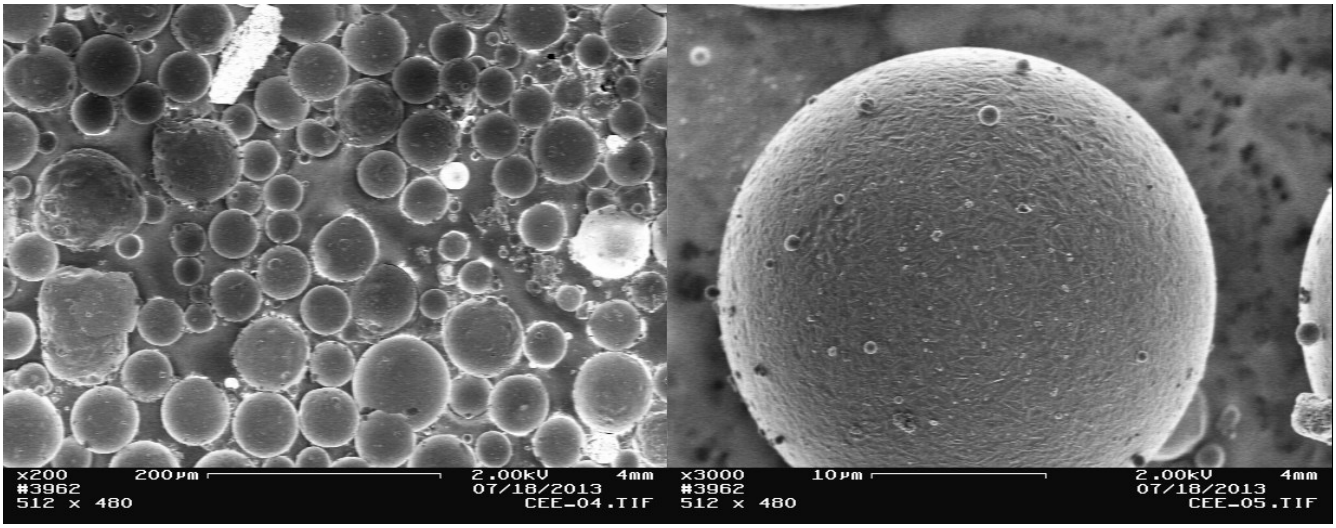

Figure 5-9. Micrographs of Uncoated Cenospheres

The cenosphere substrate showed smooth, uniform spheres in the nanometer to micron size range. These spheres were typically intact, with very little breakage or with significant size or texture outliers.

Cenospheres coated with cobalt using the hydroxyl reduction method were examined using SEM to determine the uniformity of the coating and the morphology of the cobalt particles deposited. A micrograph of the cobalt coated cenospheres is shown in *Figure 5-10*.

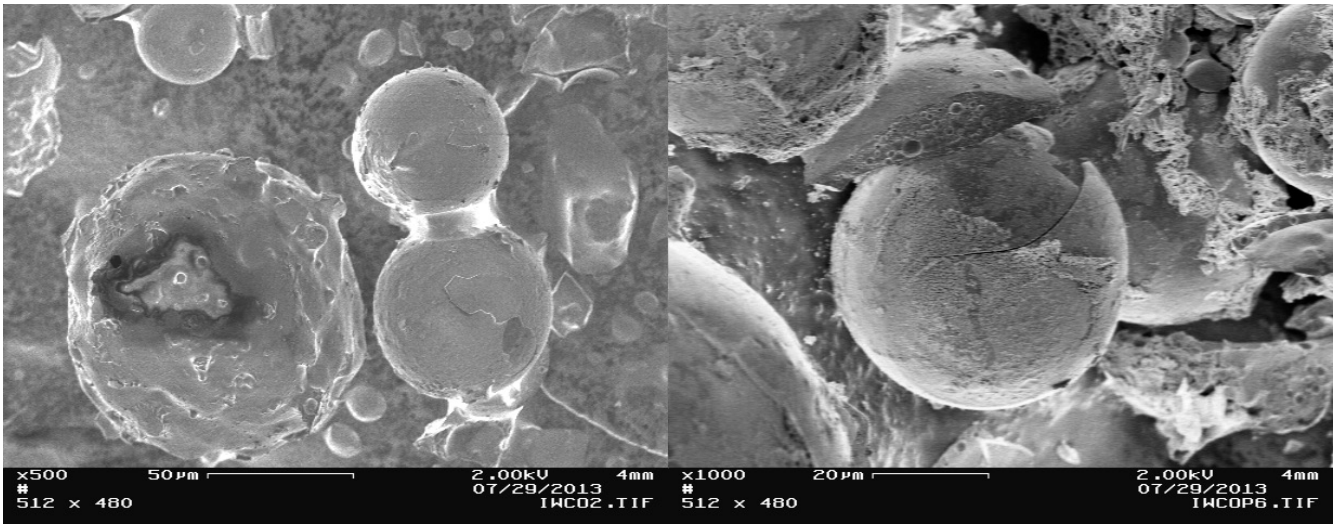

Figure 5-10. Micrograph of Cobalt Deposited on Cenospheres

The cobalt coating was relatively uniform and showed flaking from the ceramic sphere substrate. Areas with increased flaking were the focus for images because areas where the coatings were intact on the spheres gave no detail of depth perception or visual information about the coating. The cobalt showed cluster-like morphology and relatively good overall coating areas. Some cenospheres showed bare spots and there was accumulation on excess cobalt that was not adhered to the ceramic. Overall, the coating was acceptable and the majority of spheres were coated in entirety. CG-Nicalon® BN/SiC fibers were also coated with cobalt metal using the described method and the micrographs are shown in *Figure 5-11*.

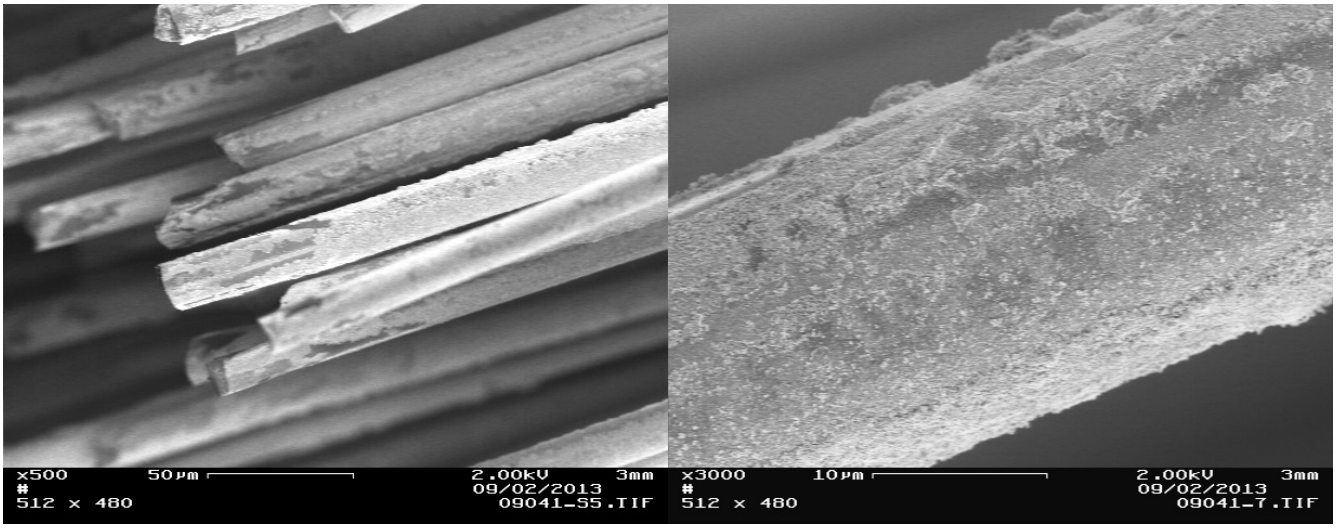

Figure 5-11. Micrographs of Cobalt Deposited on CG Nicalon® BN/SiC Fiber

The coating appeared to have a similar cluster like morphology as the coating on the cenospheres. The fiber was coated relatively uniformly, however there were some bare spots where the fiber had been cut on the ends during sample preparation. The coating was slightly clumpy but overall the fiber was fully coated.

CVI composites were fabricated by depositing an interface using CVD, followed by the application of the magnetic material, a coating of CVD SiO_2, and finally the deposition of the protective silicon carbide coating over the magnetic component. This composite was fabricated using CG-Nicalon® fibers with a boron nitride and silicon carbide duplex interface, cobalt, a CVD silicon dioxide coating, and a CVD silicon carbide coating. Micrographs of the composite before the SiC infiltration are shown in *Figure 5-12*.

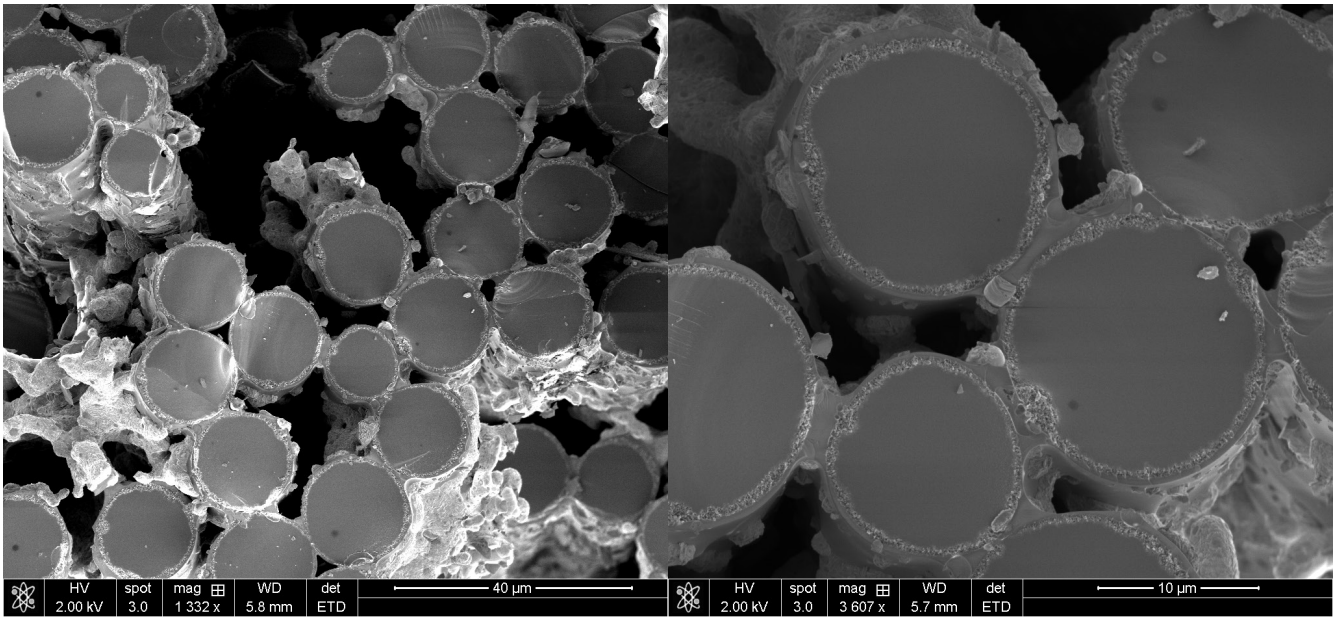

Figure 5-12. CG-Nicalon® Fiber Coated with a BN-SiC Interface with a Cobalt Coating and CVD SiO_2 Protective Layer

These micrographs show the fiber and interface, along with a clear distinct ring of cobalt metal. The cobalt showed much larger grain size than the other coatings, appearing as a grainy, slightly porous ring around the fiber. The coating appeared to have good adhesion, showing no flaking or separation from the fiber. The SiO_2 coating over the cobalt also showed excellent uniformity and adhesion. The material exhibited significant porosity between the fibers but not between the coatings, which was expected for the quick flash coating of SiO_2 that was deposited over the cobalt. These gaps were left intentionally so the composite could be infiltrated with silicon carbide.

The micrograph of the completed composite, after the silicon carbide infiltration (CG-Nicalon® BN/SiC/Co/SiO_2/SiC) is shown in *Figure 5-13*. The image was taken using the CBS Detector and the bright spots correlate to cobalt distributed throughout the sample and no longer in tight rings like in the previous micrographs.

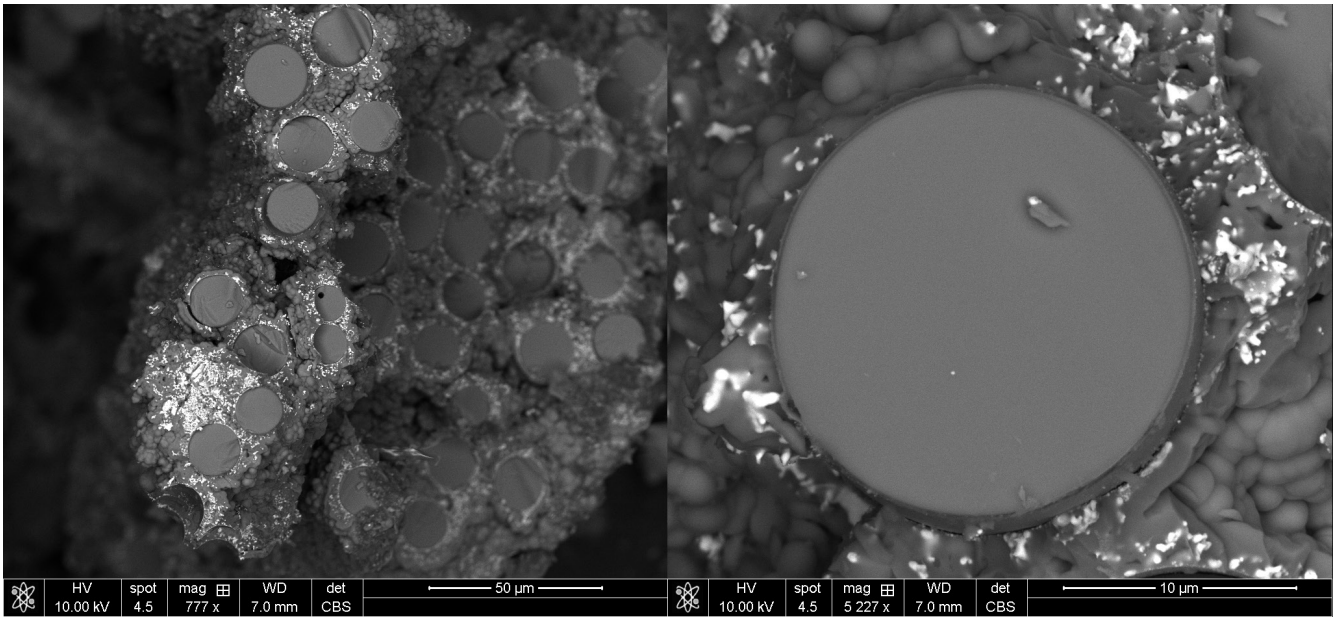

Figure 5-13. Mini-C Fabricated from CG-Nicalon® Fiber Coated with a BN-SiC Interface with a Cobalt Coating and CVD SiO_2 / SiC Protective Layer (CBS Detector)

These micrographs clearly showed the fiber with the duplex interface applied. Areas of silicon carbide and silicon dioxide are also clearly defined the in the left image, where two thicker rings of bulk material are observed. The cobalt, indicated by the bright spots, was distributed throughout the silicon dioxide and silicon carbide layers and appears to have migrated from the original area at which is was deposited.

5.4.3 Energy Dispersive X-Ray Spectroscopy

Samples of the completed composite were analyzed using EDS to determine the elemental distribution. This method was only used to yield data about the elemental mapping in the sample, and not for quantitative purposes. *Figures 5-14 and 5-15* show the electron image and the elemental mapping for carbon, oxygen, silicon, and cobalt in the completed composite.

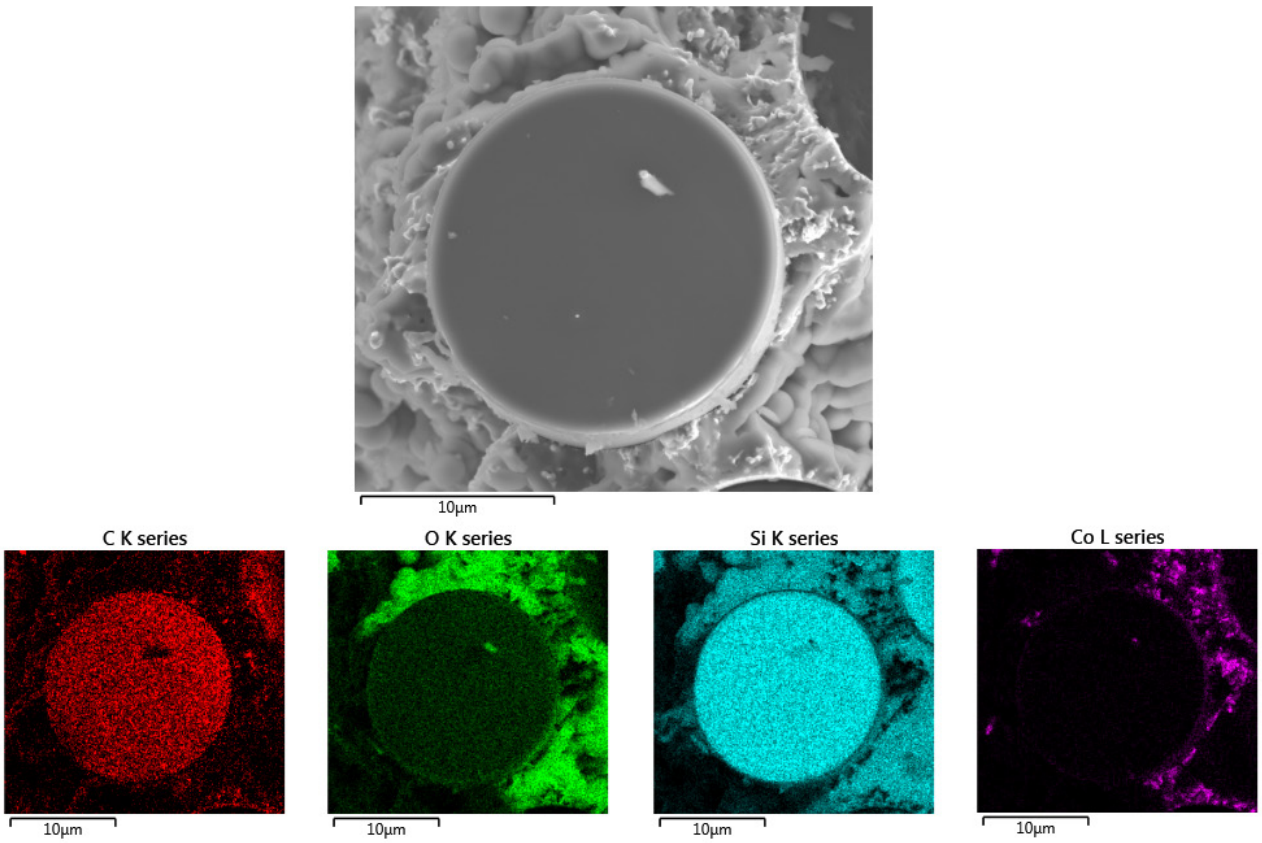

Figure 5-14. Electron Image and EDS Elemental Mapping of Cobalt CMC

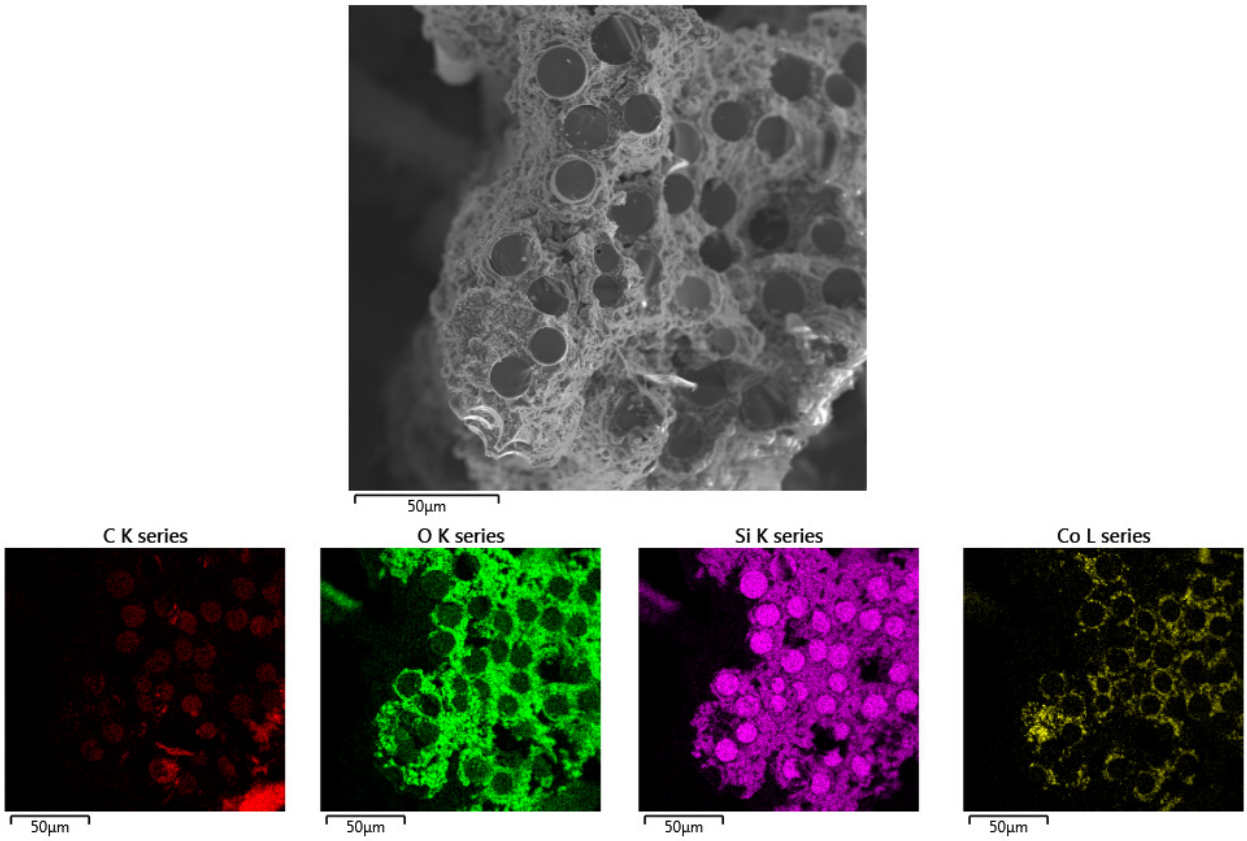

Figure 5-15. Electron Image and EDS Elemental Mapping of Bulk of Cobalt CMC

The elemental mapping showed the presence of carbon in both the carbon and the coatings around the fiber, while silicon was distributed across nearly the entire composite. Cobalt was shown the be primarily located around the perimeter of the fibers, however some migration into the matrix was observed. Oxygen appeared to be located primarily in the matrix material, though mapping showed evidence of oxygen detected in the fiber, as well as in the cobalt coating.

5.4.4 Supercondicting Quantum Interference Device (SQUID) Magnetic Measurements

Magnetic measurements were obtained for the composite in various states of fabrication, as well as for pure cobalt metal to compare as a standard. The values of magnetic moment, expressed in emu per gram, were only used for samples which achieved magnetic saturation and ferromagnetic character. Magnetic saturation was confirmed where the slopes of the Sigmoid plot ends were parallel to the axis with no slope. The plots for the CG-Nicalon® BN/SiC/Co with CVI SiC, as well as the composite with no protective coating after oxidation treatment both had sloping ends of the curve and therefore had no ferromagnetic properties. The plot for the samples showing ferromagnetism is shown in *Figure 4-16*.

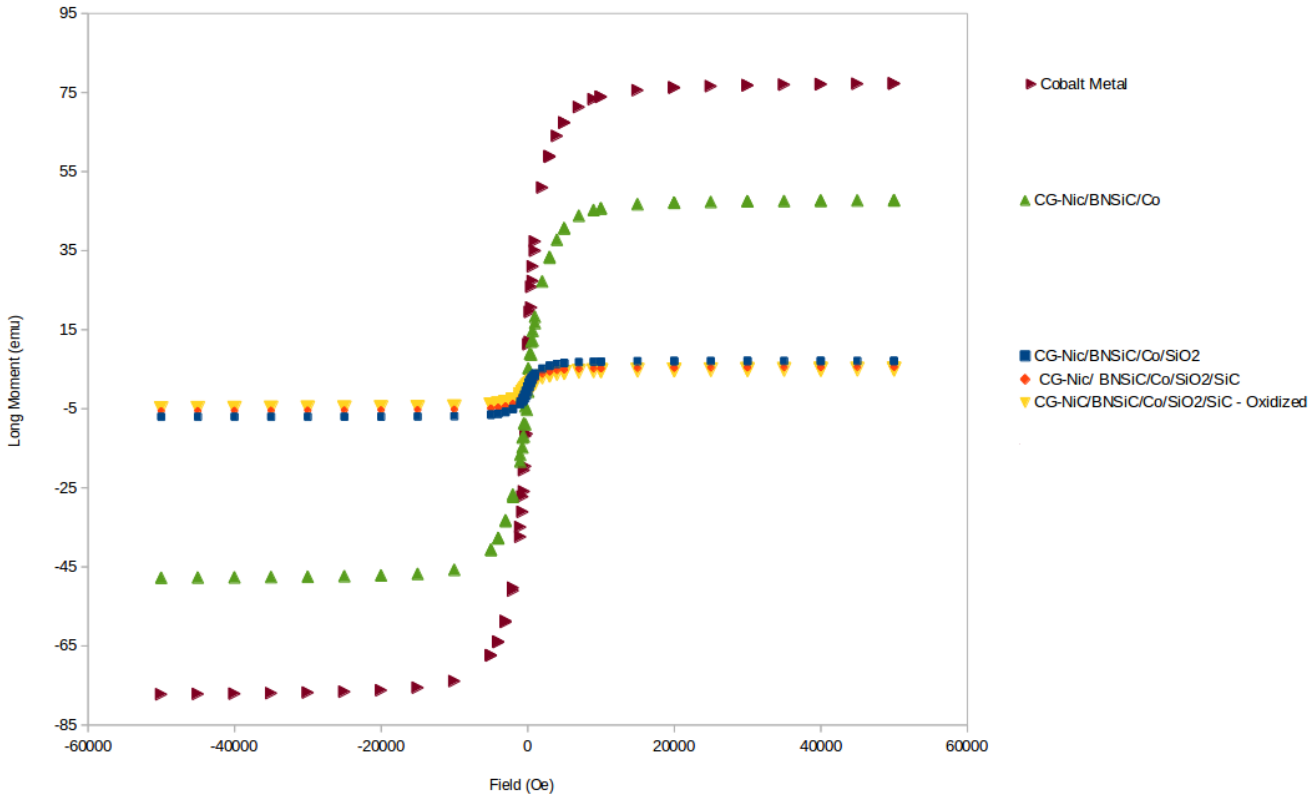

Figure 5-16 Long Moment vs. Magnetic Field Plot from SQUID Measurements

The largest magnetic moment was the pure cobalt metal, followed by the fiber and interface coated with cobalt only. The composite assembled with only the SiO_2 protective coating, the composite with both SiO_2 and CVI SiC, and the oxidized completed composite all had similar magnetic moments which were less than that of the material with only cobalt and the pure cobalt metal. These results are discussed and tabulated in **Section 5.5.5** and *Table 5-4*.

5.4.5 Instron Tensile Testing

Tensile testing was performed on the composite in various states of fabrication beginning with the as-received CG Nicalon® fiber. These studies were performed to determine the effect of applications of the various coatings on the tensile strength of the material, as well as to

determine the effect of oxidation on the strength of the fiber with and without a protective coating.

Samples were mounted in the card-stock apparatus described in **Section 5.3** for tensile testing, and at least ten samples of each test were performed. Outliers (incomplete breaks, fiber pullout, fractures at mounting points) were omitted and averages were calculated for each set of materials. A sample of data obtained directly from the Instron of as-received CG Nicalon® fiber is shown in *Figure 5-17*. The highest load measured was used to calculate the Ultimate Tensile Strength using the cross sectional area and is described in **Section 5.5.6**.

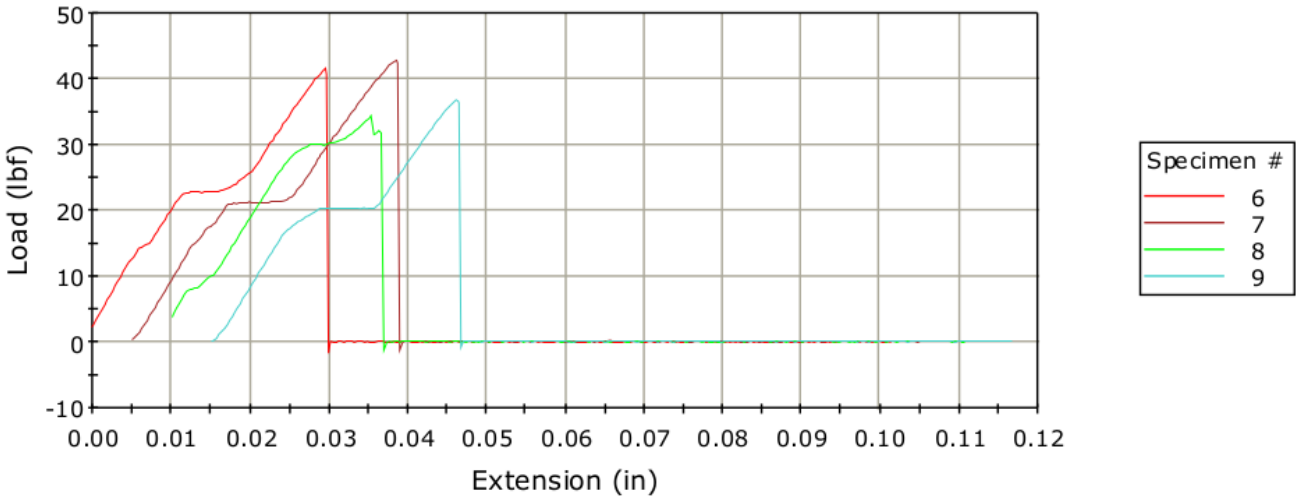

Figure 5-17. CG-Nicalon® As Received, Example of Data Obtained from Instron Tensile Tester

The plot showed mostly clean breaks in all of the samples, indicated by an increase in load force followed by a sharp decrease where the sample broke. These samples were in good agreement with each other and none were omitted as outliers. Load values for the composites in various states were summarized in *Table 5-1*, below.

Table 5-1. Average Values Obtained from Tensile Testing

Sample	Load (lbf) and Standard Deviation
CG-NiC As Received	38.30 ± 4.41
CG-NiC BN SiC	30.15 ± 5.16
CG-NiC BN SiC Co	22.16 ± 1.66
CG-NiC BN SiC Co Oxidized	- *
CG-NiC BN SiC Co SiO_2 SiC	39.03 ± 2.96
CG-NiC BN SiC Co SiO_2 SiC Oxidized	35.69 ± 4.01

*** Samples were too brittle to obtain data**

As-received fiber samples gave the highest strength values, and all subsequent applications of coatings further reduced the tensile strength. Oxidation of the magnetic fibers with no protective coatings produced samples so brittle that no data were obtained. The samples would break in the sample holder before the clamps were properly fastened, and even the slightest force would cause the fibers to fracture. Magnetic samples which had a SiO_2 and SiC protective layer applied allowed for strength high enough to be mounted in the clamps and produced load values lower than that of unoxidized samples, however much of the strength was preserved.

5.5 Discussion

5.5.1 Fabrication of Composite

Initial studies in the multi-step fabrication process of a magnetic ceramic matrix composite were much more involved than what was detailed in this thesis. Studies included the use of other magnetic metals, including iron and nickel, deposited using CVD and electroless deposition respectively, but were omitted from this work for simplicity. Initial use of the cenospheres was intended for a filler for use in PIP composites, but studies quickly proved that the cenospheres were difficult to coat uniformly and resulted in loss of magnetism when used with commercially available pre-ceramic polymers including Starfire® SMP-10. Studies were also performed using oxide fibers including Nextel™ 440 (alumina – boria – silica) but were quickly abandoned

when adhesion problems occurred with all magnetic material applications. The most successful method for creating a magnetic composite was with the use of cobalt through the reduction method with CG-Nicalon® fabric.

Magnetism was tested periodically using a cobalt-samarium handheld magnetic as a simple means of confirming the presence of magnetism before more complex methods of analysis. Samples with the initial coating of cobalt showed magnetism, but when they were coated with the protective layer of SiC, these magnetic properties were lost. This loss of magnetism was due to the reaction of cobalt with the chlorine in the methyltrichlorosilane used during the CVD deposition[129]. To combat this issue, a flash coating of CVD SiO_2 was deposited before the CVI SiC matrix application. The magnetic properties of cobalt metal were preserved after the deposition of only SiO_2, and after the SiC matrix was applied, the samples still maintained magnetic characteristics. This bench-top method for confirming the presence of magnetism allowed for fast judgments of success or failure of the developing procedure and were later used as a basis for further magnetic testing using SQUID.

5.5.2 X-Ray Diffraction

Cobalt coated cenospheres were analyzed using XRD to determine the crystalline phases present. A plot showing the diffraction patterns of both as-received cenospheres and cobalt coated cenospheres is shown in *Figure 5-18* below, where the two signals observed for cobalt have been marked with a "*".

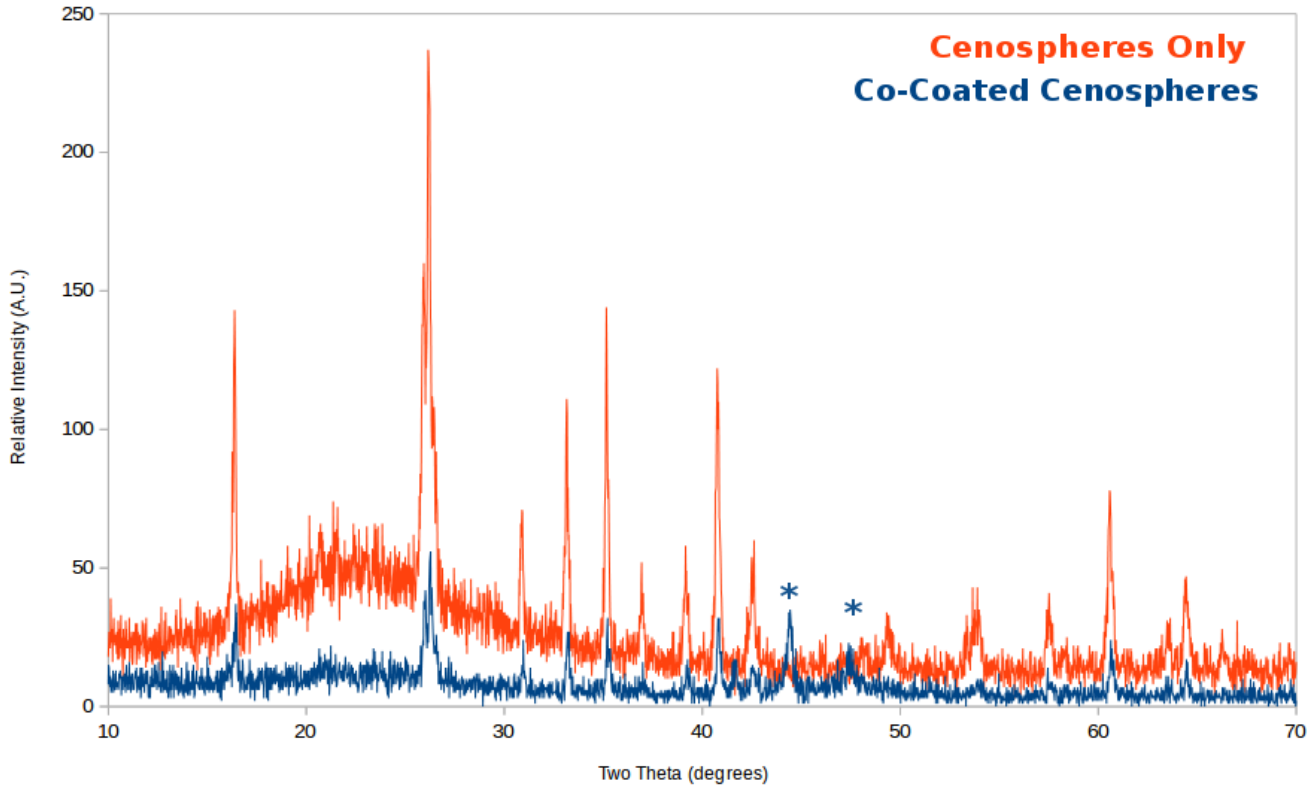

Figure 5-18. Overlay of XRD Patterns of Cenospheres and Co-Coated Cenospheres

All of the signals in the cenosphere diffraction pattern were indexed to mullite ($Al_6Si_2O_{13}$), and the indexed signals were summarized in *Table 5-2*.

Table 5-2. JCPDS vs. Experimental Reflections for Cenopheres

h k l	Mullite 2θ	Mullite I/I_0	Experimental 2θ	Experimental I/I_0
(1 1 0)	16.43	50.0	16.36	60.3
(2 1 0)	26.27	100	26.17	100
(0 0 1)	30.96	20	30.92	30.0
(2 2 0)	33.23	40.0	33.14	47.0
(1 1 1)	35.28	50.0	35.16	60.1
(2 0 1)	39.28	20	39.12	24.5
(1 2 1)	40.87	60.0	40.75	51.5
(2 3 0)	42.59	25.0	42.54	25.3
(3 1 1)	49.27	10.0	49.32	14.4
(3 2 1)	53.88	14.0	53.90	18.1
(0 4 1)	57.56	20.0	57.45	17.3
(3 3 1)	60.71	35.0	60.62	32.9
(0 0 2)	64.57	18.0	64.40	19.8

DB Card No. 00-015-0776

The diffraction pattern for the cobalt coated cenospheres showed the same reflection patterns as in the cenospheres, as expected for a coated material. The cobalt coating was not thick enough to cover the signal for the cenospheres. The signals that did not index to mullite were assigned to cobalt metal and were summarized in *Table 5-3*.

Table 5-3. JCPDS vs. Experimental Reflections for Cobalt

h k l	SiC 2θ	SiC I/I_0	Experimental 2θ	Experimental I/I_0
(1 1 1)	44.23	100	44.39	100
(2 0 0)	51.53	41.9	51.46	31.4

DB Card No. 01-077-7456

Both diffraction patterns showed sharp, resolved signals, with the exception of a broadened reflection near $2\theta = 27$. This signal was indexed to silicon dioxide from the glass slide used during analysis. Both patterns had noise and relatively low signal compared to diffraction patterns obtained for other ceramics. This may be due to the small size of the cenospheres, as well as their low density which resulted in shifting of the powder in the sample holder with very little agitation. The powder was also quite susceptible to static charge, resulting the difficulty getting the powder to stay in the sample holder during preparation.

5.5.3 Scanning Electron Microscopy

5.5.3.1 Magnetic Coatings

Magnetic samples required special sample preparation for use in the electron microscope. Magnetic particles can interfere with the electron beam and become lodged in the detector, resulting in damage to the instrument. With these considerations in mind, samples were mounted carefully to ensure no lose particles, and were exposed to a strong magnet to remove any free particles before putting into the instrument. Magnetic samples also resulted in charging of the sample, making obtaining images difficult. In times when charging was a problem, a concentric backscatter (CBS) detector was used to assist with obtaining micrographs.

Uncoated cenospheres were examined for the their shape, size, and surface properties, showing small balls of smooth ceramic, varying in size from about 100 nm to 50 micron. The interior of the spheres could be seen where they had been broken open and the thickness of the mullite shell was in the micron range. The spheres were quite uniform in size and shape and had very smooth surfaces with little variation in both the surface and bulk of the material.

Cenospheres that had been coated with cobalt using the reduction method were examined for broken or damaged spheres to gain information about the thickness and uniformity of the coating. Areas where the on the spheres where the coating was intact on the spheres gave no detail of depth of the coating. The cobalt coated particles showed some clumping of spheres, as expected with a coating process in which agitation was not added. Despite this, the spheres were still evenly coated, likely due to the process of coating while still in solution. The flowing aqueous solution allowed for movement of the particles until evaporation had occurred. This

was also evident in the coated fibers, which showed surprisingly little signs of clumping in the micrographs.

The coating on the fibers did show evidence of flaking at the ends of the fibers where they had been cut with a blade for sample preparation. Overall, the coating was relatively uniform and there were few instances of fibers being entirely stuck together, which would result in reduced area for the protective coatings to be applied. The coating appeared to have the same morphology as on the spheres, as expected. The particles were small and difficult to see when increasing the magnification.

5.5.3.2 Fabrication of Magnetic CVI Composite

Micrographs of fibers with interface, cobalt, and silicon dioxide coatings showed clear, concentric rings of each coating along the perimeter of the fiber. The grainy cobalt coating was uniform along the fibers and there were no signs of spallation or separation as observed in the fibers coated with cobalt only. The application of SiO_2 helped to fill in gaps in the metal, preventing the cobalt coating from separating from the fiber. The cobalt was containing tightly around the circumference of the fiber and there was no signs of clump formation or unattached cobalt clusters. Coating thickness was not a concern in these preliminary studies and was not varied. Evidence of complete application of the metal around the substrates was sufficient and the only consideration in these studies. The SiO_2 was applied as a flash coating, or a very quick coating just thick enough to cover the material. The silicon dioxide encapsulated the cobalt metal, protecting it from damage that occurred during the silicon carbide infiltration. The thin coatings of both cobalt and silicon dioxide did not fully densify the composite, leaving large gaps for the infiltration of SiC performed in the next step of the fabrication process.

The completed composite showed the thick, dense silicon carbide infiltration. The silicon carbide completely filled the majority of pores in the composite that were present when only the SiO_2 coating was applied. The silicon carbide was uniform and fully covered the previous

coatings applied to the fiber. The micrographs obtained with the CBS detector showed the cobalt had migrated during the deposition process and was no longer in tight rings along the perimeter of the fiber. This may be due to the heat at which the material was subjected to, though the temperature was kept well below the melting points of both cobalt (1495˚C) and silicon dioxide (1600˚C). Despite the cobalt migrating during the deposition process, the material still retained magnetic properties, unlike the samples which did not have the SiO_2 flash coatings applied.

5.5.4 Energy Dispersive X-Ray Spectroscopy

Elemental mapping was used to determine the elemental distribution throughout the composite material. This method was not used for any quantitative purpose but rather to determine the location of the magnetic material in the composite. The elemental mapping showed carbon present in both the silicon carbide CG-Nicalon® fiber, as well as in the silicon carbide matrix, as expected. The carbon was shown to directly correlate with the presence of carbon in the fiber and matrix, and was also present in the areas closer to the fiber where there was less presence of carbon, consistent with the silicon dioxide coating applied over the cobalt metal. Oxygen was primarily present in the matrix area, correlating with both the silicon and the cobalt around the fiber. This suggests the oxidation of some of the cobalt metal, as expected after heating the sample twice for the silicon dioxide and silicon carbide depositions. Finally, cobalt was present as both a ring around the fiber, as well as distributed around the fiber and especially between two fibers placed closely together. The cobalt was not distributed through the entire matrix, but clearly had migrated from its initial location around the circumference of the fiber. Overall, despite the potential oxidation and the migration of the cobalt metal, the composite still retained magnetic properties, as well as strength properties.

5.5.5 SQUID Magnetic Measurements

Magnetic measurements were obtained for the composite as it was fabricated to determine the effect of the applications of coatings on the magnetic moment, as well as to determine the effect of oxidation on the ferromagnetic properties of the composites. Cobalt metal was also analyzed as a comparison for the cobalt containing materials. The values of magnetic moment, expressed in emu per gram are summarized in *Table 5-4*.

Table 5-4. Magnetic Moments for Magnetic Composite Materials

Sample	Magnetic Moment (emu/gram)
Cobalt Metal	77.20
CG-NiC BN SiC Co	47.70
CG-NiC BN SiC with CVI SiC	0 (non-ferromagnetic)
CG-NiC BN SiC with CVD SiO_2	7.06
CG-NiC BN SiC Co with CVD SiO_2 and CVI SiC	5.58
CG-NiC BN SiC Co Oxidized	0 (non-ferromagnetic)
CG-NiC BN SiC Co SiO_2 SiC Oxidized	4.99

Two of the characterized materials did not display ferromagnetic properties, which was determined not only through the use of a handheld magnetic to confirm the loss of magnetism, but also through the slope of the ends of the Sigmoidal curve from the SQUID measurements. In both the CG-Nicalon®/BN/SiC/Co/CVI SiC material, and the CG-Nicalon®/BN/SiC/Co which had been oxidized, the slopes were positive, indicating the presence of paramagnetism but not ferromagnetism. In the sample with CVI SiC deposited directly over the cobalt, it was suspected that the chlorine from the methyltrichlorosilane precursor reacted with the cobalt metal, forming cobalt chloride. This was indicated by the slight purple color of the composites where CVI SiC was deposited directly onto the cobalt. It was this loss of ferromagnetism that led to the deposition of a flash coating of SiO_2 to preserve magnetic properties. The CG-Nicalon®/BN/SiC/Co composite which had been oxidized without a protective coating also

displayed no ferromagnetism and had positive slopes at the ends of the curve consistent with paramagnetism. It was suspected here that upon oxidation, the cobalt formed both CoO and Co_3O_4 [124] both of which are paramagnetic at the temperature at which the measurements were taken (300 K). It should be noted that below the Neél Temperatures of all three cobalt species formed ($CoCl_2$ = 25 K, CoO = 271 K[130], and Co_3O_4 = 30-40 K[131]) these compounds exhibit antiferromagnetic properties, which could be of interest for further studies.

The materials which did exhibit magnetic properties were also listed in *Table 5-4* with their magnetic moments. The as-received cobalt metal had the largest magnetic moment, as expected for a bulk material where the moment was expressed in emu per gram. The interface-coated fiber with cobalt metal coating had the next largest magnetic moment, while significantly less than the bulk metal was still relatively high, which was expected because no coatings were applied over the cobalt. The first significant decrease in magnetic moment occurred with the application of the SiO_2 protective coating over the metal. Though the magnetic moment decreased, the samples still exhibited strong ferromagnetic properties, as well as the added benefit of oxidation resistance.

The completed composite with both CVD SiO_2 and CVI SiC had a slightly smaller magnetic moment than with only the SiO_2 applied, but overall the value did not decrease significantly. This demonstrated that the SiO_2 protecting the cobalt from oxidation, as the samples lost ferromagnetic properties without the flash coat of SiO_2 applied. Finally, the completed composite was oxidized at 800°C for 36 hours and still maintained ferromagnetic properties, showing a magnetic moment only slightly less than that of the unoxidized sample. This result was excellent in comparison to the unprotected cobalt, which lost all ferromagnetism. This result showed successful protection of the cobalt, allowing the composite to retain ferromagnetism at elevated temperatures and in oxidizing environments.

5.5.6 Instron Tensile Testing

Tensile testing was performed on the composite, beginning with the as-received CG-Nicalon® fiber and the fiber coated with the BN/SiC duplex interface. The other coatings were then applied to the composite material and strength measurements were obtained. These measurements from the Instron instrument were reported in pounds of force, which did not account for cross sectional area. To standardize these strength values, the Load values (lbf) were converted to KSI, or kilopounds per square inch. This value, the ultimate tensile strength (UTS) accounted for the increasing area of the material as each coating was applied. Cross-sectional area was measured using SEM and filaments per fiber tow was approximated to be 500, in accordance with the Technical Data Sheet for CG Nicalon®. These calculated values were summarized in *Table 5-5* below.

Table 5-5. Calculated Average KSI Values Obtained from Tensile Testing

Sample	Load (lbf) and Standard Deviation	Ultimate Tensile Strength (KSI)
CG-NiC As Received	38.30 ± 4.41	274.24 ± 27.90
CG-NiC BN SiC	30.15 ± 5.16	190.74 ± 32.65
CG-NiC BN SiC Co	22.16 ± 1.66	158.68 ± 11.91
CG-NiC BN SiC Co Oxidized	- *	- *
CG-NiC BN SiC Co SiO_2 SiC	39.03 ± 2.96	114.70 ± 8.70
CG-NiC BN SiC Co SiO_2 SiC Oxidized	35.69 ± 4.01	102.95 ± 11.78

*** Samples were too brittle to obtain data**

As-received fiber was shown to undergo a strength loss from the initial application of the BN/SiC interface. This was expected and is typical of coated materials like these. Despite the strength decrease, the interface served as a means to disperse energy through the composite as it underwent strain and stress. Further application of the cobalt coating resulted in another decrease in overall strength, but this decrease was not as significant, and was again expected due to the processing required to apply the and reduce the cobalt solution. The ultimate goal of

this research was to fabricate a magnetic CMC and decreases in strength from the as received fiber was expected.

The first oxidation study was performed on the fiber coated with only cobalt. One area of concern with the application of magnetic materials into a CMC was the susceptibility to oxidation that was inevitable due to the operational conditions necessary for use of these materials in aircraft applications. As expected, the unprotected cobalt readily oxidized, losing all of its magnetic properties, as well as all of its tensile strength. The samples were so brittle that it was not possible to mount these fiber tows in the Instron without breaking them prior to even running the extension program. The clamps on the instrument could not be tightened without failure of the composite. The samples were extremely brittle and no strength data could be obtained.

Application of the SiO_2 and SiC protective coatings again resulted in a decrease of tensile strength, as expected due to two heating and cooling cycles, as well a deposition which subjected the composite to corrosive precursors. Oxidation of the samples with protective coatings showed very little strength decrease despite exposure to air 800°C for 36 hours. This indicated that the protective coatings were successful in preserving the strength of the composite and showed promising results for use in aircraft applications.

5.6 Conclusions.

The goal for this research was to design and fabricate a ceramic matrix composite with magnetic properties, and this goal was reached with the inclusion of cobalt metal and SiO_2 and SiC protective coatings into the CMC. Initial experiments with other magnetic materials including iron and nickel proved difficult but still showed promise as candidate materials with further research. Overall, the application of both the cobalt metal and the protective coatings resulted in a significant strength decrease (60% UTS loss between the as-received fiber and completed composite), as expected with the application of any coating as compared to the

as-received fiber, however with the ultimate goal in mind, these studies were a success. A magnetic composite was designed and fabricated, and both magnetic and strength properties were preserved during a 36 hour oxidation cycle. Strength decreased by 10% from the unoxidized composite after the air heat treatment, and magnetism decreased 11% during the oxidation of the completed CMC. Without the application of the protective coatings over the magnetic metal, the strength decreased so much that measurements could not be taken, and all ferromagnetic properties were lost. Comparing this result to the 10% and 11% decreases in strength and magnetic moment respectively, the application of the protective coatings allowed this material to withstand both heat and oxidation, opening doors for advanced high temperature applications. Further studies on these materials are necessary to determine the longevity of these materials under operational conditions, as well as specific studies on the magnetic properties and how these can be used to alternate applications in aircraft technologies. These multi-layered systems provide interesting properties for military applications and more in-depth, specific studies may yield information about the performance of these composites for these types of applications.

Chapter 6 Conclusions and Future Work

The research that has been described in this dissertation discussed a variety of methods and materials for use in the development of Ceramic Matrix Composites. These materials were designed for the high-temperature and oxidizing environments like those present in aerospace and aircraft applications and high temperature properties were a motivating factor of all of the materials in this research. Both pre-ceramic polymers and a variety of coatings were used to advance the thermal, mechanical, oxidation resistance, and magnetic properties of components in CMCs.

A series of coatings including carbides, borides, and nitrides were deposited using CVD and were studied for the rates of deposition, as well for the properties of the coatings. These coatings were used both for duplex interface coatings for CMCs and for the initial studies to fabricate a coated fiber for use as reinforcement in these composites. Several of the coatings produced were used in the following sections of research to assemble CFR-CMCs.

A novel polycarbosilane was designed and synthesized using a novel, simplified method for producing moderate quantities of polymer with improved shelf life and air-resistance and ceramic yield. This polymer was produced for a bench-top synthesis and was characterized extensively to determine the structure, functional group environments, and the mechanism of ceramic formation. This material showed excellent properties as compared to commercially available polymers, including a higher ceramic yield.

A modified polymer designed to produce silicon carbide and titanium diboride upon pyrolysis was produced from a commercially available polymer. This material used a two-step process to incorporate titanium and boron into the material, providing a simple process for creating this material. The polymer was characterized to determine the effect of the additives on the crystallization process and the ceramic was studied for crystalline phases. CFR-CMCs were fabricated from both the neat polymer and the modified polymer and the mechanical

properties were compared. The titanium diboride modified material proved to have withstand higher flexural stress before failure than in the unmodified material.

Finally, a magnetic CMC was developed and fabricated for use in advanced composite usage at elevated temperatures. Protective coatings were applied over the magnetic material to preserve strength and magnetic properties after oxidation at high temperatures. These materials were explored for their chemical properties as well as mechanical properties and they exhibited oxidation resistance after the protective coatings were applied. These protective coating were shown to preserve both strength and magnetic properties in the composites after oxidation at 800°C. This unique composite provided advanced properties and allowed for use in high temperature and oxidizing operational conditions for aerospace and military applications.

Future work in this research includes:

- Continued modification of polycarbosilane synthesis to produce bulk quantities of polymer for use in full scale ceramic matrix composites, as well as the fabrication of CMCs using this PCS for impregnations. Mechanical testing would be used to compare to other commercially available polymers to determine how effective the polymer is as a matrix material.

- Use of the synthesized polymer in the titanium and boron addition studies. The polymer may behave similarly to the commercially available Starfire® SMP-10 and the same methods for titanium and boron incorporation may work for the new PCS, producing a superior polymer for use in these dopant studies.

- Further heteroatom addition studies, including incorporation of zirconium and hafnium diborides. Initial studies showed crystalline phases of hafnium diboride and silicon carbide in following the same synthetic procedure detailed in **Section 4.2.1**

using hafnium isopropoxide isopropanol adduct solution, and these modification may provide a ceramic with superior high temperature properties.

- Determine the actual concentration of titanium diboride in the final ceramic product and how it is affected by initial concentration of titanium precursor added. Studies to determine the optimal concentration of TiB_2 for maximum strength properties as compared to the concentrations in Sylramic® fiber would provide information about the effect of the additives on the properties of the ceramics produced.

- Design a method for spinning fiber from the titanium modified polymer before processing with the titanium diboride heat treatment. This fiber could be characterized for strength properties as compared to the commercially available SiC – TiB_2 fibers.

- Continued studies using other magnetic materials in composites, including revisiting nickel and iron, as well as other ferromagnetics like samarium cobalt. Other metals or compounds could provide greater magnetic properties or have better oxidation resistance at high temperaures, providing a more effective material for high temperature magnetic composites. These materials would be tested for their properties in military applications and their effectiveness for these usages determined.

References

1. Scala, E. P. *A brief history of composites in the U.S."The dream and the success." JOM , 48*, 45-48.

2. Ding, D. In *2 - Processing, properties and applications of ceramic matrix composites, SiCf/SiC: an overview;* Low, I. M., Ed.; Advances in Ceramic Matrix Composites; Woodhead Publishing: **2014**; pp 9-26.

3. Aviation, G. E. *GE Successfully Tests World's First Rotating Ceramic Matrix Composite Material for Next-Gen Combat Engine*. *General Electric Aviation* **2015**.

4. Bullock, E.; Brunetaud, R.; Conde, J. F.; Keown, S. R.; Pugh, S. F. *Research and Development of High Temperature Materials for Industry;* Springer Netherlands: **2012**; .

5. Higgins, R. A. *Materials for Engineers and Technicians;* Taylor & Francis: **2006**.

6. Sims, C. T. *A History of Superalloy Metallurgy for Superalloy Metallurgists;* General Electric Company: Schenectady, New York, **1982**; , pp 399-418.

7. Sengupta, A.; Putatunda, S. K.; Bartosiewicz, L.; Hangas, J.; Nailos, P. J.; Peputapeck, M.; Alberts, F. E. Tensile behavior of a new single-crystal nickel-based superalloy (CMSX-4) at room and elevated temperatures. *Journal of Materials Engineering and Performance* **1994**, *3*, 73-81.

8. Singerman, S. A.; Jackson, J. J. In *In Titanium Metal Matrix Composites for Aerospace Applications;* Superalloys; Pratt and Whitney, GE Aircraft Engines: **1996**; .

9. Campbell, F. C. *Structural Composite Materials;* ASM International: **2010**;

10. Rosso, M. In *In Ceramic and Metal Matrix Composites: Route and Properties;* Achievements in Mechanical and Materials Engineering; Polytechnic of Turin, Dep. of Material Science and Chemical Engineering: 2005; .

11. Wachtman, J. B. *18th Annual Conference on Composites and Advanced Ceramic Materials - A: Ceramic Engineering and Science Proceedings, Volume 15;* Wiley: **2009**; .

12. Hearle, J. W. S., Ed.; In *High-performance Fibers;* Woodhead Publishing Ltd: **2001**; , pp 1-17

13. Alavudeen, A.; Venkateshwaran, N.; Jappes, J. T. W. *A Textbook of Engineering Materials and Metallurgy;* Laxmi Publications Pvt Limited: **2006**; .

14. Grashchenkov, D. V.; Balinova, Y. A.; Tinyakova, E. V. Aluminum oxide ceramic fibers and materials based on them. *Glass and Ceramics* **2012**, *69*, 130-133.

15. Clauß, B. In *Fibers for Ceramic Matrix Composites;* Ceramic Matrix Composites; Wiley-VCH Verlag GmbH & Co. KGaA: **2008**; pp 1-20.

16. Mazdiyasni, K. S. *Fiber Reinforced Ceramic Composites: Materials, Processing, and Technology;* Noyes Publications: **1990**; .

17. Xia, Z.; Li, L. In *12 - Understanding interfaces and mechanical properties of ceramic matrix composites;* Low, I. M., Ed.; Advances in Ceramic Matrix Composites; Woodhead Publishing: **2014**; pp 267-285.

18. Wiederhorn, S. M. Brittle Fracture and Toughening Mechanisms in Ceramics. *Ann. Rev. Mater. Sci.* **1984**, *14*, 373-403.

19. Evans, A. G.; Marshall, D. B. Overview no. 85 The mechanical behavior of ceramic matrix composites. *Acta Metallurgica* **1989**, *37*, 2567-2583.

20. Nguefack, M.; Popa, A. F.; Rossignol, S.; Kappenstein, C. Preparation of alumina through a sol-gel process. Synthesis, characterization, thermal evolution and model of intermediate boehmite. *Phys. Chem. Chem. Phys.* **2003**, *5*, 4279-4289.

21. Geim, A. K.; Grigorieva, I. V. Van der Waals heterostructures. *Nature* **2013**, *499*, 419-425.

22. Paine, R. T.; Narula, C. K. Synthetic routes to boron nitride. *Chem. Rev.* **1990**, *90*, 73-91.

23. Balandin, A. A. Thermal properties of graphene and nanostructured carbon materials. *Nat Mater* **2011**, *10*, 569-581.

24. Palucka, T.; Bensaude-Vincent, B. Textron Specialty Materials. *History of Science and Technology* **2002**, *Dibner Fund and the Alfred P. Sloan Foundation*.

25. Schmidt, S.; Beyer, S.; Knabe, H.; Immich, H.; Meistring, R.; Gessler, A. Advanced ceramic matrix composite materials for current and future propulsion technology applications. *Acta Astronaut.* **2004**, *55*, 409-420.

26. Miller, R. A. Thermal barrier coatings for aircraft engines: history and directions. *J. Therm. Spray Technol. , 6*, 35-42.

27. Mallick, P. K. *Fiber-Reinforced Composites: Materials, Manufacturing, and Design, Third Edition;* CRC Press: **2007**;

28. Riley, F. L. Silicon Nitride and Related Materials. *J Am Ceram Soc* **2000**, *83*, 245-265.

29. Ervin, G. Oxidation Behavior of Silicon Carbide. *J Am Ceram Soc* **1958**, *41*, 347-352.

30. McCauley, R. A. *Corrosion of Ceramic Materials, Third Edition;* CRC Press: **2013**;.

31. Lazzeri, A. In *Ceramics and Composites Processing Methods, CVI Processing of Ceramic Matrix Composites;* Bansal, N. P., Boccaccini, A. R., Eds.; John Wiley & Sons, Inc.: **2012**; Vol. First Edition, pp 313.

32. Myers, P. Narottam P. Bansal and Jacques Lamon (Eds): Ceramic Matrix Composites Materials, Modeling and Technology. *Chromatographia* **2015**, *78*, 843-844.

33. Bansal, N. P.; Lamon, J. *Ceramic Matrix Composites: Materials, Modeling and Technology;* Wiley: **2014**; .

34. Reutenauer, Justin W., "Advances in Ceramic Coatings and Ceramic Matrix Composite Fabrication" (**2013**). *Doctoral Dissertations.* Paper 17. http://digitalcommons.uconn.edu/dissertations/17

35. Miguel, A. S. Composite floor armor for military tanks and the like. **1983**.

36. Krenkel, W.; Berndt, F. C/C–SiC composites for space applications and advanced friction systems. *Materials Science and Engineering: A* **2005**, *412*, 177-181.

37. Luthra, K. L. Emerging Applications and Challenges in using Ceramics at General Electric. *Ceramic & Metallurgy Technologies, GE Global Research* **2011**.

38. Dupont Industries, Kevlar Military Personal Protection Equipment Body Armor. *http://www.dupont.com/products-and-services/personal-protective-equipment/body-armor.html* (accessed 11/02, **2015**)

39. Strasser, T. E.; Atmur, S. D. Fiber reinforced ceramic matrix composite armor. **2001**.

40. C. Becker, *Little, Strong, Black,* Cristophorus, Vol. 306, pp. 40-42.

41. Mortensen, A. *Concise Encyclopedia of Composite Materials;* Elsevier Science: **2006**; .

42. Rodgers, T.; Zhao, H.; Wadley, H. In *Integrated Development of Vapor Deposition for Non-line-of-sight Substrates;* American Institute of Aeronautics and Astronautics: **2012**; .

43. Creighton, J. R.; Ho, P. In *Introduction to Chemical Vapor Deposition (CVD);* ASM International, Ed.; Chemical Vapor Deposition; American Technical Publishers Ltd.: **2001**; pp 3.

44. Jones, J. G.; Jero, P. D.; Garrett, P. H. In-situ control of chemical vapor deposition for fiber coating. *Eng Appl Artif Intell* **1998**, *11*, 619-626.

45. Kmetz, M.A.; Laliberte, J.M.; Willis, W.S.; Suib, S.L.; Galasso, F.S.; "Synthesis, Characterization, and Tensile Strength of CVI SiC/BN/SiC Composites," Cer. Eng. Sci. Proc., Vol. 12, Issue 9-10, pg. 216, 1-2174, (**1991**).

46. Kmetz, M. A. Chemical Vapor Deposited Fiber Coatings and Chemical Vapor Infiltrated Ceramic Matrix Composites, University of Connecticut, Storrs, CT, **1992**.

47. Low, I. M. In *1 - Advances in ceramic matrix composites: an introduction;* Low, I. M., Ed.; Advances in Ceramic Matrix Composites; Woodhead Publishing: **2014**; pp 1-6.

48. N.Bansal, A. Boccaccini, Ceramics and Composite Processing Methods, John Wiley and Sons, Inc. **2012**.

49. Balasubramanian, M. *Composite Materials and Processing;* CRC Press: **2013**; .

50. Ly, H. Q.; Taylor, R.; Day, R. J.; Heatley, F. Conversion of polycarbosilane (PCS) to SiC-based ceramic Part II Pyrolysis and characterisation. *J. Mater. Sci. , 36*, 4045-4057.

51. Interrante, L. V.; Whitmarsh, C. W.; Sherwood, W.; Wu, H. -.; Lewis, R.; Maciel, G. High Yield Polycarbosilane Precursors to Stoichiometric SiC. Synthesis, Pyrolysis and Application. *MRS Online Proceedings Library Archive* **1994***, 346*, 595 (11 pages).

52. Saini, Vikram, "Measurement of elastic moduli of porous SiC/SiC ceramic matrix composites using ultrasonics" (**1994**). Retrospective Theses and Dissertations. Paper 249

53. King, D. S.; Fahrenholtz, W. G.; Hilmas, G. E. Silicon carbide–titanium diboride ceramic composites. *Journal of the European Ceramic Society* **2013***, 33*, 2943-2951.

54. Munro, R. G. Material properties of titanium diboride. *Journal of Research of the National Institute of Standards and Technology* **2000***, 105*, 709-720.

55. Tarry, C. A. Process for densification of titanium diboride. **1992**.

56. Yun, H.; Wheeler, D.; Chen, Y.; DiCarlo, J. In *Thermo-Mechanical Properties of Super Sylramic SiC Fibers;* Mechanical Properties and Performance of Engineering Ceramics and Composites: Ceramic Engineering and Science Proceedings; John Wiley & Sons, Inc.: **2005**; 2008; pp 59-66.

57. Materials & Manufacturing Directorate. AFRL Commercializes Advanced Silicon Carbide Fibers *Air Force Print News* **2007**.

58. Tracton, A. A. *Coatings Materials and Surface Coatings;* CRC Press: **2006**; .

59. Heck, C. In Magnetic Materials and their Applications. *1 - Introduction;* Heck, C., Ed.; Magnetic Materials and their Applications; Butterworth-Heinemann: **1974**; pp 1-3.

60. Heck, C. In Magnetic Materials and their Applications. *15 - Magnetic materials for information storage;* Heck, C., Ed.; Magnetic Materials and their Applications; Butterworth-Heinemann: **1974**; pp 580-654.

61. Heck, C. In Magnetic Materials and their Applications. *17 - Materials for magnetic shielding;* Heck, C., Ed.; Magnetic Materials and their Applications; Butterworth-Heinemann: **1974**; pp 673-679.

62. Stabik, J.; Chrobak, A.; Haneczok, G.; Dybowska, A. Magnetic properties of polymer matrix composites filled with ferrite powders. *Mater. Sci. Eng.* **2011***, 48*, 97-102.

63. Coons, T. P. Ceramic Matrix Composites: An Investigation into Methods to Improve Environmental, Thermal, and Mechanical Properties, University of Connecticut, Storrs, CT, **2012**.

64. Hill, C. L. Interface and Matrix Processing Evaluation for Non-Oxide Ceramic Matrix Composites, University of Connecticut, Storrs, CT, **2002**.

65. Kmetz, M. Multilayered boron nitride/silicon nitride fiber coatings. **2009**.

66. Evans, A. G.; Zok, F. W.; Mackin, T. J. In *Chapter 1 - The structural performance of ceramic matrix composites;* Nair, S. V., , and Jakus, K., Eds.; High Temperature Mechanical Behaviour of Ceramic Composites; Butterworth-Heinemann: Newton, **1995**; pp 3-84.

67. Lavrenko, V. A.; Alexeev, A. F. High-temperature oxidation of boron nitride. *Ceram. Int.* **1986**, *12*, 25-31.

68. Bocanegra-Bernal, M. H.; Matovic, B. Mechanical properties of silicon nitride-based ceramics and its use in structural applications at high temperatures. *Materials Science and Engineering: A* **2010**, *527*, 1314-1338.

69. Ren, H.; Zhang, L.; Su, K.; Zeng, Q.; Cheng, L. Thermodynamic study on the chemical vapor deposition of silicon nitride from the SiCl4–NH3–H2 system. *Computational and Theoretical Chemistry* **2015**, *1051*, 93-103.

70. Zhang, W. G.; Hüttinger, K. J. CVD of SiC from Methyltrichlorosilane. Part I: Deposition Rates. *Chemical Vapor Deposition* **2001**, *7*, 167-172.

71. Besmann, T. M.; Lowden, R. A. Titanium diboride ceramic fiber composites for Hall-Heroult cells. **1990**.

72. Baumgartner, H. R.; Steiger, R. A. Sintering and Properties of Titanium Diboride Made from Powder Synthesized in a Plasma-Arc Heater. *J Am Ceram Soc* **1984**, *67*, 207-212.

73. Eichhorn, S.; Hearle, J. W. S.; Jaffe, M.; Kikutani, T. *Handbook of Textile Fibre Structure: Natural, Regenerated, inorganic and Specialist Fibres;* Elsevier Science: **2009**;

74. Mallick, P. K. *Fiber-reinforced composites: materials, manufacturing, and design;* CRC Press: **2008**;

75. Corten, H. T. *Composite Materials : Testing and Design: (second Conference), held at Anaheim, Calif., 20-22 April 1971;* ASTM: **1972**;

76. Chawla, K. K. Thermal fatigue damage in Borsic AI (6061) composites. *J. Mater. Sci.* **1976**, *11*, 1567-1569.

77. Hwan, L.; Suib, S.; Galasso, F. Silicon Carbide-Coated Boron Fibers. *J Am Ceram Soc* **1989**, *72*, 1259-1261.

78. Tan, B. J.; Hwan, L.; Suib, S. L. Spectroscopic Characterization of CVD Ti Coating on SiC-Coated Boron Fibers. *Chem. Mater* **1991**, *3*, 368-378.

79. Emsley, J. *Nature's Building Blocks: An A-Z Guide to the Elements;* Oxford University Press: **2001**;

80. Goodfellow Metals, Alloys, Compounds, Ceramics, Polymers, Composites: Molybdenum: Material Information. Catalogues 2014-15.

81. Jones, R.; Szweda, A.; Petrak, D. Polymer derived ceramic matrix composites. *Composites Part A: Applied Science and Manufacturing* **1999**, *30*, 569-575.

82. Zhang, Z.; Scotto, C.,S.; Laine, R.,M. Processing stoichiometric silicon carbide fibers from polymethylsilane. Part 1 Precursor fiber processing. *J. Mater. Chem.* **1998**, *8*, 2715-2724.

83. Lee, S. G.; Fourcade, J.; Latta, R.; Solomon, A. A. Polymer impregnation and pyrolysis process development for improving thermal conductivity of SiCp/SiC–PIP matrix fabrication. *Fusion Eng. Des.* **2008**, *83*, 713-719.

84. Mukherjee, J.; Ranjan, A.; Saxena, A. K.; Das, P. K.; Banerjee, R. Liquid polycarbosilane derived SiC coating on silicon (1 1 1) wafer for enhanced mechanical properties. *Appl. Surf. Sci.* **2013**, *270*, 219-224.

85. Houser, E. J.; Simonson, D. L.; Stepnowski, J. L.; Papantonakis, M. R.; Ross, S. K.; Stepnowski, S. V.; Snow, E. S.; Perkins, K. F.; Bryant, C.; LaPuma, P.; Hook, G.; McGill, R. A. In *Design of Sorbent Hydrogen Bond Acidic Polycarbosilanes for Chemical Sensor Applications;* American Chemical Society: **2007**; Vol. 980, pp 71-87.

86. Wang, W.; Watari, F.; Omori, M.; Liao, S.; Zhu, Y.; Yokoyama, A.; Uo, M.; Kimura, H.; Ohkubo, A. Mechanical properties and biological behavior of carbon nanotube/polycarbosilane composites for implant materials.*Journal of Biomedical Materials Research Part B: Applied Biomaterials* **2007**, *82B*, 223-230.

87. Colombo, P. *Polymer Derived Ceramics: From Nano-structure to Applications;* DEStech Publications: **2010**;.

88. Y. Kim, D. G. Shin, H. R. Kim, D. Y. Han, Y. U. Kang, D. H. Riu, "Kumada Rearrangement of Polydimethylsilane Using a Catalytic Process", Key Engineering Materials, Vols. 317-318, pp. 85-88, **2006**.

89. Xing, X.; Liu, L.; Cao, F.; Li, X. D.; Chu, Z. Y.; Cheng, H. F. Silicon Carbide Base Ceramic Fiber Synthesis from Polycarbosilane-Modified Polymethylsilane Blend Polymers by Melt Spinning. *Mater. Sci. Forum* **2011**, *675-677*, 139-142.

90. Nannetti, C. A.; Ortona, A.; de Pinto, D. A.; Riccardi, B. Manufacturing SiC-Fiber-Reinforced SiC Matrix Composites by Improved CVI/Slurry Infiltration/Polymer Impregnation and Pyrolysis. *J Am Ceram Soc* **2004**, *87*, 1205-1209.

91. Lodhe, M.; Babu, N.; Selvam, A.; Balasubramanian, M. Synthesis and characterization of high ceramic yield polycarbosilane precursor for SiC. *Journal of Advanced Ceramics* **2015**, *4*, 307-311.

92. Whitmarsh, C. K.; Interrante, L. V. Synthesis and structure of a highly branched polycarbosilane derived from (chloromethyl)trichlorosilane. *Organometallics* **1991**, *10*, 1336-1344.

93. Takeda, M.; Sakamoto, J.; Imai, Y.; Ichikawa, H.; Ishikawa, T. In *Properties of Stoichiometric Silicon Carbide Fiber Derived from Polycarbosilane;* Proceedings of the 18th Annual Conference on Composites and Advanced Ceramic Materials?A: Ceramic Engineering and Science Proceedings; John Wiley & Sons, Inc.: 1994; **2008**; pp 133-141.

94. Jacobsen, A. J.; Barvosa-Carter, W.; Gross, A. F.; Cumberland, R.; Kirby, K. W.; Kisailus, D. Composite structures with ordered three-dimensional (3D) continuous interpenetrating phases. **2012**.

95. Starfire Systems, I., USA Star PCSTM SMP-10 Silicon Carbide Matrix Precursor Technical Data Sheet.

96. Huang, M.; Fang, Y.; Li, R.; Huang, T.; Yu, Z.; Xia, H. Synthesis and properties of liquid polycarbosilanes with hyperbranched structures. *J Appl Polym Sci* **2009**, *113*, 1611-1618.

97. Lee, R. Carbosilanes: Reactions & Mechanisms of SMP-10 Pre-Ceramic Polymers, Marshall Space Flight Center, Huntsville, AL, **2009.**

98. Yamaji, T.; Saito, T.; Hayamizu, K.; Yanagisawa, M.; Yamamoto, O. SDBS No. 497HSP-05-077. *National Institute of Advanced Industrial Science and Technology* .

99. Fiori, C.E., Newbury, D.E. and Myklebust, R.L. "*Artifacts Observed in Energy Dispersive Spectrometry in Electron Beam Instruments- A Cautionary Guide*", in Energy Dispersive X-Ray Spectrometry, *National Bureau of Standards Special Publication 604*, US Govt. Printing Office, Wash. DC 20402, Heinrich, K.F.J., Newbury, D.E., Myklebust, R.L. and Fiori, C.E., Editors, **1981**, pp. 315-340.

100. Sewell, T.; Weber, B. W.; Jaffer, M. A. EDX: Precision and Accuracy in EDX Analysis. *Centre for Imaging and Analysis, University of Capetown* .

101. Hyde, A. R. Ceramic matrix composites: high-performance materials for space application. *Mater Des* **1993**, *14*, 97-102.

102. Yun, H. M.; DiCarlo, J. A. In *In Comparison of the Tensile, Creep, and Rupture Strength Properties of Stoichiometric SiC Fibers;* 23rd Annual Cocoa Beach Conference sponsored by the American Ceramic Society. NAS A/TM-- 1999-209284; NASA/NTIS: Cocoa Beach, FL, **1999**; .

103. Cai, K. F.; Mueller, E.; Drasar, C.; Stiewe, C. The effect of titanium diboride addition on the thermoelectric properties of ß-FeSi2 semiconductors. *Solid State Commun.* **2004**, *131*, 325-329.

104. Biddulph, R. H. Method of hot pressing titanium diboride utilizing a growing sintered zone. **1970**.

105. Besmann, T. M.; Lowden, R. A. Titanium diboride ceramic fiber composites for Hall-Heroult cells. **1990**.

106. Kalantar-zadeh, K.; Fry, B. *Nanotechnology-Enabled Sensors;* Springer US: **2007**; .

107. Meyers, M. A.; Sarikaya, M.; Ritchie, R. O. *Nano and Microstructural Design of Advanced Materials;* Elsevier Science: **2003**; .

108. Zhu, D.; Kriven, W. M. *Advances in Ceramic Armor: A Collection of Papers Presented at the 29th International Conference on Advanced Ceramics and Composites, Jan 23-28, 2005, Cocoa Beach, FL, Ceramic Engineering and Science Proceedings, Vol 26;* Wiley: **2009**; .

109. Spilker, H.; Curtis, J. Sylramic SiC Fiber, COI Ceramics Inc., ATK Space Systems. **2006**.

110. King, D. S.; Fahrenholtz, W. G.; Hilmas, G. E. Silicon carbide–titanium diboride ceramic composites. *Journal of the European Ceramic Society* **2013**, *33*, 2943-2951.

111. Chen, D.; Zhang, X.; Ritchie, R. O. In *Mechanisms of High-Temperature Fatigue and Fracture in Silicon Carbide Ceramics;* Fatigue and Fracture Behavior of High Temperature Materials; John Wiley & Sons, Inc.: **2001**; pp 1-8.

112. Landwehr, S. E.; Yeckley, R. L. Titanium diboride-silicon carbide composites useful in electrolytic aluminum production cells and methods for producing the same. **2013**.

113. Tikekar, N. M.; The University, o. U. *Novel Double-layer Titanium Boride Coating on CP-titanium and Titanium-aluminum-vanadium Alloy: Kinetics of Boron Diffusion and Coating Morphologies;* University of Utah: **2007**; .

114. Qian, M.; Froes, F. H. *Titanium Powder Metallurgy: Science, Technology and Applications;* Elsevier Science: **2015**; .

115. Bhatt, R. T. Oxidation Effects on the Mechanical Properties of a SiC-Fiber-Reinforced Reaction-Bonded Si3N4 Matrix Composite. *J Am Ceram Soc* **1992**, *75*, 406-412.

116. Naito, K.; Tsuji, T.; Matsui, T.; Une, K. Purification of Inert Gas. *J Nucl Sci Technol* **1974**, *11*, 22-28.

117. National Research Council (US) Committee on,Magnetic Materials; National, R. C.; National Research Council (US) National Materials,Advisory Board *Magnetic Materials: Report;* National Academy Press: **1985**; .

118. White, R. M. Report on the Committee of Magnetic Materials. *National Materials Advisory Board* **1985**, *Publication NMAB-426*.

119. Kaneo Mohri; Tsuyoshi Uchiyama; Panina, L. V. Recent advances of micro magnetic sensors and sensing application. *Sensors and Actuators A: Physical* **1997**, *59*, 1-8.

120. Wake, L. V.; Brady, R. F. Formulating Infrared Coatings for Defense Applications. *DSTO Materials Research Laboratory* **1993**, *MRL Research Report MRL-RR-1-93*.

121. Wang, S. X.; Taratorin, A. M. In Magnetic Information Storage Technology, *Chapter 1 - Introduction;* Wang, S. X., Taratorin, A. M., Eds.; Magnetic Information Storage Technology; Academic Press: San Diego, **1999**; pp 1-30.

122. Department of Defense In *Ceramic Matrix Composites;* MIL-HDBK-17-5, Ed.; Department of Defense Handbook, Composite Materials Handbook; Department of Defense: **2002**; Vol. 5, pp 87-88.

123. Chung, D. D. L. *Composite Materials: Functional Materials for Modern Technologies;* Springer London: **2013**; .

124. Tompkins, H. G.; Augis, J. A. The oxidation of cobalt in air from room temperature to 467°C. *Oxidation Metals , 16*, 355-369.

125. Bertrand, N.; Desgranges, C.; Poquillon, D.; Lafont, M. C.; Monceau, D. Iron Oxidation at Low Temperature (260-500°C) in Air and the Effect of Water Vapor. *Oxidation Metals* **2009**, *73*, 139-162.

126. Graham, M.; Cohen, M. On the Mechanism of Low□Temperature Oxidation (23°–450° C) of Polycrystalline Nickel. *J. Electrochem. Soc.* **1972**, *119*, 879-882.

127. Fomenko, E. V.; Anshits, N. N.; Vasilieva, N. G.; Mikhaylova, O. A.; Rogovenko, E. S.; Zhizhaev, A. M.; Anshits, A. G. Characterization of Fly Ash Cenospheres Produced from the Combustion of Ekibastuz Coal. *Energy Fuels***2015**, *29*, 5390-5403.

128. Coatings, N. R. C. C. *High-temperature Oxidation-resistant Coatings: Coatings for Protection from Oxidation of Superalloys, Refractory Metals, and Graphite;* National Academy of Sciences: **1970**;

129. Anufrieva, T. A.; Derlyukova, L. E. Reactions of cobalt oxide with chlorine. *Russian Journal of Inorganic Chemistry , 52*, 1840-1843.

130. Kittel, Charles (2005). *Introduction to Solid State Physics* (8th ed.). New York: John Wiley & Sons. ISBN 978-0-471-41526-8.

131. Kumzerov, Y. A.; Kartenko, N. F.; Parfenaeva, L. S.; Smirnov, I. A.; Sysoeva, A. A.; Misiorek, H.; Jezowski, A. Determination of the Neel temperature from measurements of the thermal conductivity of the Co3O4 antiferromagnet nanostructured in porous glass channels. *Physics of the Solid State* **2012**, *54*, 1066-1069.